INSTITUTO DE PESQUISAS ENERGÉTICAS E NUCLEARES
Autarquia Associada à Universidade de São Paulo

Creation and spatial-temporal characterization of gas targets and plasmas for laser-electron acceleration

ARMANDO VALTER FELICIO ZUFFI

Tese apresentada como parte dos requisitos para obtenção do Grau de Doutor em Ciências na Área de Tecnologia Nuclear - Materiais

Orientador:
Prof. Dr. Ricardo Elgul Samad

São Paulo
2023

INSTITUTO DE PESQUISAS ENERGÉTICAS E NUCLEARES
Autarquia Associada à Universidade de São Paulo

Creation and spatial-temporal characterization of gas targets and plasmas for laser-electron acceleration

Versão Corrigida
Versão Original disponível no IPEN

ARMANDO VALTER FELICIO ZUFFI

Tese apresentada como parte dos requisitos para obtenção do Grau de Doutor em Ciências na Área de Tecnologia Nuclear - Materiais

Orientador:
Prof. Dr. Ricardo Elgul Samad

São Paulo
2023

Fonte de Financiamento: O Conselho Nacional de Desenvolvimento Científico e Tecnológico

Como citar:

FELICIO ZUFFI, A. V. ***Creation and spatial-temporal characterization of gas targets and plasmas for laser-electron acceleration***. 2023. 147 f. Tese (Doutorado em Tecnologia Nuclear), Instituto de Pesquisas Energéticas e Nucleares, IPEN-CNEN, São Paulo. Disponível em: ‹http://repositorio.ipen.br/› (data de consulta no formato: dd/mm/aaaa)

Ficha catalográfica elaborada pelo Sistema de geração automática da Biblioteca IPEN, com os dados fornecidos pelo(a) autor(a).

Felicio Zuffi, Armando Valter
Creation and spatial-temporal characterization of gas targets and plasmas for laser-electron acceleration / Armando Valter Felicio Zuffi; orientador Ricardo Elgul Samad. -- São Paulo, 2023.
147 f.

Tese (Doutorado) - Programa de Pós-Graduação em Tecnologia Nuclear (Materiais) -- Instituto de Pesquisas Energéticas e Nucleares, São Paulo, 2023.

1. ultrafast laser micromachining. 2. time resolved interferometry. 3. density retrieval algorithms. 4. laser-plasma interactions. 5. laser wakefield acceleration. I. Elgul Samad, Ricardo , orient. II. Título.

INSTITUTO DE PESQUISAS ENERGÉTICAS E NUCLEARES
Autarquia Associada à Universidade de São Paulo

Creation and spatial-temporal characterization of gas targets and plasmas for laser-electron acceleration

Original Version

ARMANDO VALTER FELICIO ZUFFI

A thesis submitted to obtain the degree of Doctor in Science in Nuclear Technology – Materials

Advisor:
Prof. Dr. Ricardo Elgul Samad

São Paulo
2023

In memory of
my paternal grandmother
and my maternal grandfather.

ACKNOWLEDGEMENTS

This thesis would not have been possible without the support of many people. I get to express my heartfelt thanks to everyone who was involved directly or indirectly in this present work.

First of all, I would like to express my gratitude to my advisor *Prof. Dr. Ricardo Elgul Samad* for his encouragement and care during my research and writing of this thesis. His enthusiasm and friendly attitude keep things going easily even in the most difficult situations.

I owe special thanks to *Prof. Dr. Nilson Vieira Dias Júnior* for all the insightful discussions that we have had. He assumed a leadership role in efforts to implement the first laser-plasma accelerator infrastructure in Brazil, always motivating everyone involved in this aim.

I also owe special thanks to *Prof. Dr. Edison Puig Maldonado* for his valuable advice, mainly when I started my PhD. He always suggested good references in the literature, which contributed to guiding this work.

I also thank *Prof. Dr. Sudeep Banerjee* for his collaboration with our research group, being one of the main motivators to join us in the laser wakefield acceleration field. His two visits to our lab gave me great learning and encouraged me to apply for a scholar internship in his former lab, Extreme Light Laboratory in the US.

I am very grateful to *MSc. Fabio Bittencourt Dutra Tabacow, Dr. José Antonio Sevidanes da Matta*, and *Dr. Jhonatha Ribeiro Santos* for their generous support and contributions during the development of this work.

At Lasers and Applications Center (CLA), I would like to thank *Prof. Dr. Wagner de Rossi* for his help in the fabrication of the nozzles, *Prof. Dr. Marcus Paulo Raele* for his advice during the development of the time-resolved Mach–Zehnder-like interferometer. In addition, thanks to *Paulinho* and *Marcão* for their contribution to the fabrication of several components used in the experimental setup in this work.

At Extreme Light Laboratory (ELL), I would like to thank *Prof. Dr. Donald Umstadter* for giving me the opportunity to work in his lab, being my co-advisor during my scholar internship at ELL. In addition, thanks to the ELL staff: *Daniel*, *Lake*, *Junzhi*, *Shao Xian*, *Shao Qin*, *Benjamin*, *Lisa*, *Ping*, *Kyle*, *Rakesh*, *Mukhtar*, and *Prof. Dr. M. Ashiq Fareed* for welcoming me and for guiding me during my two stays in Lincoln.

Bellow but not least, I would like to express my sincere gratitude to everyone who supported me emotionally during my PhD, keeping me positive during this period and during the pandemic lockdown.

Foremost, I want to express my gratitude and love to my partner, *Fernanda* for her partnership, giving all the support I needed and encouraging me to do my best. I have had such lovely moments spending time with her.

I extend my gratitude to my parents, *Wagner* and *Susi* for always supporting me in all my decisions, and providing me through moral their unconditional love. I am also grateful to my siblings, *Wagner (Junior)* and *Amanda*, as well as Amanda's partner, *Fabricio*, who have supported me along the way.

Furthermore, my other family members and friends deserve special thanks for also supporting me along the way, making these years more enjoyable. Therefore, thank you: my aunt *Neusa*, *Joaquim*, *Henrique*, *Júlio*, *Jorge*, *Luan*, *Leonardo* (*Mestre*), *Gabriel*, *Vinicius (Panda)*, *Renata*, *Pollyanna* (friends from my hometown); *Flaubert*, *Bruno*, *Talita*, *Álvaro (Mega)*, *Sandro*, *Israel*, *Rafael*, *Marcus*, *Renan*, *Milan*, *Flávio*, *Vinicius (Ney)*, *Arthur (Phelps)*, *Carol*, *Geisiane*, *Jhonas* (*Brothers*), *Mateus* (*Novinho*), *Rodriguinho*, *Rafael (Hot Wheels)*, *Raul*, *Wagner*, *Felipe (Febem)*, *Pollyanna*, *Danyellen*, *Denis*, *Gerson*, *Érico*, *Prof. Cleber*, *Prof. Lino* (friends from São Paulo or other cities); *Saulo*, *Noé*, *António*, *Giovanni*, *Camila Ramos*, *Tânia*, *Carol*, *Camila Salvego*, *Gilberto*, *Jonatan*, *Vitoria*, *Bruna*, *Reinaldo* (friends from IPEN); *Felipe*, *Adauto*, *Maria*, *Sunil*, *Sai*, *Josh*, *Roy*, *Denny* (friends from Lincoln).

Lastly, financial support and proper infrastructure were crucial to the development of this thesis. Therefore, I acknowledge *Conselho Nacional de Desenvolvimento Científico e Tecnológico (CNPq)* for my PhD scholarship (#142246/2018-2), *Coordenação de Aperfeiçoamento de Pessoal de Nível Superior (CAPES)* for my scholarship during the internship at ELL (#88887.576447/2020-00), *US Department of Energy (DoE)* for the funding granted during LaserNetUS Cycle3 project implementation, and *Fundação de Amparo à Pesquisa do Estado de São Paulo (FAPESP)* for financial support in our laboratory. I also would like to thank *Instituto de Pesquisas Energéticas e Nucleares (IPEN)* for the opportunity to perform my PhD work in a suitable infrastructure.

Those who are governed by reason, desire nothing for themselves which they do not also desire for the rest of humankind.

Baruch Spinoza

CONTENTS

LIST OF FIGURES

LIST OF TABLES

LIST OF CONSTANTS, SYMBOLS, AND ABBREVIATIONS

Constants

c	speed of light (vacuum) 299 792 458 m/s	$\mathcal{R}$	specific gas constant 8.31446261815324 J/K mol
e	elementary charge 1.6021766×10^{-19} C	r_e	classical electron radius 2.8179403×10^{-15} m
h	Planck constant 6.62607015×10^{-34} m²kg/s	ε_0	vacuum permittivity 8.8541878×10^{-12} F/m
k_B	Boltzmann constant 1.3806485×10^{-23} J/K	μ_0	vacuum permeability 1.2566371×10^{-6} N/A²
m_e	electron rest mass 9.1093836×10^{-31} kg		

Symbols

a	normalized vector potential	E_{wb}	wave-breaking electric field for relativistic cold plasma
a_0	normalized vector potential amplitude	$E_{wb,0}$	wave-breaking electric field for non-relativistic cold plasma
A	vector potential	$E_{wb,th}$	wave-breaking electric field for relativistic warm plasma
A_0	vector potential magnitude	$\mathcal{E}_{ion}$	atom ionization energy
b	confocal parameter	$\mathcal{E}_k$	electron kinetic energy
B	magnetic field	$\mathcal{E}_L$	laser pulse energy
c_P	specific heat for constant pressure	f	focal lengthF_p ponderomotive force
c_V	specific heat for constant volume	$\mathcal{F}_{th}$	ablation threshold fluence
D_{GVD}	dispersion parameter	h	gas jet height
E	electric field	I_0	intensity amplitude
E_0	electric field amplitude	I_{bg}	background intensity in the interferogram
E_{acc}	acceleration electric field	I_{BSI}	threshold laser intensity for BSI
E_{max}	maximum electric field		
E_s	spatial term of electric field		

I_{fr}	intensity of the interference fringes in the interferogram
I_L	laser intensity
I_{ref}	interference fringes intensity reference
I_{tar}	interference fringes intensity with the target
j	total current
j_f	free current in the plasma
k_0	central wave number
k_p	plasma wave number
k_{th}	wave number related to thermal effects
l	$1/e^2$ diameter of the plasma
L	propagation distance
L_{deph}	dephasing length
L_{depl}	depletion length
m_i	ion mass
$\dot{m}$	mass flow rate
M^2	laser quality factor
n_c	critical density
n_e	electron density or plasma density
$n_{e,0}$	initial electron density
n_g	neutral gas molecular density or gas density
$n_{g,0}$	gas molecular density in the backing chamber
n_i	ionic densities in state i
N_p	number of plasma periods behind the laser pulse
p	electron momentum
p_z	electron longitudinal momentum
p_x	electron transverse momentum
P	material polarization
$\mathcal{P}_{g,0}$	gas pressure in the backing chamber
$\mathcal{P}_L$	laser peak power
$\mathcal{P}_{RSF}$	critical laser power for relativistic self-focusing
Q	charge or bunch charge
Q_T	total charge
r	radial coordinate
R	gas jet radius
t	time
T_e	electron temperature
$T_{g,0}$	gas temperature in the backing chamber
U	Coulomb potential
U_p	ponderomotive potential
$U_{p,max}$	maximum ponderomotive potential
$\mathcal{U}_i$	ionic partition function for the state i
v	propagation velocity
v_1	electron velocity in a uniform electric field
v_2	electron velocity in a non-uniform electric field
v_{df}	electron drift velocity
v_e	electron velocity
v_{etch}	etching velocity
v_g	group velocity
v_{th}	electron thermal velocity
v_ϕ	phase velocity
$v_\perp$	electron orthogonal velocity

V	scalar potential
V_L	laser field potential
w	laser spot size
w_0	laser beamwaist
w_{min}	minimum laser beamwaist
W_{max}	maximum electron energy gain
x	x-axis or x-coordinate
y	y-axis or y-coordinate
x_1	electron displacement in a uniform electric field
z	z-axis or z-coordinate
Z	atom ionization state
z_R	Rayleigh length
A_e	nozzle exit area
α	molecular polarizability
A_t	nozzle throat area
β	interference fringe wavelength
γ_e	Lorentz factor
γ_g	Lorentz factor associated with the plasma wave velocity
γ_K	Keldysh parameter
δ	displacement of the interferogram fringes peaks
$\Delta\mathcal{E}_{ij}$	energy difference between the transition levels i and j
$\Delta\mathcal{E}_k$	electron kinetic energy width
Δt	interval of the interferometer probe pulses
$\Delta\varphi_r$	radial phase shift
$\Delta\phi$	integrated phase shift
$\Delta\lambda_L$	laser bandwidth
$\Delta\lambda_{pr}$	probe bandwidth
$\varepsilon_{x,rms}$	transverse normalized rms emittance in the x-axis
$\varepsilon_{y,rms}$	transverse normalized rms emittance in the y-axis
η	refractive index
η_p	plasma refractive index
$\eta_{p,0}$	linear contribution of the plasma refractive index
$\eta_{p,2}$	nonlinear contribution of the plasma refractive index
θ	wavefront tilted angle
θ_g	gas jet divergence angle
Θ	half-angle of the focused Gaussian laser beam
κ	ratio of the specific heats
λ_0	central wavelength
λ_{CM}	spectral center of mass
λ_L	laser wavelength
λ_p	plasma wavelength
$\lambda_{p,nl}$	nonlinear plasma wavelength
λ_{pr}	probe wavelength
μ	magnetic permeability
M	Mach number
ξ	coordinate in the frame co-propagating
ρ	charge density
ρ_f	charge distribution density
σ_{abel}	uncertainty of the accuracy of the inverse Abel transform
σ_{n_e}	uncertainty of the gas density
σ_{n_g}	uncertainty of the plasma density

$\sigma_{\Delta\phi}$	uncertainty of the integrated phase shift
$\sigma_{\lambda_{\mathrm{pr}}}$	uncertainty of the probe bandwidth
τ	time in the co-moving reference frame
τ_1	pulse duration (FWHM) before medium propagation
τ_2	pulse duration (FWHM) after medium propagation
τ_L	laser pulse duration (FWHM)
ϕ	phase shift
ϕ_0	initial phase shift
ϕ_{car}	carrier phase
ϕ_{dis}	unwanted distributions phase
ϕ_{SPM}	phase shift related to the self-phase modulation
ϕ_{sam}	phase related to the sample
Φ	electrostatic wake
$\emptyset$	diameter
$\emptyset_e$	nozzle exit diameter
$\emptyset_t$	nozzle throat diameter
$\chi^{(n)}$	n$^{\mathrm{th}}$-order electric susceptibility
ω	frequency
ω_0	central frequency
ω_L	laser frequency
ω_p	plasma frequency
$\omega_{p,th}$	plasma frequency related to thermal effects
ω_{rp}	relativistic plasma frequency

Abbreviations

ADK	Ammosov–Delone–Krainov ionization model
ATI	above threshold ionization
BBO	beta barium borate crystal
BSI	barrier suppression ionization
CCD	charge-coupled device
CEP	carrier-envelope phase
CPA	chirped pulse amplification
CW	continuous wave
DC	direct current
DIAG	interferometer diagnostic arm
ELL	Extreme Light Laboratory
FBPIC	Fourier-Bessel particle-in-cell
FFT	fast Fourier transform
FWHM	full width at half maximum
FWTM	Full width at tenth maximum
GPU	graphics processing unit
GUI	graphical user interface
GVD	group velocity dispersion
HAZ	heat affected zone
IFFT	inverse fast Fourier transform
IPEN	*Instituto de Pesquisas Energéticas e Nucleares* -

	Nuclear and Energy Research Institute
LCLS	linac coherent light source
LHC	Large Hadron Collider
LTE	local thermal equilibrium
LWFA	laser wakefield acceleration
MIV	measured in vacuum
MOSFET	metal–oxide semiconductor field-effect transistor
MPI	multi-photon ionization
MZI	Mach–Zehnder interferometer
OAP	off-axis parabolic mirror
OPCPA	optical parametric chirped-pulse amplification
PhD	philosophy doctor
PIC	particle-in-cell
QME	quasi-monoenergetic
QSA	quasi-static approximation
REF	interferometer reference arm
RF	radio-frequency
ROI	region of interest
RSF	relativistic self-focusing
RHIC	Relativistic Heavy Ion Collider
SEM	scanning electron micrography
SF	self-focusing
SM	envelop pulse self-modulation
SM-LWFA	self-modulated laser wakefield acceleration
SPM	self-phase modulation
TI	tunnel ionization
TTL	Transistor-Transistor Logic
UNL	University of Nebraska-Lincoln
UNL	University of Nebraska-Lincoln
VDC	volts of direct current
VHEE	very high energy electron

ABSTRACT

ZUFFI, A. V. F. Creation and spatial-temporal characterization of gas targets and plasmas for laser-electron acceleration. 2023. 147 p. Thesis (PhD in Sciences) – Nuclear and Energy Research Institute – IPEN-CNEN, São Paulo.

The acceleration of electrons by lasers is a technique that has been gaining importance all over the world in recent years due to its potential to decrease the size and complexity of accelerators, favoring the diffusion of this technology to conventional laboratories, with the inevitable emergence of new science and applications. The High Intensity Ultrashort Laser Pulses Laboratory at IPEN has been working to implement the first laser-electron acceleration infrastructure in Brazil and Latin America. For this purpose, we are currently focusing efforts on different challenges, ranging from the creation and characterization of micrometric gaseous targets and laser-induced plasmas for particle acceleration, to the upgrade of a laser system to achieve the needed peak powers. This PhD thesis explores a significant portion of these challenges, starting with the fabrication of micrometric de Laval nozzles by ultrafast laser micromachining in alumina, to generate laser targets in the form of supersonic gas jets in vacuum. Nozzles were manufactured in a home-built trepanning setup, and their geometry and surface quality dependence on the laser and machining parameters were studied, resulting in fabrication protocols that create de Laval nozzles capable of generating supersonic jets used as targets for laser-plasma interactions. To diagnose the micro-jets and the plasmas, a time-resolved Mach–Zehnder-like interferometer was developed, built, and coupled to a pump-probe setup to study the plasma dynamics with femtosecond resolution. In this setup, density profiles of gas jets and laser-induced plasmas were measured with a spatial resolution of a few micrometers. In addition, a detailed study of the laser-induced plasma evolution in air was conducted from tens of femtoseconds to hundreds of picoseconds, in which plasma formation, impact ionization, and electron recombination were investigated, using algorithms and softwares developed by our group. This diagnostic setup proved to be reliable to characterize the density gradients of micrometric laser-induced plasmas, becoming a permanent setup for further laser-electron acceleration developments at IPEN.

Keywords: ultrafast laser micromachining, time-resolved interferometry, density retrieval algorithms, laser-plasma interactions, laser wakefield acceleration

RESUMO

ZUFFI, A. V. F. Criação e caracterização espaço-temporal de alvos gasosos e plasmas para aceleração de elétrons por laser. 2023. 147 p. Tese (Doutorado em Ciências) – Instituto de Pesquisas Energéticas e Nucleares – IPEN-CNEN, São Paulo.

A aceleração de elétrons por lasers é uma técnica que vem ganhando importância em todo mundo nos últimos anos devido ao seu potencial de reduzir o tamanho e a complexidade de aceleradores, favorecendo a difusão desta tecnologia para laboratórios convencionais, com o inevitável surgimento de nova ciência e aplicações. O Laboratório de Lasers de Pulsos Ultracurtos de Alta Intensidade do IPEN vem trabalhando para implantar a primeira infraestrutura de aceleração de elétrons por laser no Brasil e na América Latina. Para este propósito, atualmente estamos concentrando esforços em diferentes desafios que vão desde a criação e caracterização de alvos gasosos micrométricos e plasmas induzidos por laser para a aceleração de partículas, até a melhoria de um sistema de laser para atingir as potências de pico necessárias. Esta tese de doutorado explora uma parte significativa desses desafios, começando com a fabricação de bocais de de Laval micrométricos por microusinagem de alumina por laser de pulsos ultracurtos, para gerar alvos para o laser na forma de jatos de gás supersônicos em vácuo. Um sistema de trepanação a laser foi construído no laboratório para a fabricação de bocais, e a dependência de sua geometria e qualidade da superfície com o laser e os parâmetros de usinagem foram estudados, resultando em protocolos de fabricação que criam bocais de de Laval capazes de gerar jatos supersônicos usados como alvos para interações laser-plasma. Para diagnosticar os microjatos e os plasmas, um interferômetro resolvido no tempo do tipo Mach-Zehnder foi desenvolvido, construído e acoplado a um arranjo bombeio-prova para estudar a dinâmica do plasma com resolução de femtossegundos. Nesta configuração, perfis de densidade de jatos de gás e de plasmas induzidos por laser foram medidos com uma resolução espacial de alguns micrômetros. Adicionalmente, um estudo detalhado da evolução do plasma induzido por laser no ar foi realizado de dezenas de femtossegundos a centenas de picossegundos, no qual a formação de plasma, ionização por impacto e recombinação de elétrons foram investigados utilizando algoritmos e softwares desenvolvidos pelo nosso grupo. Este sistema de diagnóstico provou ser confiável para caracterizar os gradientes de densidade de plasmas

micrométricos induzidos por laser, tornando-se um arranjo permanente para futuros desenvolvimentos de aceleração de elétrons por laser no IPEN.

Palavras-chave: microusinagem por laser de pulsos ultracurtos, interferometria resolvida no tempo, algoritmos de recuperação de densidade, interações laser-plasma, aceleração por campo de rastro

1 INTRODUCTION

Particle accelerators are among the largest machines built by humans, being the main tools for elementary particle research since their creation in 1932[1, 2]. These conventional particle accelerators use radio-frequency (RF) electromagnetic fields to propel charged particles at speeds close to that of light and to confine them in well-defined beams[3, 4]. The control of the quality of these beams (particle kinetic energy, bunch duration, and spatial properties such as divergence) is fundamental to their applications, which, for big accelerators, may include high-energy physics in colliders like the LHC[5] and the RHIC[6], and synchrotron light generation like in the Sirius[7], for investigations in condensed matter physics. For small accelerators, the applications can be particle beam diagnostics, medical therapies, and the production of radioisotopes for nuclear medicine [8, 9, 10], among others. However, due to the maximum electric fields on the order of 100 MV/m limited by the breakdown of the accelerator materials, those conventional accelerators can reach kilometers in length or in circumference, as exemplified by the LCLS in Figure 1.1a, being machines of high maintenance, complexity, and costs. Thus, there has always been a search for new acceleration technologies, and recently, particle acceleration driven by lasers has been growing rapidly in the scientific community[11, 12].

Figure 1.1 – (a) Aerial view of the 3.2 km LCLS in Stanford, capable of accelerating electrons up to 50 GeV. (b) Plasma produced by a high-intensity laser pulse incident on a gas jet. The length of the accelerating structure in this plasma is 4 mm and supports over 100 GV/m fields.

Source: Adapted from PATHAK, N. C.[13].

Plasma-based particle acceleration was originally introduced in 1979 by Tajima and Dawson[14], when they proposed that laser-induced plasmas could sustain

acceleration fields over 100 GV/m, three orders of magnitude higher than in RF accelerators. This increase provided a way to reduce the size of accelerators from the km to the laboratory scale, as shown in Figure 1.1b, representing a revolution for the use of such beams in many applications[15]. For decades, this kind of acceleration has been pursued by different approaches[16, 17, 18], and in 2004 an important breakthrough occurred when three distinct groups accelerated electrons to energies above 100 MeV in quasi-monoenergetic (QME) beams, with charges greater than 100 pC, and low beam divergence[19, 20, 21] by laser wakefield acceleration (LWFA). In this technique, high-intensity laser pulses ($>10^{17}$ W/cm^2, typically) are focused on a gaseous target in vacuum, creating a plasma region with a wave pattern of charge density, the so-called wakefield[19, 22]. This region is established, initially, by the gas laser-induced ionization followed by the action of the ponderomotive force originated by the spatial gradient of the laser intensity[23, 24], which moves the charges away from the laser intensity peak. As a result of this force, the electrons are moved transversely away from the pulse propagation axis, and are then attracted to the axis by the positive charges that remained there. These dynamics can establish, temporarily, a periodic net charge distribution along the pulse propagation axis[22]. This charge arrangement moves with the laser pulse close to the speed of light and works as a plasma accelerator channel (wakefield channel), capable of accelerating electrons.

To accelerate the electrons, they must be injected (or self-injected)[25, 26, 27] into the wakefield channel, and when this occurs at the appropriate time, they are trapped in regions with a high charge gradient and gain energy from the wakefield. These electrons are accelerated in bunches carried by the plasma waves and can reach kinetic energies over a few GeV[28, 29, 30] in tens of centimeters, grouped into bunches with tens of femtoseconds duration, with a total bunch charge between fC and nC[31] and a few percent energy dispersion, with divergence under 1 mrad, and current peaks of each bunch exceeding hundreds of amperes[32, 33, 34].

The breakthroughs in 2004 boosted new joint efforts in the high-intensity laser and accelerator communities (ICFA-International Committee for Future Accelerators)[35], and within these developments, in 2016 the North American Department of Energy published a report[36] pointing the direction of using lasers to accelerate particles to high energies in compact systems. Thus, several laser systems of this type have been developed and currently generate bunches of electrons and/or of ions (subsequently accelerated). The interaction of these particles with matter allows the development of tunable, compact

sources of high-energy ionizing radiation[37], which are already being used in new imaging techniques[38]. Other research applications of laser particle accelerators are the production of isotopes for medicine[39, 40], protontherapy, hadron therapy[10, 41], and fast ignition in fusion targets[42, 43].

Many of the LWFA approaches for accelerating electrons up to GeV use the blowout regime[44, 45, 46], in which the laser pulse length is close to the plasma wavelength, in a resonance condition. However, this approach requires laser pulses with peak powers in the range from 10 TW to 1 PW (duration of tens of femtoseconds and energies from a few hundred mJ to tens of J), and low-density plasmas (with electron densities n_e <10^{18} cm^{-3}). Those laser systems usually have several amplifiers (CPA or OPCPA) that, to avoid detrimental effects from high thermal charge, operate at low repetition rates (few Hz or lower), which is inadequate for most practical applications. On the other hand, Ti:Sapphire systems able to generate a few TW pulses at ~kHz repetition rates are widely available in many laboratories[47], and they have been presented as an alternative to acceleration by LWFA in the blowout regime using laser pulses of a few cycles (~fs), and high-density plasma waves (n_e >10^{19} cm^{-3}). Although this approach presents electrons bunches with energies limited to tens of MeV[48], since the high-density plasma reduces the acceleration length to lesser than a few hundred micrometers due to the electron dephasing length[33], many applications that require scanning, matter probing, radioisotope production, among others[49, 50], become viable on this energy range and repetition rates. However, the post-compression of laser pulses to a few fs and its propagation, present additional challenges that involve the energy losses in the spectral broadening[51], high group velocity dispersion (GVP)[52, 53], and carrier-envelope phase (CEP) stabilization[52, 54].

Another alternative to generate MeV electron bunches with peak powers of a few TW at kHz operation rates is the self-modulated LWFA (SM-LWFA) regime[55, 56, 57], with the additional advantage of not requiring laser pulse compression to a few fs in contrast to the LWFA using few cycle pulses. The SM-LWFA can generate bunches with a total charge in the nC range (two orders of magnitude higher than LWFA)[58, 59], which makes these bunches attractive for applications where a high dose of radiation is required[59, 60, 61]. Promising results showed recently the possibility of accelerating electron bunches to MeV using a laser with peak powers as low as 40 GW and pulse energy of ~1.3 mJ[62]. This regime differs from the conventional LWFA by using high densities (n_e >10^{19} cm^{-3}) and long pulses (tens to hundreds of fs), outside the resonance condition.

When a pulse propagates through the plasma, its leading edge undergoes stimulated Raman backscattering[63], while the pulse peak undergoes a stimulated Raman forward scattering[64] and self-modulation[65, 66], longitudinally modulating itself and creating a train of laser micropulses at the plasma period, as illustrated in Figure 1.2. This establishes a new resonance condition, in which the plasma waves, and, consequently, the accelerating fields, are enhanced. Additionally, the SM-LWFA regime also helps the electron injection by the self-focusing mechanism, leading to an increase in laser intensity that favoring ionization.

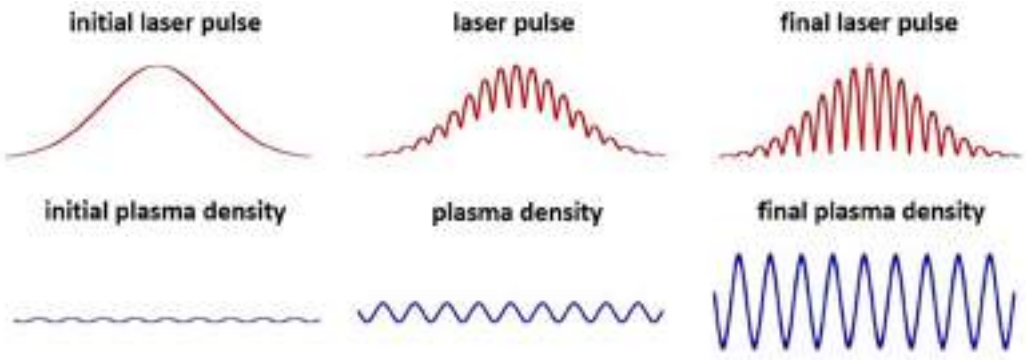

Figure 1.2 – Evolution of the laser pulse and plasma density in SM-LWFA. The laser pulse is modulated, creating a train of laser micropulses resonant with the high-density plasma wave.
Source: Adapted from MALKA, V.[67].

Besides Ti:Sapphire laser systems, there has been significant progress in fiber[68] and diode-pumped solid-state laser systems[69] that generate sub-TW pulses, with hundreds of femtoseconds, and up to tens of kHz repetition rates. Those systems together with the SM-LWFA regime may be the key to making laser-plasma acceleration more practical and enabling numerous applications. However, at this moment the SM-LWFA has not been able to produce electron bunches as collimated and as monoenergetic as the ones from LWFA, but relativistic energies have already been reported[62].

To generate optimal electron bunches (energies up to tens of MeV, quasi-monoenergetic and low divergence) in the SM-LWFA regime, or even in the LWFA with few-cycle pulses, submillimetric and flat-top gaseous targets with well-defined high-densities regions are usually required[50, 70, 71, 72]. A simple way to create this kind of target is by using supersonic gas jets generated by de Laval nozzles[50], expanding in a vacuum. These jets are pulsed synchronously with the laser shots[73], and their well-defined edges ensure that the ionization and wakefield formation only occurs in the region of high gas density, preventing losses of laser pulse energy[74].

The typical de Laval (or converging-diverging) nozzle geometry is illustrated in Figure 1.3. In this kind of nozzle, a high-pressure gas in the backing chamber originates a flow, which is subsonic in the nozzle converging section, compressing the gas passing the throat, through the diverging section where the gas axial velocity progressively increases due to a free expansion and after the exit exhausts into the vacuum environment as a supersonic jet[70, 71]. Although de Laval nozzles are employed in many different applications, they have been poorly investigated at the micrometric scale, being mainly explored in the context of micro-thrusters for small-scale spacecraft[75, 76] and, only recently, in laser-plasma experiments in the LWFA scope[77, 78].

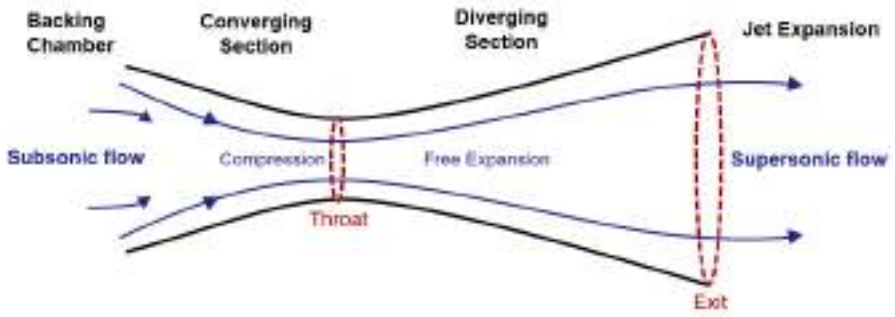

Figure 1.3 – Schematic geometry of a de Laval nozzle. Blue lines represent the conversion of the gas flow from the subsonic to the supersonic regime through the nozzle converging-diverging sections.

Source: By the author.

Once the supersonic gas jet is created by the de Laval nozzle, its diagnosis, as well as the characterization of the laser-induced plasma in it, is essential for a better understanding of the laser-plasma interaction dynamics in LWFA. Currently, one of the main problems limiting the laser-plasma accelerators to reach higher energies and currents are the instability and reproducibility of the electron bunches quality[79], which may come from the dynamics of either the wakefield formation or the electron injection mechanism. Several groups have been studying this problem[80, 81, 82], and they are working on improvements in the control of the experimental parameters (increased laser operating stability, target reproducibility, etc.). For high repetition rate regimes, such as SM-LWFA, these requirements are even more strict than for low repetition rates or single-shot systems, since the demand for practical applications is greater, and maintaining good operation stability for intervals smaller than milliseconds should be a challenging task[72]. In this scope, the urging for reliable diagnostic tools, especially those which respond in the timeframe of the pulse duration has been drawing increasing attention[83, 84, 85], as well

as statistical methods to assist the experiments[86, 87, 88]. A large part of the effort to have a laser-plasma accelerator installation running is devoted to diagnostic systems, which are critical for a reproducible daily operation[89]. Approximately 10% of the budget of any accelerator is devoted to diagnostics, which are essential to control the experimental parameters. Several non-disturbing optical methods can be used to characterize the gas jet, the laser-induced plasma, and the electron bunches[56]. These techniques include interferometry[90], Schlieren imaging[91], spectroscopy[92], and fluorescence measurements[56], among others.

Interferometry is a very accurate technique capable of quantifying very small optical path differences, and therefore, suitable for measuring density variations in gaseous targets, and laser-induced plasmas[89, 93, 94]. Additionally, in the SM-LWFA regime, usually, the laser pulses are tightly focused (close to the diffraction limit) in a thin gaseous target, limiting the plasma region, and, consequently, the wakefield to tens of μm, demanding a highly accurate technique. From an interferometry measurement (interferogram), the phase-shift accumulated by a laser beam propagating through a gas jet or plasma can be extracted, and consequently, their density distribution can be determined. While a continuously flowing gas target can be diagnosed by CW interferometry, to analyze a laser-induced plasma, time-resolved techniques are required[89] due to the short plasma formation time and excited ions fast decay[95], which would fade the signal in CW techniques due to the extremely small duty-cycle. In this scope, the interferometry made with femtosecond temporal resolution is a powerful diagnostic tool for LWFA (and SM-LWFA), since this technique can characterize the gaseous target (continuous or pulsed flow)[96], and also laser-induced plasmas[93, 97, 98] during the wakefield formation and electron acceleration process[99].

In light of this encouraging scenario, many groups worldwide have been pursuing advances in the LWFA field and other plasma acceleration schemes, from institutions across North America, Europe, and Asia[100]. In Latin America, our research group has worked to pioneer the implementation of a laser-plasma accelerator at the Nuclear and Energy Research Institute (IPEN-CNEN)[101, 102, 103]. The main goal of this proposal is to produce electron bunches with energy up to tens of MeV by the SM-LWFA regime. Those electrons would be able to generate γ-radiation by bremsstrahlung[104, 105], with enough energy to induce the photonuclear reaction ^{100}Mo (γ, n) ^{99}Mo, as a future application[106] for the production of radiopharmaceuticals. This alternative for radioisotope generation could have a big impact on Brazil, which spends, annually, an estimated US$ 15 million

for importing the ^{99}Mo[107] isotope. In addition to this benefit, this project opens up a range of other applications within medicine, such as protontherapy[108] and very high energy electron (VHEE) therapy[109, 110].

Particle-in-cell (PIC) simulations have been showing us the possibility to generate tens of MeV electron bunches by SM-LWFA, using TW or sub-TW laser pulses and gaseous targets with submillimetric dimensions[58, 111, 112, 113, 114]. In addition to computational PIC simulation support, we are currently focusing efforts on several developments required for a LWFA installation, such as a source of high-peak-power laser pulses[115], proper gaseous and plasma target creation[116, 117], and development and implementation of diagnostic tools to assist and monitor the experiments[118, 119].

During this PhD, I worked on the development of techniques to manufacture micrometric de Laval nozzles by ultrafast laser micromachining[116, 120]. We established a methodology to manufacture high-quality de Laval nozzles by ultrashort laser pulses trepanning on alumina substrates (Al_2O_3), a dielectric ceramic. This strategy has been producing nozzles that originate supersonic jets with interaction lengths of 100 µm and longer. Those nozzles also were explored in some laser-electron acceleration experiments conducted at the Extreme Light Laboratory (ELL) at the University of Nebraska-Lincoln (UNL), with which our research group has a cooperation agreement[121]. Furthermore, I worked on the development of a new time-resolved Mach–Zehnder-like interferometer coupled to a pump-probe setup capable of diagnosing transient phenomena in gaseous targets and laser-induced plasmas on the femtosecond scale[118, 122, 123]. The development and implementation of this interferometer have provided useful information about the submillimetric gas jets created by the laser micromachined nozzles, and the plasma region created into the gaseous target. Lastly, the implementation of this interferometer in a vacuum environment, where the SM-LWFA studies will be conducted, was also a PhD goal. This step aims to establish a permanent diagnostic setup in the future laser electron acceleration installation at IPEN.

1.1 Thesis outline

This thesis has been structured in the following way:

Chapter 1: provides an introduction to laser-based plasma accelerators, exploring the scientific context, competitiveness over conventional accelerators, and the evolution of

this technology. Moreover, the motivation for starting a laser electron acceleration installation in Brazil (IPEN) and its challenges are explored, thereby connecting the PhD aims to this goal.

Chapter 2: reviews the theoretical background on laser-plasma interactions. Topics include basic ionization mechanisms, interaction dynamics between a laser pulse and a single electron, the collective plasma response to a laser pulse, and a description of electron acceleration mechanisms. Although no LWFA (or SM-LWFA) outcomes are presented in this thesis, the topics discussed in Chapter 2 are the theoretical basis for the laser-plasma acceleration field, therefore they were chosen to compose this chapter.

Chapter 3: motivates the discussion about PIC simulations since it is a lead-off to establishing the aims of this PhD, and therefore the further experimental activities discussed in the next chapters. Section 3.1 presents a brief introduction to PIC algorithms in general, as well as the specific code of azimuthal Fourier decomposition used by our research group. Section 3.2 summarizes simulation results, demonstrating the viability to generate MeV electron bunches by SM-LWFA from laser parameters that could be achieved at IPEN.

Chapter 4: addresses to discuss the two high intensity laser systems available in our laboratory. Section 4.1 describes the T-cube laser system, which is undergoing an upgrade to implement a second amplifier stage to reach a laser peak power of about 1 TW enough to conduct SM-LWFA experiments. Section 4.2 describes the Femtopower laser system, which was the system used in the experimental activities discussed in this thesis.

Chapter 5: dedicated to micrometric Laval nozzles, which are required to generate the gaseous target according to simulation results. Section 5.1 describes a simple model for de Laval nozzles capable to generate supersonic gas flows. Section 5.2 and the ultrafast laser micromachining technique used for producing our homemade micrometric de Laval nozzle. Section 5.3 discusses the characterization of manufactured de Laval nozzles by optical profilometry and scanning electron microscopy.

Chapter 6: dedicated to interferometric diagnostic of the typical targets in LWFA experiments. Section 6.1 discusses in detail the steps involved in analyzing the interferograms to obtain the gas jet or laser-induced plasma density profiles and presents a homemade software developed by our group to retrieve those targets. Section 6.2 addresses the development of a CW interferometer setup in atmosphere capable to diagnose the supersonic gas jets generated by our laser micromachined nozzles. Section

6.3 shows the development of a time-resolved Mach-Zehnder-like interferometer coupled in a pump-probe setup to diagnose the evolution of gas jets as well as laser-induced plasmas. The setup assembled firstly in atmosphere leads to an interesting investigation of the laser-induced plasma formed in air, also discussed in this section. Section 6.4 discusses the implementation of the time-resolved Mach-Zehnder-like interferometer inside a vacuum chamber to diagnose the desired targets for future laser-electron acceleration studies at IPEN, which is the first step to establishing a diagnostic tool for further LWFA target characterizations.

Chapter 7: concludes and summarizes the work done in this thesis and provides an outlook into how these outcomes can be utilized to benefit the future experiments aimed at by our research group at IPEN.

2 THEORY OF LASER-PLASMA INTERACTIONS

In this chapter, the fundamental theory involving laser-plasma interactions in the LWFA scope is reviewed. The principal references for this chapter include the textbook by Paul Gibbon[124], and the PhD thesis by Ajay Kawshik Arunachalam[125], by Alexander Sävert[126], Jinpu Lin[127], and Ralph Jung[128].

2.1 Ionization mechanisms

Ultrashort pulses from Ti:Sapphire (Ti:Al_2O_3) lasers have a photon energy around 1.55 eV, which is smaller than the amount required for the direct first ionization of usual LWFA gaseous targets, such as helium (24.6 eV) and nitrogen (14.5 eV). Nevertheless, at sufficiently high intensities, nonlinear effects become relevant and the interaction with multiple photons or the strong laser field can promote the ionization. With a photon density comparable to the atomic or molecular density of the gaseous target, the probability that multiple photons are absorbed by a single atom or molecule becomes non-negligible. For that, short-lived virtual electronic states can be created with a lifetime in the order of the pulse duration, given by Heisenberg's uncertainty[126] for transitions in the visible and near UV range. This process is called multi-photon ionization (MPI), as illustrated in Figure 2.1a, and can be described by perturbative nonlinear optics[129], since the laser field is weak compared to atomic potential, and does not distort it. The electron also can absorb more photons than required for ionization and leave the atom with net kinetic energy, a process known as above threshold ionization (ATI).

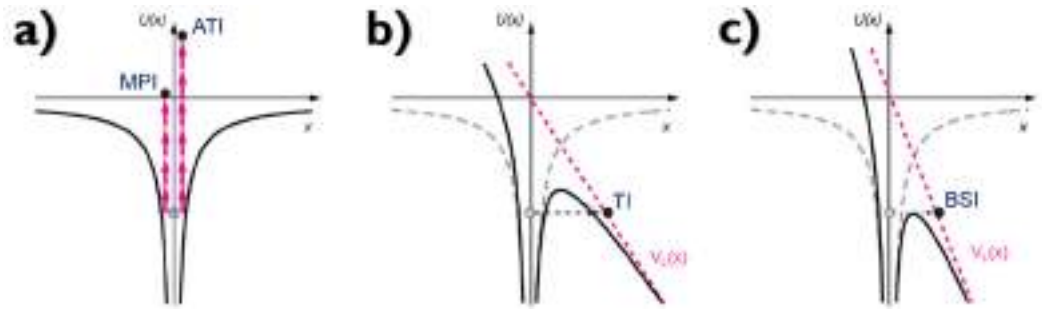

Figure 2.1 – Nonlinear ionization mechanisms: (a) multi-photon ionization (MPI) and above threshold ionization (ATI), (b) tunnel ionization (TI), (c) barrier suppression ionization (BSI). The Coulomb potential is represented by $U(x)$ (black solid line) and the laser field potential represented by $V_L(x)$ (dashed pink line).
Source: Adapted from SÄVERT, A.[126].

At higher laser intensities, its electric field exceeds the binding potential of the electron, and the process can no longer be treated by the perturbative theory. At these intensities, the dominant ionization mechanism is tunnel ionization (TI), in which the electron tunnels through the potential barrier resulting from the Coulomb potential modified by the laser field, as shown in Figure 2.1b. The threshold between MPI and TI can be estimated by the Keldysh parameter[130], γ_K, given by:

$$\gamma_K = \frac{Time\ to\ tunnel\ out}{Period\ of\ laser\ field} \approx \sqrt{\frac{\mathcal{E}_{ion}}{2\,U_{p,max}}}, \tag{2.1}$$

where $\mathcal{E}_{ion}$ is the atom ionization energy for a specific state, and $U_{p,max}$ is the maximum ponderomotive potential, which is the electron quiver energy averaged over one oscillation period, and can be expressed, in eV, by:

$$U_{p,max}[\mathrm{eV}] = 9.33 \times 10^{-14} (I_L[\mathrm{W/cm^2}]\ \lambda_L^2[\mu\mathrm{m}]), \tag{2.2}$$

where I_L and λ_L are the laser intensity and its wavelength, respectively. MPI dominates for $\gamma_K > 1$, which corresponds to high ionization energies and/or low laser intensities, whereas TI dominates for $\gamma_K < 1$, which corresponds to low ionization energies and/or high laser intensities. Meanwhile, the ratio expressed by (2.1) is only valid as long as the laser field is less than the Coulomb potential. For even higher intensities, the Coulomb potential is extremely distorted by the laser field, becoming smaller than the binding energy and the electron can be freed spontaneously, a process called barrier suppression ionization (BSI), which is a limit case of TI, as illustrated in Figure 2.1c. The threshold laser intensity for BSI, I_{BSI}, can be estimated by setting the Coulomb potential equal to the ionization potential[126, 131]:

$$I_{BSI}[\mathrm{w/cm^2}] \approx 4.0 \times 10^9 \frac{\mathcal{E}_{ion}^4[\mathrm{eV}]}{Z^2}, \tag{2.3}$$

where Z is the atom ionization state. Although the BSI model presents satisfactory agreement with experimental results[131, 132, 133], mainly for simple gaseous species, more accurate ionization rates can be estimated using more complex approaches from the finite laser pulse duration and 3D shape of the atom or molecule[126].

Once the laser field ionizes electrons from atoms, the freed electrons can collide with ions and ionize them to release more electrons. This process is called impact ionization (or collisional ionization), causing an avalanche effect[127, 134]. This thermal process occurs for times longer than the ultrashort pulse duration. However, for a high

target density or long pulse duration, there will be enough collisional events such that impact ionization can dominate over the laser ionization mechanisms[123].

2.2 Laser pulse and single electron interaction

To understand the interactions between a high-intensity laser pulse and a plasma, it is worth examining what happens to a single electron in the presence of the laser field. Although the laser pulses can be approximated by Gaussian profiles both in the spatial and temporal domains, once they are focused to reach high intensities, in the focal region they can be considered to be a plane wave for many applications[126]. Therefore, assuming 1D plane waves for the laser near the focus, a single electron driven by the Lorentz force[124] obeys:

$$\frac{d\boldsymbol{p}}{dt} = \frac{d}{dt}(\gamma_e m_e \boldsymbol{v_e}) = -e(\boldsymbol{E} + \boldsymbol{v_e} \times \boldsymbol{B}), \tag{2.4}$$

where $\boldsymbol{E}$ and $\boldsymbol{B}$ are the laser electric and magnetic fields, respectively, e is the elementary charge, $\boldsymbol{p}$ is the electron momentum, m_e is the electron mass, $\boldsymbol{v_e}$ is electron velocity, and the Lorentz factor is $\gamma_e = 1/\sqrt{1 - \boldsymbol{v_e}^2/c^2}$, with c as the speed of light in vacuum. Moreover, the fields $\boldsymbol{E}$ and $\boldsymbol{B}$ can be expressed by the vector potential $\boldsymbol{A}$ and the scalar potential V as:

$$\boldsymbol{E} = -\frac{\partial \boldsymbol{A}}{\partial t} - \boldsymbol{\nabla} V, \tag{2.5}$$

$$\boldsymbol{B} = \boldsymbol{\nabla} \times \mathbf{A}. \tag{2.6}$$

Using the vector potential $\boldsymbol{A}$ and considering the absence of field sources ($V = 0$), equation (2.4) can be rewritten to the form:

$$\frac{d\boldsymbol{p}}{dt} = \frac{\partial \boldsymbol{p}}{\partial t} + (\boldsymbol{v_e} \cdot \boldsymbol{\nabla})\boldsymbol{p} = -e\left(\boldsymbol{v_e} \times \boldsymbol{\nabla} \times \boldsymbol{A} - \frac{\partial \boldsymbol{A}}{\partial t}\right) = -e\left[\boldsymbol{\nabla}(\boldsymbol{v_e} \cdot \boldsymbol{A}) - \frac{d\boldsymbol{A}}{dt}\right], \tag{2.7}$$

which is explored in the next session for two cases: non-relativistic and relativistic electrons.

2.2.1 Non-relativistic case

When the electron velocity is much smaller than the speed of light ($v_e \ll c$), the contribution of the magnetic force is negligible compared to the electric one, expressly

$|\boldsymbol{v_e} \times \boldsymbol{B}| \ll |\boldsymbol{E}|$. This is the classical limit ($\gamma_e \approx 1$) in which the equation (2.7) can be reduced to:

$$\frac{d\boldsymbol{p}}{dt} = e\frac{d\boldsymbol{A}}{dt} \Rightarrow m_e\frac{d\boldsymbol{v_e}}{dt} = e\frac{d\boldsymbol{A}}{dt}. \tag{2.8}$$

Assuming an electron at rest at the origin, at $t = 0$, its velocity and displacement can be obtained by making the ansatz $\boldsymbol{A} = A_0 \sin(k_0 z - \omega_0 t)\hat{x}$, a linear polarized plane wave propagating along the z-axis with central wave number k_0 and central frequency ω_0. Integrating equation (2.8) in time, results in:

$$\boldsymbol{v_e} = \frac{eA_0}{m_e}\sin(k_0 z - \omega_0 t)\,\hat{x}, \tag{2.9}$$

$$\boldsymbol{x} = \frac{eA_0}{\omega_0 m_e}[1 - \cos(k_0 z - \omega_0 t)]\,\hat{x}. \tag{2.10}$$

Both equations (2.9) and (2.10) demonstrate the motion of the electron (or quiver motion) as a harmonic oscillation along the x direction centered around $eA_0/\omega_0 m_e$, while its position in the z direction remains unchanged. The electron displacement has a phase of π relative to the applied $\boldsymbol{E}$ field (laser), as shown in Figure 2.2, whereas its velocity is $\pi/2$ out of phase .

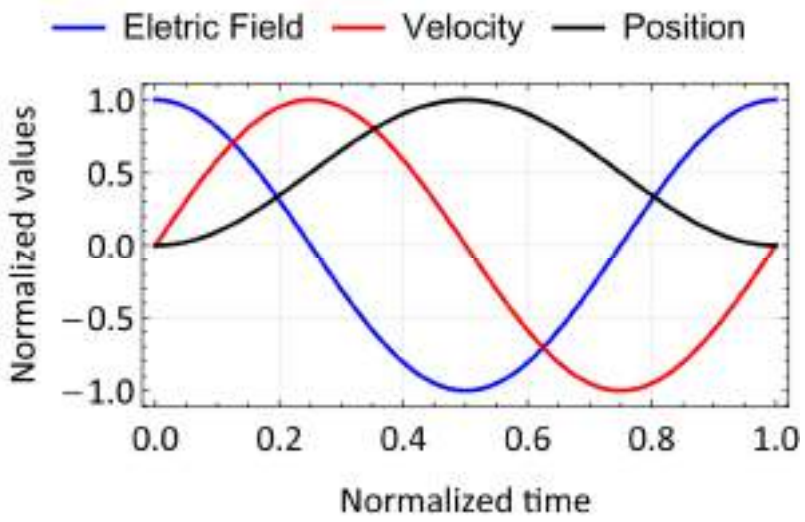

Figure 2.2 – Normalized relation of phase between Electric Field (E), electron velocity (v_e) and electron transverse position (x) in a non-relativistic laser field.
Source: By the author.

2.2.2 *Relativistic case*

At laser intensities close to 10^{18} W/cm^2, at which the electrons velocities approach the speed of light ($v_e \approx c$), the magnetic force becomes comparable to the electric force,

and the electron dynamics become nonlinear. At this moment, the normalized vector potential $\boldsymbol{a}$ is commonly introduced, and its laser strength parameter (dimensionless amplitude) a_0 can be related to the laser intensity I_L in the following way:

$$I_L = \frac{1}{2}\varepsilon_0 c E_0^2 = 2\pi^2 \varepsilon_0 c^5 \left(\frac{m_e a_0}{e\lambda_L}\right)^2 \implies a_0 = \sqrt{\frac{I_L[W/cm^2](\lambda_L[\mu m])^2}{1.37 \times 10^{18}}}, \qquad (2.11)$$

where ε_0 is the vacuum permittivity and E_0 is the laser electric field amplitude. For $a_0 = 1$, the electron kinetic energy gained from the laser field is equal to electron rest energy and, therefore, for $a_0 \geq 1$ the electron quiver motion becomes relativistic. Applying equation (2.11) is a common way to determine whether the laser field is relativistic. For a typical Ti:Sapphire laser system (λ_L = 0.8 μm), $a_0 = 1$ is reached at a laser intensity I_L = 2.1×10^{18} W/cm^2.

In the relativistic approach, the $\boldsymbol{B}$ field and the Lorentz factor ($\gamma_e < 1$) cannot be disregarded, and the equation for the motion of the electron, (2.7), is kept in its complete form:

$$\frac{d\boldsymbol{p}}{dt} = \frac{d}{dt}(\gamma_e m_e \boldsymbol{v_e}) = -e\left[\boldsymbol{\nabla}(\boldsymbol{v_e} \cdot \boldsymbol{A}) - \frac{d\boldsymbol{A}}{dt}\right]. \qquad (2.12)$$

For a plane wave, the condition $\frac{\partial}{\partial x}(v_\perp A_0) = \frac{\partial}{\partial y}(v_\perp A_0) = 0$ is valid for transverse components. Thus, it follows that $\frac{d}{dt}p_x = e\frac{dA}{dt}$, which can be integrated with the first invariant C_1:

$$p_x - eA = C_1, \qquad (2.13)$$

where p_x is the electron transverse momentum. Furthermore, using the equation (2.12) to analyze the electron longitudinal momentum, p_z, conducts to the second invariant C_2, given by:

$$\frac{dp_z}{dt} = m_e c\frac{d\gamma_e}{dt} \Rightarrow \gamma_e - \frac{p_z}{m_e c} = C_2, \qquad (2.14)$$

where $v_e \approx c$ was assumed due to the relativistic regime. For an electron initially at rest at the origin, the constants C_1 and C_2 are equal to 0 and 1, respectively. Thus, from the equations (2.13) and (2.14) the following can be reduced:

$$p_x = eA, \qquad (2.15)$$

$$\mathcal{E}_k = m_e c^2(\gamma_e - 1) = p_z c = \frac{1}{2}\frac{p_x^2}{m_e c}. \qquad (2.16)$$

Equations (2.15) and (2.16) are the two conservation laws for the electron motion: the transverse momentum p_x and the kinetic energy $\mathcal{E}_k$[126]. Using the new ansatz $\boldsymbol{a} = a_0 \sin(k_0 z - \omega_0 t)\hat{x}$, with the normalized potential vector amplitude defined as $a_0 = eA_0/m_e c^2$, and in the co-moving reference frame ($\tau = t - z/c$), the equations (2.15) and (2.16) can be integrated to obtain the electron trajectory[124]:

$$z(\tau) = \frac{c}{4} a_0^2 \left[\tau - \frac{1}{2\omega_0}\sin(2\omega_0\tau)\right], \tag{2.17}$$

$$x(\tau) = \frac{c}{\omega_0} a_0 [1 - \cos(\omega_0\tau)], \tag{2.18}$$

$$z(\tau) = 0, \tag{2.19}$$

where the central frequency ω_0 can be written as the laser frequency ($\omega_0 = \omega_L$), form used by many authors[125, 126]. The transverse motion $x(\tau)$ oscillates like the classical non-relativistic motion, described in equation (2.10). The longitudinal motion $z(\tau)$ is a combination of an oscillation with double the laser frequency, with a longitudinal translation with a drift velocity $v_{df} = ca_0^2/(a_0^2 + 4)$. The Figure 2.3 illustrates the electron trajectory (quiver motion) for different values of a_0 in the laboratory frame and in the co-moving frame ($v_{df} = 0$), the latter containing the typically "figure-8" motion. It is noteworthy that if a circularly polarized laser is used instead of a linear one, the electron would describe a circular trajectory with a radius $a_0/\sqrt{2}\gamma_e$ in the co-moving frame and a helical orbit in the laboratory frame[128].

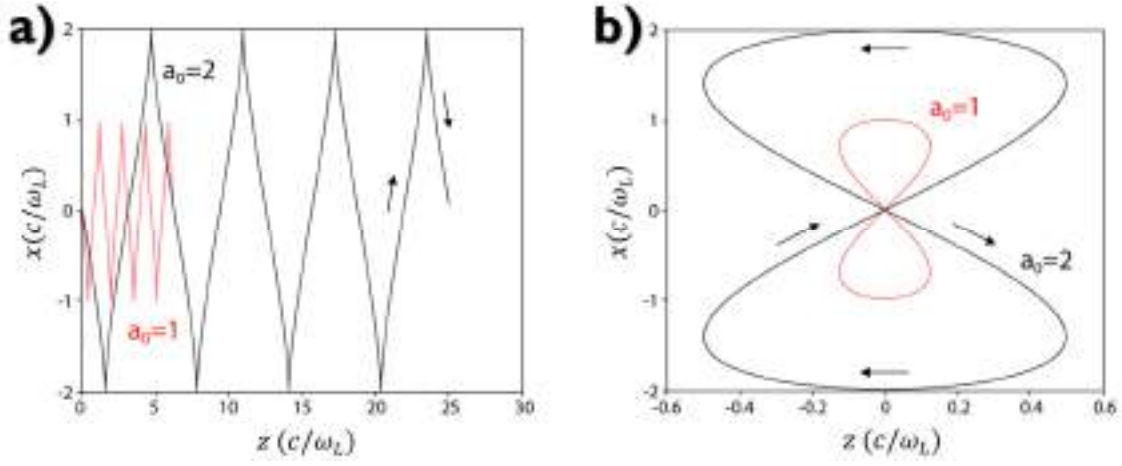

Figure 2.3 – Illustrative trajectory of an electron in a relativistic laser field interaction (for $a_0 = 1$ and $a_0 = 2$) observed (a) in the laboratory frame and (b) in a co-moving frame, presenting a figure-8 motion.
Source: Adapted from SÄVERT, A.[126].

Indeed, a high-intensity laser pulse (in the form of a plane wave at focus) will accelerate a single electron both transversally and longitudinally. However, when the electron surpasses the laser period, it is decelerated and returns to the initial position (behind the pulse), although it is displaced towards the laser propagation axis. While the symmetry of acceleration and deceleration are undisturbed, the electron gains no net energy from the laser field in vacuum according to the Lawson-Woodward theorem[135, 136] that is valid since the following assumptions are fulfilled[137]:

1. The interaction region is in vacuum and is infinite (there are any boundaries),
2. The electron is highly relativistic along the acceleration path,
3. There are no static electric or magnetic fields,
4. Ponderomotive effects are neglected.

Once one or more of the above assumptions are violated, the electron can, in principle, gain net kinetic energy from the laser field. As will be outlined in the following sections, a very effective way to obtain a net electron acceleration with relativistic laser fields is via the generation of strongly driven Langmuir waves (plasma waves), which violates all of the assumptions made in the Lawson-Woodward theorem[138].

2.3 Ponderomotive force

As mentioned in the previous section, an electron in a plane wave (constant amplitude) gains no net kinetic energy. However, real high-intensity laser pulses present intensity gradients in the radial and longitudinal directions, with the peak in the laser axis. This intensity gradient leads radially to a net force on the electron. Here, this net force is calculated from the equation of electron motion (2.4) in its non-relativistic form (γ_e=1) and by including an inhomogeneous electric field $\boldsymbol{E} = \boldsymbol{E_s}(\boldsymbol{x})\cos(\omega_0 t)$, with a spatial term that can be described by a first-order Taylor expansion:

$$\boldsymbol{E_s}(\boldsymbol{y}) = \underbrace{\boldsymbol{E_s}(\boldsymbol{x})|_{\boldsymbol{x_0}}}_{Constant\ term} + \underbrace{(\Delta\boldsymbol{x}\cdot\boldsymbol{\nabla})\boldsymbol{E_s}(\boldsymbol{x})|_{\boldsymbol{x_0}}}_{1^{st}-order} + \cdots \tag{2.20}$$

where $\Delta\boldsymbol{x} = \boldsymbol{x_1} - \boldsymbol{x_0}$. Taking into account only the 1st order term (homogenous contribution), for an electron initially at the axis, ($\boldsymbol{x_0} = 0$), its velocity $\boldsymbol{v_1}$ and displacement $\boldsymbol{x_1}$ can be obtained by integrating equation (2.4), resulting in the equations that describe the motion of an electron acted upon by an uniform electric field:

$$\boldsymbol{v_1} = \frac{e}{m_e\omega_0}\boldsymbol{E_s}(\boldsymbol{x_0})\sin(\omega_0 t), \tag{2.21}$$

$$\Delta \boldsymbol{x} = \boldsymbol{x_1} = \frac{e}{m_e \omega_0^2} \boldsymbol{E_s}(\boldsymbol{x_0}) \cos(\omega_0 t). \tag{2.22}$$

The inhomogeneous contribution of the electron motion can be obtained by applying equation (2.4) assuming only the motion resulting in the non-uniform electric field and $\boldsymbol{v_1} \times \boldsymbol{B}$, given as:

$$m_e \frac{d\boldsymbol{v_2}}{dt} = -e\left[(\boldsymbol{x_1} \cdot \boldsymbol{\nabla})\boldsymbol{E}(\boldsymbol{x_1}, t)|_{\boldsymbol{x_0}} + \boldsymbol{v_1} \times \boldsymbol{B}(\boldsymbol{x_1}, t)\right], \tag{2.23}$$

where $\boldsymbol{v_2}$ is the electron velocity in a non-uniform electric field. It is noteworthy that in this approach the magnetic field force contribution ($\boldsymbol{v_1} \times \boldsymbol{B}$) is relevant, being described in terms of a non-uniform electric field expansion making $\boldsymbol{v} \times \boldsymbol{B} = \boldsymbol{E} \times (\boldsymbol{\nabla} \times \boldsymbol{E})$. Time averaging over the fast oscillations of the laser field and using the equations (2.21) and (2.22), modifies equation (2.23) to[125]:

$$\boldsymbol{F_p} = m_e \langle \frac{d\boldsymbol{v_2}}{dt} \rangle = -\frac{e^2}{4 m_e \omega_0^2} \boldsymbol{\nabla}(\boldsymbol{E_s^2}) \tag{2.24}$$

where the $\boldsymbol{F_p}$ is termed ponderomotive force, which is a resulting force arising from a non-uniform laser field. This net force is proportional to the laser intensity (through $\boldsymbol{E_s^2}$), and it is opposed to the intensity gradient, therefore, it drives electrons toward regions of low intensity. It is worth mentioning that the force applied on an electron is much greater than that applied on an ion due to the mass dependence in equation (2.24). Therefore, is usual to neglect the ion dynamics, assuming that it remains static in this approach.

The ponderomotive force also can be written in terms of the ponderomotive potential as $\boldsymbol{F_p} = -\boldsymbol{\nabla} U_p$, where U_p can be equated to the time-averaged kinetic energy gained by the electron from the laser field, shown as:

$$U_p = -\frac{e^2}{4 m_e \omega_0^2} \boldsymbol{E_s^2} \equiv \frac{1}{2} m_e \langle \boldsymbol{v_e} \rangle^2, \tag{2.25}$$

where the $\langle \boldsymbol{v_e} \rangle$ spatial distribution follows the pulse envelope.

For a relativistic electron, a similar expression for the ponderomotive force can be obtained using the relativistic equation of motion of the electron[139]:

$$\boldsymbol{F_p} = -\boldsymbol{\nabla} U_p = -\frac{e^2}{4 \langle \gamma_e \rangle m_e \omega_0^2} \boldsymbol{\nabla}(\boldsymbol{E_s^2}), \tag{2.26}$$

where $\langle \gamma_e \rangle$ is the time-averaged Lorentz factor. Analogously to the non-relativistic case, the ponderomotive force expels the electron from regions of high intensity toward lower intensities. For ultrashort laser pulses, it means that, besides the radial motion, the electrons are also accelerated forwards and backwards in the laser propagation direction,

along with an increase in the quivering amplitude due to the net energy gained by the electron from the laser field, as illustrated in Figure 2.4. The differences in the dynamics between the non-relativistic and the relativistic cases arise from the relativistic electron mass increase (decreasing $\boldsymbol{F_p}$) and the magnetic field contribution, which is considered throughout this approach.

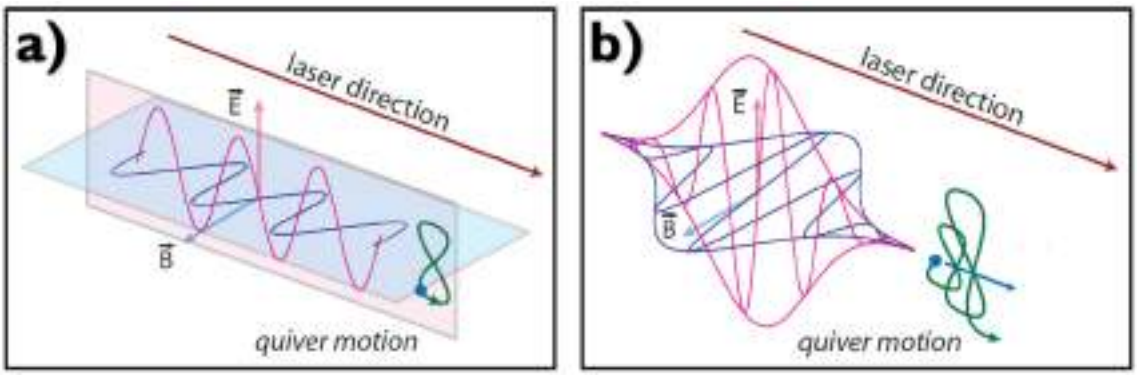

Figure 2.4 – Illustrative trajectories of an electron in a relativistic laser field observed at a co-moving frame under (a) a homogenous laser field (constant intensity), in which the electron quiver motion is a figure-8, and (b) an inhomogeneous laser field (ultrashort laser pulse), where the quiver motion increases its amplitude in each laser period, as well displaces the electron along the laser propagation.
Source: Adapted from PLATEAU, G.[140].

For the laser-plasma interaction, the time-averaged Lorentz factor $\langle\gamma_e\rangle$ can be expressed in terms of time-averaged normalized potential vector:

$$\langle\gamma_e\rangle = \sqrt{1 + \langle\boldsymbol{a}\rangle^2}\,, \tag{2.27}$$

where $\langle a\rangle^2 = a_0^2/2$ for linearly polarized laser pulses, and $\langle a\rangle^2 = a_0^2$ for circularly polarized pulses[127]. The more frequently used expression of the ponderomotive force is also described in terms of the normalized potential vector using $a_0 = eE/m_e\omega_0^2 c$ in equation (2.26), which results, for linearly polarized pulses, in the following:

$$\boldsymbol{F_p} = -\boldsymbol{\nabla} U_p = -\frac{m_e c^2}{2\langle\gamma_e\rangle}\boldsymbol{\nabla}\langle\boldsymbol{a^2}\rangle. \tag{2.28}$$

In this case, the ponderomotive potential can be described as:

$$U_{p,max} = m_e c^2(\langle\gamma_e\rangle - 1) \Rightarrow\ U_{p,max}[\text{MeV}] = 0.511\left(\sqrt{1 + \langle a\rangle^2} - 1\right), \tag{2.29}$$

which corresponds to the average kinetic energy gained by the electron from the laser field. As an example, a linearly polarized high-intensity laser at $\lambda_L = 0.8$ µm with $I_L = 4.0{\times}10^{19}$ W/cm^2 produces $a_0 = 4.8$, corresponding to an electron energy gain of $U_p = 0.8$ MeV, in contrast to the Lawson-Woodward theorem[135, 136]. As will be outlined

in the following sections, when the collective plasma oscillations contribute to the acceleration process, the energy gained by the electrons is notably greater than the ponderomotive potential for equivalent laser parameters.

2.4 Plasma properties

To better understand the propagation of a laser pulse in a plasma is essential to initially comprehend the electrons collective behavior. A plasma can be defined as a collection of ionized matter that admits quasi-neutrality, meaning that the electrons and ions charge densities are approximately equal over a large scale[13]. Under normal plasma conditions, the ions can be assumed to be motionless compared with the electrons in the presence of an external field. Due to the ion mass, m_i, being much greater than electron rest mass ($m_i/m_e > 10^3$), the electron moves considerably faster in external field response, making the ions stationary on the electron time scale. Therefore, the plasma collective behavior is communally described in terms of its electrons response.

For an externally applied perturbation in a plasma, such as a laser pulse, the electrons are displaced from the background of ions, and an electric field distribution is created in the plasma. This electric field acts to restore plasma neutrality by pulling the electrons back to their initial, equilibrium, positions. Nevertheless, due to their inertia, the electrons will oscillate around their equilibrium positions with a characteristic plasma frequency, ω_p, which from the cold and collisionless plasma assumption (electron temperature $T_e = 0$), can be described as:

$$\omega_p = \sqrt{\frac{n_e e^2}{\varepsilon_0 m_e}}, \tag{2.30}$$

where n_e is the electron density (or plasma density). In a relativistic laser field, the electron oscillation speed reach values close to the speed of light, being necessary to include the relativistic correction in equation (2.30). This is done using the time-averaged Lorentz factor, resulting in the relativistic plasma frequency $\omega_{rp}^2 = \omega_p^2/\langle\gamma_e\rangle$. It is noteworthy that since the thermal motion of the elections is considered, the dispersion relation for the collective electron oscillations can be described by the Bohm-Gross relation[141]:

$$\omega_{p,th}^2 = \omega_p^2 + 3v_{th}^2 k_{th}^2, \tag{2.31}$$

where the electron thermal velocity is $v_{th} = \sqrt{k_B T_e / m_e}$, with k_B being the Boltzmann constant, and k_{th} is the wave number related to the propagation of the electron density oscillations due to the thermal effects. However, thermal effects play a key role only for time scales higher than an ultrashort laser pulse duration (> ps). For that reason, during the ultrashort pulse laser-plasma interaction the plasma can be well described as a cold and collisionless plasma.

The inverse of ω_p is the electrons response time to a disturbing external field. For instance, if a laser field with a frequency ω_L impinges into a plasma, the electrons will move to restore plasma neutrality. However, if $\omega_L > \omega_p$ the electrons will not be able to shield the laser field since the period of the electromagnetic oscillation of the laser is shorter than the response time of the electrons. Such a plasma is called an underdense plasma once its electron density allows this laser field to propagate through it. Otherwise, if the plasma has a higher density such as $\omega_L < \omega_p$, the electrons respond fast enough and absorb the laser field. This second condition is known as an overdense plasma. Making $\omega_L = \omega_p$ defines the electron density at which the plasma becomes overdense, known as critical density n_c, which is given by:

$$n_c = \frac{\varepsilon_0 m_e \omega_L^2}{e^2} \Rightarrow n_c[cm^{-3}] = \frac{1.1\times10^{21}}{\lambda_L^2[\mu m]}. \tag{2.32}$$

Although the underdense and overdense plasma classifications are commonly employed, some authors define near-critical plasma with densities in the interval of $0.1 n_c < n_e < n_c$[125]. Moreover, it is worth noting that for the relativistic case, the critical density is increased to $n_c \langle \gamma_e \rangle$.

2.5 Laser propagation in underdense plasmas

The propagation of an electromagnetic wave in an underdense plasma can be described from the Maxwell equations in the matter, given by[142]:

$$\boldsymbol{\nabla} \cdot \boldsymbol{E} = -\frac{1}{\varepsilon_0} \boldsymbol{\nabla} \cdot \boldsymbol{P} + \rho_f, \tag{2.33}$$

$$\boldsymbol{\nabla} \times \boldsymbol{E} = -\frac{\partial \boldsymbol{B}}{\partial t}, \tag{2.34}$$

$$\boldsymbol{\nabla} \cdot \boldsymbol{B} = 0, \tag{2.35}$$

$$\boldsymbol{\nabla} \times \boldsymbol{B} = \mu \left(\varepsilon_0 \frac{\partial \boldsymbol{E}}{\partial t} + \frac{\partial \boldsymbol{P}}{\partial t} + \boldsymbol{j_f} \right), \tag{2.36}$$

where we define new variables: $\boldsymbol{P}$ is the plasma polarization, ρ_f is the charge density, μ is the magnetic permeability that in this context can be approximated to the vacuum permeability ($\mu \approx \mu_0$), and the total current is $\boldsymbol{j} = (\partial \boldsymbol{P}/\partial t) + \boldsymbol{j_f}$, with $\partial \boldsymbol{P}/\partial t$ being the bound currents, and $\boldsymbol{j_f}$ the free currents in the plasma. Considering the plasma as a dielectric medium, where only the transverse electron oscillations in the electric field $\boldsymbol{E}$ are allowed, results in $\rho_f = 0$ and $\boldsymbol{J_f} = 0$. From these assumptions, and combining the Maxwell equations, is possible to obtain a wave equation[125]:

$$\boldsymbol{\nabla^2 E} - \frac{1}{c^2}\frac{\partial^2 \boldsymbol{E}}{\partial t^2} = \frac{1}{\varepsilon_0}\left[\frac{1}{c^2}\frac{\partial^2 \boldsymbol{P}}{\partial t^2} - \boldsymbol{\nabla}(\boldsymbol{\nabla}\cdot\boldsymbol{P})\right], \tag{2.37}$$

where $c = 1/\sqrt{\varepsilon_0 \mu_0}$ and $\boldsymbol{\nabla}\cdot\boldsymbol{P}$ can be regarded as zero since only the transverse motion of the electrons is considered. Furthermore, assuming an instantaneous electrons response to the external electric field $\boldsymbol{E}$, the polarization $\boldsymbol{P}$ can be described in terms of $\boldsymbol{E}$ to account for the nonlinear response of plasma, which is given in the vectorial form as[143]:

$$\boldsymbol{P} = \sum_{\boldsymbol{n=1}}^{\infty} \varepsilon_0 \chi^{(n)} \boldsymbol{E^n} = \underbrace{\varepsilon_0 \chi^{(1)} \boldsymbol{E}}_{linear\ response} + \underbrace{\varepsilon_0 \chi^{(2)} \boldsymbol{E^2} + \varepsilon_0 \chi^{(3)} \boldsymbol{E^3} + \cdots}_{nonlinear\ response}, \tag{2.38}$$

where the constant $\chi^{(1)}$ is the first-order electric susceptibility, which depends on the microscopic properties of the medium (plasma). The higher-order electric susceptibilities ($\chi^{(2)}$, $\chi^{(3)}$,$\cdots$) describe the nonlinear response of plasma and depend also on the different powers of the external electric field $\boldsymbol{E}$.

2.5.1 Linear response

The linear response of a plasma, related to $\chi^{(1)}$, is independent of the external electric field $\boldsymbol{E}$, being the plasma polarization directly proportional to the electric field by $\boldsymbol{P} = \varepsilon_0 \chi^{(1)} \boldsymbol{E}$. For a purely transverse plasma response, the time derivative of the bound current results in $\partial^2 \boldsymbol{P}/\partial t^2 = \varepsilon_0 \chi^{(1)} \partial^2 \boldsymbol{E}/\partial t^2$, which can be substituted in equation (2.37) to obtain the following wave equation for an underdense plasma:

$$\boldsymbol{\nabla^2 E} = \frac{1+\chi^{(1)}}{c^2}\frac{\partial^2 \boldsymbol{E}}{\partial t^2} = \left(\frac{\eta}{c}\right)^2 \frac{\partial^2 \boldsymbol{E}}{\partial t^2}, \tag{2.39}$$

with the refractive index $\eta = \sqrt{1 + \chi^{(1)}}$ and, therefore, a propagation velocity $v = c/\eta$. The bound current $\partial \boldsymbol{P}/\partial t$ depends on the transverse electron oscillations and is related to the electrons velocity by:

$$\frac{\partial \boldsymbol{P}}{\partial t} = -e n_e \boldsymbol{v_e}. \tag{2.40}$$

Combining the time derivative of the equation (2.40) with the time derivative of the bound current produces the following relation:

$$\frac{\partial^2 \boldsymbol{P}}{\partial t^2} = -e n_e \frac{\partial \boldsymbol{v_e}}{\partial t} \equiv \varepsilon_0 \chi^{(1)} \frac{\partial^2 \boldsymbol{E}}{\partial t^2}. \tag{2.41}$$

In addition, considering the motion of a non-relativistic electron, described by $\partial \boldsymbol{v_e}/\partial t = -e\boldsymbol{E}/m_e$, under excitation by a plane wave $\boldsymbol{E} = \boldsymbol{E_o} exp[i(\omega_0 t - k_0 x)]$, the equation (2.41) yields an expression for the plasma electric susceptibility:

$$\chi^{(1)} = -\frac{e^2 n_e}{m_e \varepsilon_0 \omega_0^2} = -\frac{\omega_p^2}{\omega_0^2}, \tag{2.42}$$

expressed in terms of the plasma frequency. Thus, the plasma refractive index for an electromagnetic wave with a frequency ω_0, can be described as:

$$\eta_p = \sqrt{1 + \chi^{(1)}} = \sqrt{1 - \frac{\omega_p^2}{\omega_0^2}} = \sqrt{1 - \frac{n_e}{n_c}}. \tag{2.43}$$

For underdense plasmas, in which $n_e < n_c$, this refractive index is smaller than 1; on the other hand, for overdense plasmas ($n_e > n_c$), the refractive index becomes imaginary, indicating that the electromagnetic wave is absorbed cannot propagate into it.

The propagation velocity of the electromagnetic field occurs at the phase velocity v_ϕ, and can be described using the plasma refractive index and the equation (2.43):

$$v_\phi = \frac{\omega_0}{k_0} = \frac{c}{\eta_p} = \sqrt{\frac{c^2 \omega_0^2}{(\omega_0^2 - \omega_p^2)}}, \tag{2.44}$$

which shows that $v_\phi > c$ in an underdense plasma. Moreover, equation (2.44) provides the dispersion relation of an electromagnetic wave with a frequency ω_0 and wave number k_0 propagating in plasma, given by:

$$\omega_0^2 = \omega_p^2 + c^2 k_0^2, \tag{2.45}$$

which shows that the minimum frequency allowed for the propagation of an electromagnetic wave through a plasma is ω_p, as already mentioned in Section 2.4. A more realistic description of a laser pulse considers a Gaussian distribution of frequencies, which can be decomposed in several monochromatic waves, and also satisfies the wave equation (2.39). However, during the laser pulse propagation through a plasma, each frequency component experiences a different refractive index. Thus, each frequency

component travels with a different phase velocity that introduces changes in the temporal structure of the laser pulse, a phenomenon so-called dispersion. The velocity with which the pulse envelope moves in the medium can be studied by assuming an overlap of the two monochromatic waves of the same amplitude with slightly different frequencies ($\omega_0 \pm \Delta\omega$) and wave numbers ($k_0 \pm \Delta k$). From these assumptions, the resulting electric field can be described by[125]:

$$\boldsymbol{E} = \boldsymbol{E_0} e^{i[(\omega_0+\Delta\omega)t-(k_0+\Delta k)x]} + \boldsymbol{E_0} e^{i[(\omega_0-\Delta\omega)t-(k_0-\Delta k)x]}, \tag{2.46}$$

from which the real component of the resultant electric field is:

$$\boldsymbol{E} = 2\boldsymbol{E_0} \cos(\omega_0 t - k_0 x) \cos(\Delta\omega t - \Delta k x), \tag{2.47}$$

where the first cosine corresponds to a plane wave with a phase velocity $v_\phi = \omega_0/k_0$, whereas the second cosine is a modulation of $2\pi/\Delta k$ wavelength traveling at a velocity:

$$\frac{\Delta\omega}{\Delta k} \approx \frac{\partial\omega}{\partial k} = v_g. \tag{2.48}$$

It is noteworthy that this analysis can be extended to include more frequencies, providing a better representation of a real laser pulse. However, the conclusion will be basically the same. The v_g is termed the group velocity, and it refers to the velocity of the laser pulse envelope moving through the medium, which for propagation in an underdense plasma can be characterized by its refractive index η_p using the dispersion relation from equation (2.45):

$$v_g = \frac{\partial\omega}{\partial k} = \frac{k_0 c^2}{\sqrt{\omega_p^2 + c^2 k_0^2}} = c\frac{c}{\omega/k} = c\eta_p. \tag{2.49}$$

At relativistic intensities, the plasma frequency and the critical density need to be corrected due to the electron mass increase that yields, $\omega_{rp}^2 = \omega_p^2/\langle\gamma_e\rangle$ and $n_c\langle\gamma_e\rangle$, as shown in Section 2.4. Thus, the relativistic plasma refractive index is:

$$\eta_p = \sqrt{1 - \frac{\omega_p^2}{\langle\gamma_e\rangle\omega_0^2}} = \sqrt{1 - \frac{n_e}{\langle\gamma_e\rangle n_c}}. \tag{2.50}$$

2.5.2 Nonlinear response

The nonlinear response of a plasma to an external electric field $\boldsymbol{E}$ can be understood from the plasma refractive index in equation (2.50), since $\langle\gamma_e\rangle = \sqrt{1 + \langle\boldsymbol{a}\rangle^2}$ is dependent on the intensity of the electric field. Thus, this dependence originates

propagation effects during the laser pulse displacement through the underdense plasma, such as ionization-induced defocusing, relativistic and ponderomotive self-focusing, and self-phase modulation. These effects can be related to refractive index changes following the temporal and spatial profile of a laser pulse, as well as the local plasma density. In addition, the effects can be studied by introducing perturbations in the plasma density in the form $n_e' = n_e + \delta n_e$, and in the laser central frequency $\omega_0' = \omega_0 + \delta\omega_0$, where $\delta n_e \ll n_e$ and $\delta\omega_0 \ll \omega_0$. Using these perturbations terms in the linear approximation of the refractive index of the plasma, which is only valid for an underdense plasma with $n_e \ll n_{crit}$, the equation (2.50) can be rewritten as:

$$\eta_p \approx 1 - \frac{1}{2}\frac{1}{\sqrt{1+\langle \boldsymbol{a} \rangle^2}}\frac{n_e+\delta n_e}{(\omega_0+\delta\omega_0)^2}. \tag{2.51}$$

For a linearly polarized laser pulse with non-relativistic intensities ($a_0 < 1$), the inverse of the time-averaged Lorentz factor, $1/\langle\gamma_e\rangle = 1 - a_0^2/4$, can be used in equation (2.51) and expanded as[22, 126]:

$$\eta_p = 1 - \frac{1}{2}\frac{\omega_p^2}{\omega_0^2}\left(1 - \frac{a_0^2}{4} + \frac{\delta n_e}{n_e} - 2\frac{\delta\omega_0}{\omega_0}\right). \tag{2.52}$$

Likewise, for relativistic intensities ($a_0 > 1$), with $1/\langle\gamma_e\rangle = (\sqrt{2}/a_0)(1 - 1/a_0^2)$, equation (2.51) can be expanded to:

$$\eta_p = 1 - \frac{1}{\sqrt{2}}\frac{\omega_p^2}{\omega_0^2 a_0}\left(1 - \frac{1}{a_0^2} + \frac{\delta n_e}{n_e} - 2\frac{\delta\omega_0}{\omega_0}\right). \tag{2.53}$$

The refractive index dependence on δn_e, $\delta\omega_0$ and a_0 yields several different effects that impact the laser pulse during its propagation through an underdense plasma. For instance, the normalized density perturbation $\delta n_e/n_e$ is the term influenced by transverse electron modulations that can produce self-focusing effects (for $\delta n_e/n_e < 0$), or plasma defocusing effects (for $\delta n_e/n_e > 0$), and the normalized frequency perturbation $\delta\omega_0/\omega_0$ is responsible for self-phase modulation. In this Section, each of these effects is studied in detail using different mathematical approaches. In addition, although each effect could compete with others depending on their strengths, they are treated independently and any combination of the propagation effects is ignored due to the complex required analysis.

Ionization-induced defocusing (plasma defocusing)

Considering the propagation of a laser pulse in a gaseous target such as argon, for non-relativistic laser intensities exceeding the gas ionization threshold, the ionization

process results in a decrease in the refractive index since $\eta_p = (1 - n_e/n_c)^{1/2}$. However, the laser pulses usually present a radial Gaussian intensity distribution centered on the propagation axis that results in an electron density distribution related to the various ionization levels of the gas, as illustrated in Figure 2.5a. It corresponds to a resulting plasma refractive index and a laser phase velocity identical to propagation in a negative lens as shown in Figure 2.5b. This reduced phase velocity at the peak of the laser intensity leads to a defocusing effect. For a wavefront that is being focused, this causes first a decrease and then an increase in its radius of curvature. Thus, the laser pulse propagation continues to be dominated by the defocusing effect while its intensity exceeds the ionization threshold.

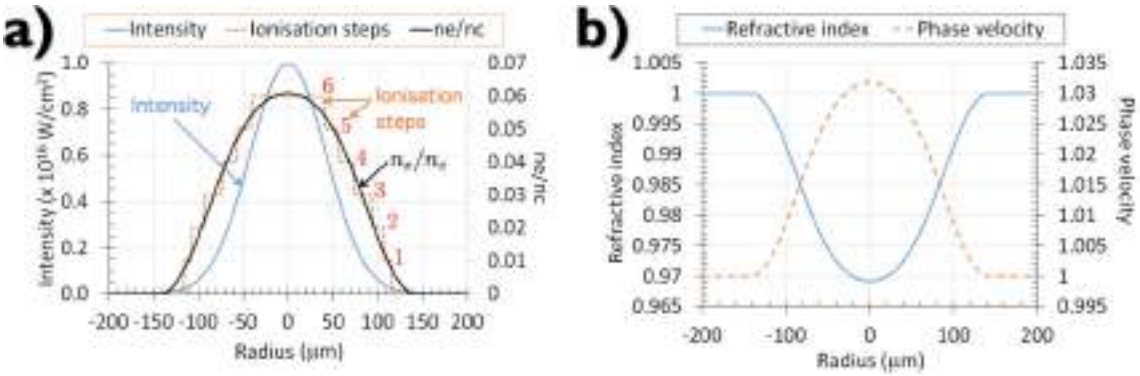

Figure 2.5 – Illustrative changes of plasma refractive index in the ionization-induced defocusing effect: (a) Laser intensity with a Gaussian radial distribution (blue line) with the corresponding ionization intensity levels for argon (orange line) and a smooth plasma density profile (black line), where the transition of the argon ionization states is assumed to be smooth between the two related successive ionization states. (b) Radial distribution of the plasma refractive index (blue line) and laser phase velocity (orange line).
Source: Adapted from ARUNACHALAM, A. K.[125].

The formulation of the ionization-induced defocusing effect can be studied by assuming a Gaussian beam focused to a beamwaist w_0, corresponding to a Rayleigh length $z_R = \pi w_0^2/\lambda_L$ and focused half-angle $\Theta = \lambda_L/\pi w_0$, as illustrated in Figure 2.6a. Due to the plasma defocusing effect, after a propagation distance of x in a time t, the wavefront undergoes a tilt by an angle θ, as shown in Figure 2.6b. The on-axis propagation velocity v'_ϕ is different from that of the edge v_ϕ, which can be obtained from the wavefront position:

$$x = v_\phi t = \frac{c}{\eta_p} t = \frac{c}{\sqrt{1 - n_e/n_c}} t \approx c\left(1 + \frac{1}{2}\frac{n_e}{n_c}\right) t, \tag{2.54}$$

whereas the on-axis distance x'due to the electron density $n_e + \delta n_e$ can be described by:

$$x' = v'_\phi t = \frac{c}{\sqrt{1-(n_e+\delta n_e)/n_c}} t \approx c\left(1 + \frac{1}{2}\frac{n_e}{n_c} + \frac{1}{2}\frac{\delta n_e}{n_c}\right) t. \tag{2.55}$$

Comparing (2.54) with (2.55) results in:

$$x' \approx x + c\frac{\delta n_e}{2n_c} t = x + \delta x, \tag{2.56}$$

with the displacement $\delta x = c\delta n_e t/2n_c$. Following, the tilting angle θ for small values can be described by:

$$\theta \approx \tan\theta = \frac{\delta x}{w_0} = \frac{ct}{w_0}\frac{\delta n_e}{2n_c} \approx \frac{x}{w_0}\frac{\delta n_e}{2n_c}. \tag{2.57}$$

Since the laser is being focused at a half-angle Θ, the plasma defocusing is neutralized when $\theta = \Theta$. Thus, considering a propagation distance of $x = 2z_R \approx ct$, the ionization-induced defocusing effect dominates as long as[144]:

$$\theta = 2\frac{\pi w_0^2}{\lambda_L}\frac{1}{w_0}\frac{\delta n_e}{2n_c} > \Theta = \frac{\lambda_L}{\pi w_0} \Rightarrow \frac{\delta n_e}{n_c} > \left(\frac{\lambda_L}{\pi w_0}\right)^2, \tag{2.58}$$

where this condition has a good agreement for regions immediately around the focus position. In practice, ionization-induced defocusing can impair the achievement of the desired laser intensity at the focus. However, as displayed in equation (2.58) this effect can be compensated by going for either a tighter focusing geometry, pre-ionization of the medium target, or choice of a target with fewer ionization levels.

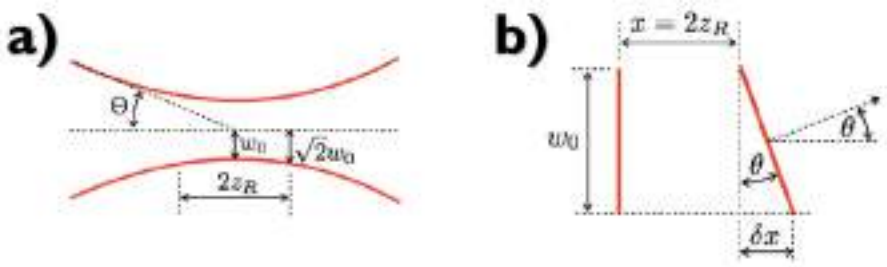

Figure 2.6 – (a) Propagation of a focused Gaussian laser beam at a divergence half-angle Θ and (b) its flat wavefront tilt after a propagation distance $x = 2z_R$.
Source: Adapted from ARUNACHALAM, A. K.[125].

Self-focusing in underdense plasmas

The self-focusing of a laser pulse in underdense plasmas can be a result of two effects: the relativistic increase of the electron mass close to the laser axis, and electrons depletion on the laser axis due to the ponderomotive force. In addition, the self-focusing contributes to a further increase of the laser intensity as well as the focused laser guiding over longer distances than the Rayleigh length z_R.

To investigate the relativistic increase of the electron mass effect during the laser pulse propagation in a plasma, the effects of ponderomotive electron repulsion will be neglected. Considering a linearly polarized laser pulse propagating in an underdense plasma with uniform density, the plasma refractive index can be described in terms of the normalized vector potential:

$$\eta_p = 1 - \frac{1}{2}\frac{\omega_p^2}{\omega_0^2}\left(1 - \frac{a_0^2}{4}\right). \tag{2.59}$$

Moreover, assuming a Gaussian laser pulse (shown in Figure 2.7a) propagating in the uniform plasma, the refractive index described by equation (2.59) increases in the axis of the laser pulse due to its higher intensity, and the corresponding laser phase velocity decreases, as shown in Figure 2.7b. This effect corresponds to a plasma refractive index and a laser phase velocity distribution similar to the propagation through a positive lens, making the pulse undergo self-focusing until it is compensated by natural diffraction.

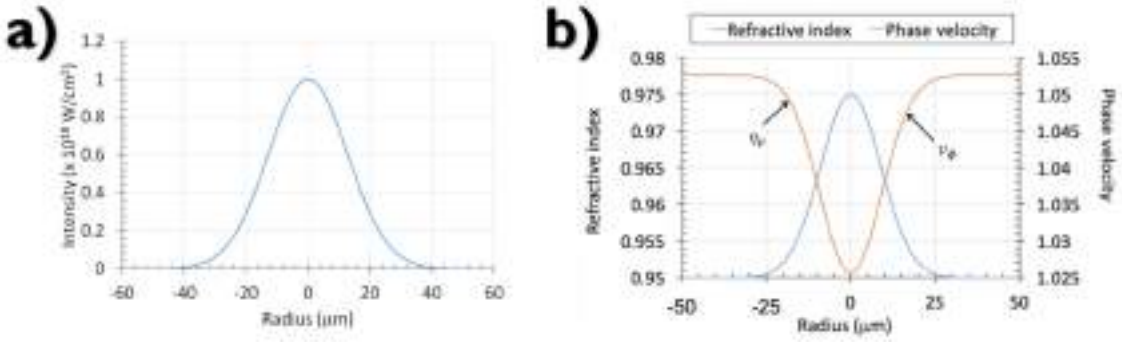

Figure 2.7 – Illustrative changes of plasma refractive index in the self-focusing effect by relativistic electron mass: (a) Laser intensity with a Gaussian radial distribution. (b) Radial distribution of the plasma refractive index (blue line) and laser phase velocity (orange line).
Source: Adapted from ARUNACHALAM, A. K.[125].

This effect is known as relativistic self-focusing (RSF) and its critical laser power, $\mathcal{P}_{RSF}$, can be derived from balancing the natural diffraction of the laser pulse with the self-focusing, where a known result for a laser pulse with a Gaussian radial profile is represented by[124]:

$$\mathcal{P}_{RSF} = \frac{c}{2\pi\varepsilon_0}\left(\frac{e}{r_e}\right)^2 \Longrightarrow \mathcal{P}_{RSF}[\mathrm{GW}] \approx 17.5\frac{\omega_0^2}{\omega_p^2} = 17.5\frac{n_c}{n_e}, \tag{2.60}$$

where $r_e = e^2/4\pi\varepsilon_0 m_e c^2$ is the classical electron radius. For typical high-density LWFA experiments with $n_e = 0.05 n_c$, $\mathcal{P}_{RSF}$ = 350 GW, which is a laser power easily reached by near TW-class laser systems. These considerations have also been experimentally demonstrated for hydrogen targets[145], where for laser peak powers $\mathrm{P}_L < \mathrm{P}_{RSF}$ the

ionization-induced defocusing effect dominates, and for $P_L > P_{RSF}$ the relativistic self-focusing takes over.

To understand the second self-focusing caused by the ponderomotive force, is essential to remember that this force originates from the laser pulse nonuniform intensity distribution during its propagation in an underdense plasma, and it acts from higher to lower intensity regions (Section 2.3). For a high-intensity laser pulse, this force is strong enough to radially expel the electrons from the axis and form an electron depleted channel, as illustrated in Figure 2.8a. Thus, the resulting plasma refractive index can cause different parts of the laser pulse to undergo ponderomotive self-focusing at varying degrees. In the steady-state limit, the laser pulse is guided by the electron density distribution across the cavity, as illustrated in Figure 2.8b. The electron depletion in the central focal region acts as a positive lens for the laser pulse propagation[146]. It is noteworthy that although each self-focusing effect has a different mechanism, experimentally both self-focusing effects are basically indistinguishable from one another.

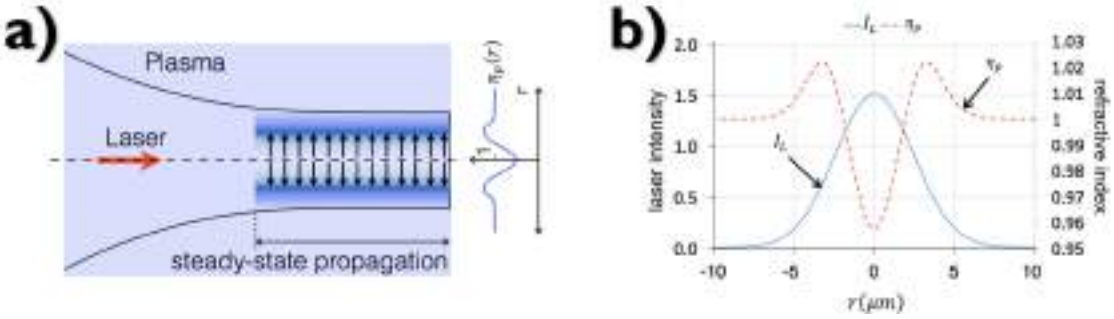

Figure 2.8 – Illustrative representation of ponderomotive self-focusing effect: (a) schematic representation of the electron cavity formation due to the ponderomotive expulsion of the electrons in the laser focal position, and (b) electron density variation (red line) across the cavity in the steady-state limit corresponding to a laser intensity with a Gaussian profile (blue line).
Source: Adapted from ARUNACHALAM, A. K.[125].

Self-phase modulation

When a laser pulse is focused into a gaseous target, the pulse leading edge ionizes the gas atoms, and the subsequent laser propagation in an underdense plasma depends on the interdependent evolution of the plasma electron density and the laser intensity. The change in the instantaneous frequency of the laser pulse due to the intensity dependent plasma refractive index in the longitudinal direction is known as self-phase modulation (SPM). This effect can be understood as analogous to self-focusing on the longitudinal direction in the plasma, and it can be investigated by assuming that the linearly polarized

laser pulse envelope and the longitudinal electron density profile remain unchanged in the co-moving reference frame of the laser pulse, thus the instantaneous plasma refractive index $\eta_p(\tau)$ can be described by:

$$\eta_p(\tau) = \eta_{p,0}(\tau) + \eta_{p,2}(\tau) I_L(\tau) = \underbrace{1 - \frac{1}{2}\frac{n_e(\tau)}{n_c}}_{\eta_{p,0}(\tau)} + \underbrace{\frac{1}{8}\frac{n_e(\tau)}{n_c} a_0^2(\tau)}_{\eta_{p,2} I_L(\tau)}, \tag{2.61}$$

where $I_L(\tau)$ refers to the laser intensity in the co-moving reference frame, $\eta_{p,0}$ corresponds to the linear contribution of the refractive index, while $\eta_{p,2}$ is the nonlinear contribution for $a_0 < 1$. Otherwise, for $a_0 > 1$, $\eta_p(\tau)$ has to be modified accordingly to equation (2.53).

The phase shift $\phi(\tau)$ accumulated by different parts of the laser pulse after a propagation distance L can be given by:

$$\phi(\tau) = \phi_0 + \omega_0 \tau + \phi_{SPM}(\tau), \tag{2.62}$$

where ϕ_0 is the initial phase shift, ω_0 is the central frequency, and ϕ_{SPM} refers to the accumulated phase shift due to the instantaneous plasma refractive index $\eta_p(\tau)$, which can be expressed by:

$$\phi_{SPM}(\tau) = \frac{2\pi}{\lambda_0} \int_0^L \eta_p(\tau) dx, \tag{2.63}$$

from where the instantaneous laser frequency $\omega(\tau)$ can be described in the following form:

$$\omega(\tau) = \frac{d}{d\tau}\phi(\tau) = \omega_0 + \frac{d}{d\tau}\left[\frac{2\pi}{\lambda_0}\int_0^L \eta_p(\tau) dx\right] = \omega_0 + \underbrace{\frac{2\pi}{\lambda_0} L \frac{d}{d\tau}\eta_p(\tau)}_{\delta\omega(\tau)}, \tag{2.64}$$

where $\delta\omega(\tau)$ is the instantaneous frequency change caused by the ionization and self-phase modulation effect[125]. These changes can be visualized in Figure 2.9 on the temporal and frequency domains of a Gaussian laser pulse during its propagation through an underdense plasma; Figure 2.9a shows that during the laser pulse leading edge, the electron density has been assumed to steadily increase and after the peak intensity, it remains constant, neglecting the ponderomotive effects; Figure 2.9b shows the refractive index profile in the co-moving reference frame and the instantaneous frequency change after a propagation distance in plasma; Figure 2.9c shows the corresponding self-phase modulated electric field of the laser pulse, where the frequency modulation is evident; Figure 2.9d shows the SPM broadened spectrum.

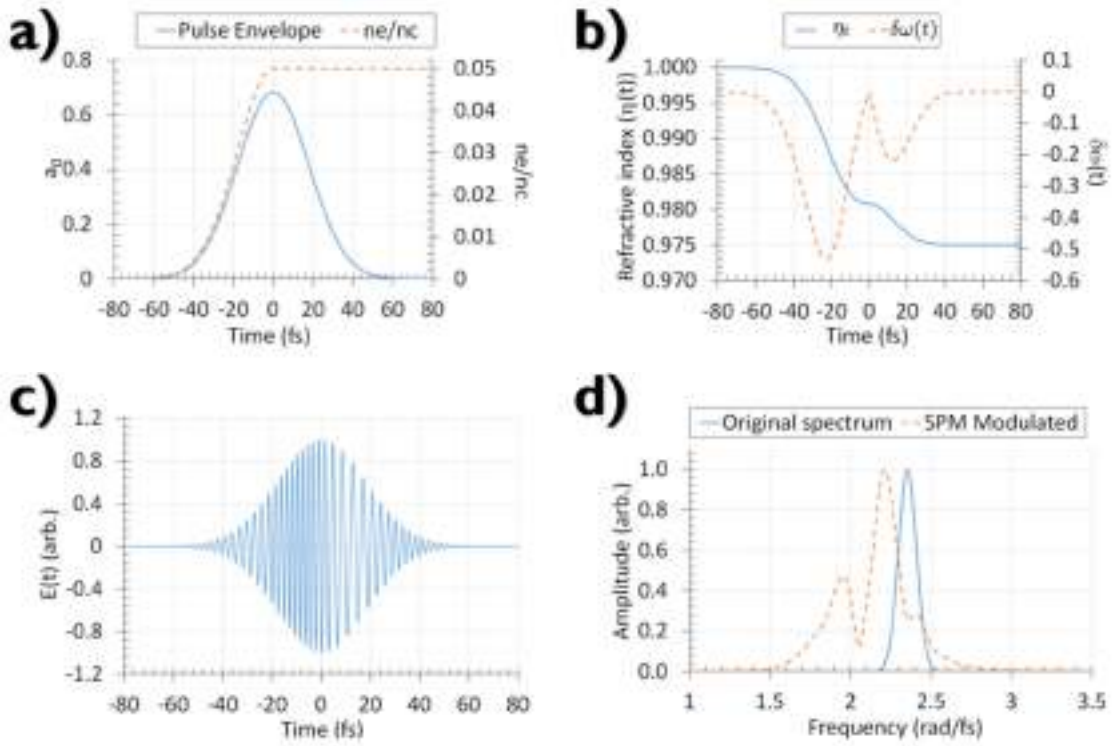

Figure 2.9 – Illustrative representation of self-phase modulation effect during the laser pulse propagation in an underdense plasma: (a) laser pulse envelope intensity profile along with the corresponding electron density profile. (b) the variation of the refractive index profile and the laser instantaneous frequency. (c) the modified electric field of the laser pulse after the propagation of in plasma. (d) the unmodulated (original) and self-phase modulated spectrum of the laser pulse after the propagation in plasma.
Source: Adapted from ARUNACHALAM, A. K.[125].

2.6 Plasma wakefield generation

As previously described, when an intense laser pulse propagates through an underdense plasma, its ponderomotive force pushes radially the electrons from the ionic background. Since the ions remain stationary, a restorative electric field pulls the electrons back, thus establishing electron density oscillations at the trail of the laser pulse, a so-called plasma wave with a frequency ω_p. As far as the laser pulse propagates with its group velocity v_g through the underdense plasma, it continues to push the electrons away from higher intensity regions, leading to a plasma wave with a relativistic phase velocity $v_\phi \approx v_g$ (close to the laser pulse envelope). This process will evolve to create laser-generated wakefields in the plasma, and it can be derived from an analysis in the one-dimensional (1D) nonlinear regime and modeling the plasma as a cold fluid[124, 126], as described in this section to reduce the complexity. Thus, assuming the quasi-static approximation (QSA) in which the laser pulse does not evolve over the transit time of the

plasma, and can be represented as a function of the coordinate $\xi = x - v_g t$ in the co-propagating frame, the generation of 1D plasma waves in the cold fluid limit can be described by:

$$\frac{1}{k_p^2}\frac{\partial^2 \Phi}{\partial \xi^2} = \gamma_g \left\{ \frac{v_g}{c}\left[1 - \frac{1+a^2}{\gamma_g^2 (1+\Phi)^2}\right]^{-1/2} - 1 \right\}, \tag{2.65}$$

where k_p is the plasma wave number, Φ is the electrostatic wake, a is the normalized potential vector, $\gamma_g = \sqrt{1 - v_g/c}$ is the Lorentz factor associated with the group velocity of the plasma wave. If the laser group velocity is close to the speed of light ($v_g \approx c$), the equation (2.65) can be reduced to[126]:

$$\frac{1}{k_p^2}\frac{\partial^2 \Phi}{\partial \xi^2} = \frac{1}{2}\left[\frac{1+a^2}{(1+\Phi)^2} - 1\right]. \tag{2.66}$$

Solving the differential equation (2.66) for the wake potential, some wakefield properties can be calculated, including the longitudinal electric. Figure 2.10 presents two numerical solutions for the equation (2.66) corresponding to the wakefield generated by linearly polarized laser pulses with low intensity ($a_0 = 0.3$, Figure 2.10a) and high intensity ($a_0 = 3$, Figure 2.10b), both plots using a plasma with an initial density of $n_{e,0} = 10^{18}$ cm^{-3}. In addition, the laser intensity plotted as the square of the normalized laser potential function a^2, and the plasma density and the longitudinal electric field are normalized. It is worth noting that in the high-intensity case ($a_0 > 1$), the plasma wave is strongly nonlinear and the characteristic electron density spikes are formed with almost linear electric fields between them.

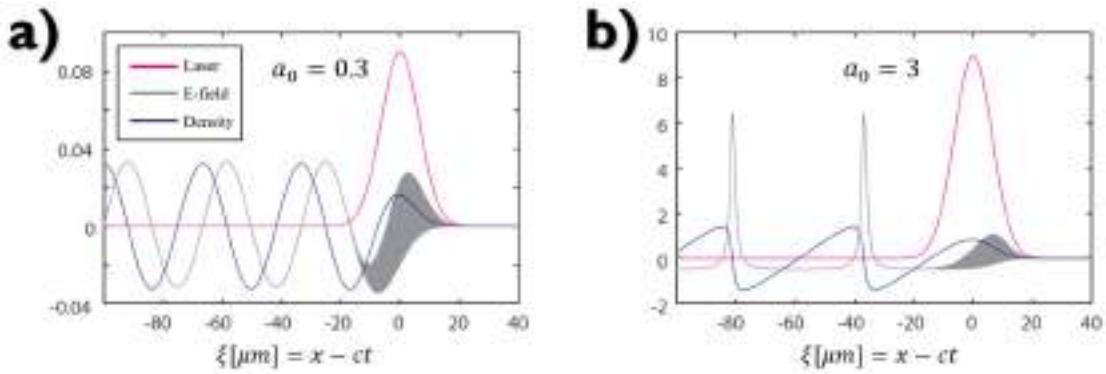

Figure 2.10 – Plasma wakefield formation from a laser-driver with Gaussian temporal profile with a duration of 50 fs (FWHM). The plots show the laser intensity (magenta line), the density profiles (gray line), and the longitudinal electric field profile (blue line). The horizontal axis represents the relative position of the laser pulse.
Source: Adapted from PLATEAU, G.[140].

This ability to generate longitudinal electric fields makes plasmas an attractive medium for electron acceleration. However, the longitudinal electric field cannot reach infinitely large amplitudes. When the plasma group velocity (velocity of the electrons composing the plasma) becomes equal to the phase velocity of the plasma wave, a singularity is formed in equation (2.66), which in practice corresponds to an overlap between the trajectories of neighboring charges occurs[138]. This is the point where the wakefield no longer can increase and breaks down. This process is called longitudinal wave-breaking and it defines a limit to the maximum electric field supported by the plasma wave. For the non-relativistic cold wave-breaking limit[147] this electric field is:

$$E_{wb,0}[V/m] \approx \frac{m_e \omega_p c}{e} = 96\sqrt{n_{e,0}[\mathrm{cm}^{-3}]}. \tag{2.67}$$

Otherwise, for relativistic velocities, a new limit for the wave-breaking electric field in cold relativistic plasmas described initially by Akhiezer and Polovin[148] takes place as:

$$\frac{E_{wb}}{E_{wb,0}} \approx \sqrt{2\left(\frac{\omega_0}{\omega_p} - 1\right)} \propto \frac{1}{\sqrt{\omega_p}}. \tag{2.68}$$

Nevertheless, in warm plasmas the electrons have higher initial velocities and can travel out of the high-density spike below the cold wave-breaking limit, being self-trapped in the plasma wave. This new limit for the wave-breaking electric field in relativistic warm plasmas was derived from the warm relativistic fluid theory[149, 150], and is given by:

$$\frac{E_{wb,th}}{E_{wb,0}} = \left(\frac{4}{27}\frac{m_e c^2}{T_e}\right)^{\frac{1}{4}}, \tag{2.69}$$

where T_e is the electron temperature in eV. For instance, assuming a plasma with a density n_e = 10^{19} cm^{-3} and temperature T_e = 200 eV, as well as a laser pulse with a_0 = 2, the maximum longitudinal electric field can be compared for the three wave-breaking limits by equations (2.67), (2.68), and (2.69), as presented in Table 2.1.

Cold non-relativistic plasma	**Cold relativistic plasma**	**Warm relativistic plasma**
$E_{wb,0}$ = 300 GV/m	E_{wb} = 1470 GV/m	$E_{wb,th}$ = 1320 GV/m

Table 2.1 –Wave-breaking electric field limits for different plasma regimes estimative at a plasma with n_e = 10^{19} cm^{-3} and T_e = 200 eV, and laser pulse at a_0 = 2.
Source: Adapted from SÄVERT, A.[126].

To summarize, the relativistic effects increase significantly the wave-breaking field in comparison with the non-relativistic regime although the longitudinal electric field, even

for the non-relativistic regime, is already adequate for electron acceleration experiments. However, it is worth mentioning that in more realistic approaches with 2D or 3D geometries using PIC simulations, the transverse effects can lead to wave-breaking at lower wakefield amplitudes[126, 151].

2.7 Laser wakefield acceleration

Tajima and Dawson have proposed[14] that the ponderomotive force of a strongly focused laser pulse can excite a plasma wave that travels with a relativistic phase speed. They have also demonstrated that although a high a_0 is required to create a wakefield efficiently, it is also necessary to achieve a match condition between the laser pulse length and the plasma waves wavelength. This resonance condition can be expressed by:

$$c\tau_L = \frac{\lambda_p}{2}, \tag{2.70}$$

where the λ_p is the plasma wavelength and $c\tau_L$ is the laser pulse length, being τ_L the pulse duration (FWHM). Under these conditions, if electrons are trapped inside of the spatial-temporal plasma density oscillations (such as a surfer catching an ocean wave), those electrons can be accelerated up to a few GeV over a few centimeters[30] by the longitudinal electric field (wakefield) created by the charges separation, as illustrated in Figure 2.11. Besides the wave-breaking as a mechanism to self-trap electrons, other methods also are explored, such as colliding pulse[152, 153], ionization induced[27, 154], shock wave[155, 156], and density-ramp injection[157, 158].

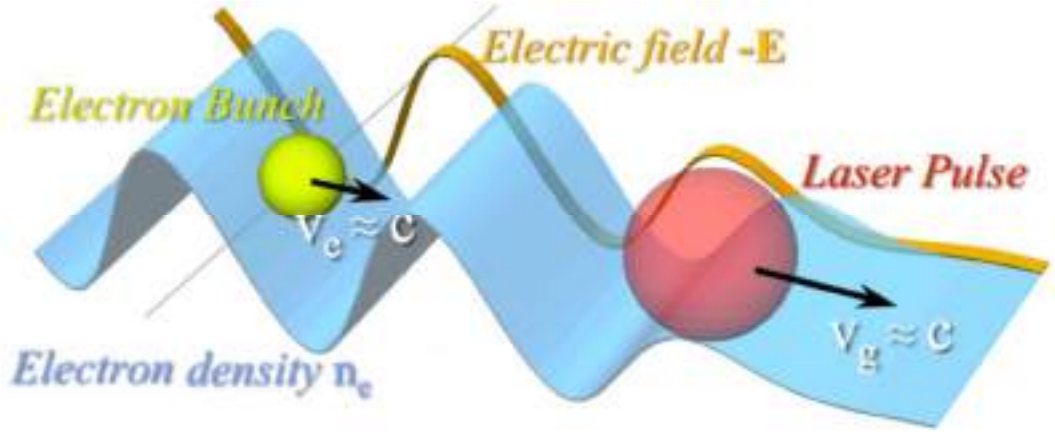

Figure 2.11 – Scheme of the laser wakefield acceleration, where the leading edge of the intense laser pulse creates a plasma wave capable to trap the electron bunch, which is further accelerated by the longitudinal electric field in the direction of laser propagation.
Source: Adapted from LIN, J.[127].

The laser-driven electron acceleration in underdense plasmas is a process known as laser wakefield acceleration (LWFA) and it can be operated in different regimes. The most efficient is the so-called blowout regime (or bubble regime)[22, 25], which operates at high nonlinear wakefield ($a_0 \gg 1$) and close to the resonance condition expressed by equation (2.70), as well as with the focus radius (beamwaist) also close to $\lambda_p/2$. These spatial requirements can be reached by adjusting the size of the focal spot using the appropriate focalization optics, while the temporal condition can be obtained using a plasma density that matches the pulse duration. Furthermore, as shown in Figure 2.10b, for a high-intensity laser pulse, the plasma wake spikes have large amplitude as well as a longitudinal sawtooth-like electric field. These changes in the plasma wave allow a new definition for the plasma wavelength for a high nonlinear wakefield, such as LWFA in the blowout regime. Thus, the nonlinear plasma wavelength $\lambda_{p,nl}$ is given by[159]:

$$\lambda_{p,nl} = \frac{2\lambda_p}{\pi}\frac{E_{max}}{E_{wb,0}}, \tag{2.71}$$

where E_{max} is the maximum electric field amplitude of the nonlinear wakefield. This lengthening of the plasma wavelength has an important effect on the transverse shape of the 3D nonlinear plasma waves. Due to the Gaussian intensity profile of the laser pulse, the wave is driven more strongly on-axis, which results in a curved wavefront of the plasma wave. Thus, for an intense nonlinear wakefield, the volume behind the laser pulse becomes depleted of electrons, forming a so-called ion bubble. This blowout regime (bubble regime) presents a stable accelerating structure due to the longitudinal electric field; meanwhile, the laser electric field (focusing field) decreases with the radial distance. These characteristics promote acceleration dynamics that can generate quasi-monoenergetic electron (QME) bunches with high energy and low divergence, suitable as particle sources in several applications[37, 41]. Figure 2.12 presents a 3D PIC simulation illustrating the blowout regime and an analogy related to a surfer surfing the wave generated by a boat.

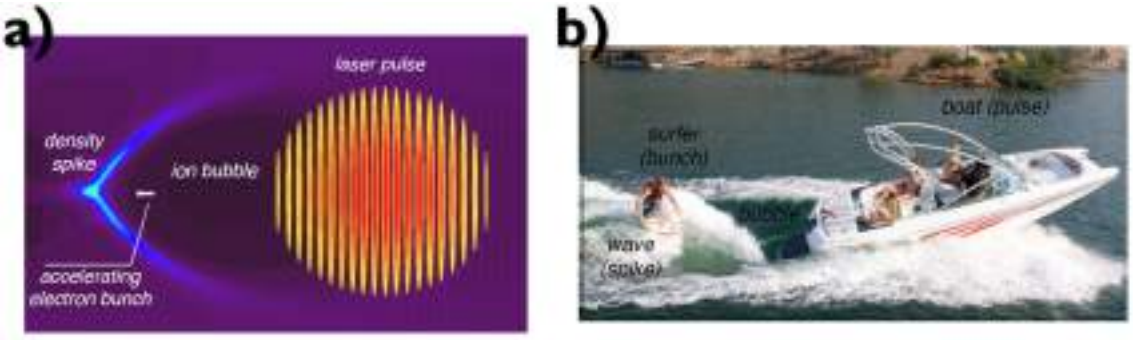

Figure 2.12 – Analogy between (a) a typical PIC simulation of LWFA operating in the blowout regime and (b) a surfer surfing the wave generated at the back of a boat.
Source: Adapted from PLATEAU, G.[140].

For a laser pulse longer than the plasma wavelength ($c\tau_L > \lambda_p$), the LWFA can be made possible by another mechanism outside of the resonance condition, the so-called self-modulated laser wakefield acceleration (SM-LWFA) regime[22, 55]. This regime can be reached even starting from a non-relativistic laser intensity ($a_0 < 1$), provided that the pulses surpass the critical power for relativistic self-focusing, $\mathcal{P}_{RSF}$ (equation (2.60)), what can be obtained by increasing the plasma density. Once this condition is met, this self-focusing increases the laser intensity to relativistic values ($a_0 > 1$). In the SM-LWFA, the laser pulses undergo a self-focusing effect that promotes laser instabilities as stimulated Raman[55]. These perturbations can periodically change the laser pulse group velocity yielding a modulation in its intensity profile, leading to the growth of spectral side bands $\omega_0 + n\omega_p$ and $\omega_0 - n\omega_p$ (with n as an integer) scattered by the plasma waves. This process increases the amplitude of the longitudinal plasma waves and breaks the pulse intensity profile into a train of shorter pulses separated by λ_p, as already illustrated in Figure 1.2. Thus, since the short pulses are resonant with the plasma wavelength, they are capable to accelerate electrons. In practice, although SM-LWFA experiments can be operated at lower laser intensities, usually the electron bunches have high charges but are no longer QME, do not have low divergence, and are no more energetic than in the blowout regime.

2.8 Electron acceleration limits

Although plasmas can sustain longitudinal electric fields with amplitudes over GV/m, as discussed in Section 2.6, the electrons cannot be accelerated and gain energy infinitely. The final electron energy is determined by the interaction between the accelerating field and how far this field can be sustained. There are different effects

capable of limiting the acceleration field extent as well as the electron energy gain. In this Section, those effects are discussed individually along with analytical expressions derived from the 1D approach[126].

2.8.1 Diffraction

Due to the high laser intensities requirement to drive LWFA experiments, the laser pulses are focused on the target. As a consequence of the diffraction, outside the confocal parameter $b = 2z_R$ the laser spot size increases rapidly and, consequently, the laser intensity quickly drops. Although self-focusing effects can lengthen the focal region, it does not extend it to many z_R. Thus, the electron acceleration length cannot be sustained for long distances, and the diffraction limits the energy gain. Nonetheless, some experimental methods have been investigated for extending the acceleration length by external guiding structures with a preformed plasma channel before the arrival of the laser-driver pulse[160, 161].

2.8.2 Laser depletion length

A portion of the laser energy is required to create and sustain the plasma waves. While the leading edge of the laser pulse ionizes the target and interacts with the plasma formed, the trailing edge resides within the ionic channel. This spatial variation of the electron density along the pulse envelope etches away the pulse starting from its leading edge with a velocity $v_{etch} = c\omega_p^2/\omega_L^2$, moving the leading edge backwards. Thus, the laser pulse is depleted after a depletion length L_{depl}, given by[22, 162]:

$$L_{depl} = \left(\frac{\omega_L}{\omega_p}\right)^2 \frac{c\tau_L}{a_0^2}, \qquad \text{for } a_0 < 1, \tag{2.72}$$

$$L_{depl} = \left(\frac{\omega_L}{\omega_p}\right)^2 c\tau_L, \qquad \text{for } a_0 > 1. \tag{2.73}$$

When the laser pulse loses a substantial portion of its energy, the plasma wave amplitude decreases, and the electron acceleration process is terminated. In addition, a sharp shape of the laser pulse leading edge, as well as the formation of a plasma density spike, can be observed at the depletion position[126].

2.8.3 Dephasing length

Usually, the electron bunches travel with velocities close to the speed of light c, while the plasma wave propagates with the same group velocity of the laser pulse, which is slightly less than c. Once the electrons travel faster than the plasma waves, after some distance within the acceleration region they will enter into a deceleration region, as can be understood by referring to Figure 2.13. This dephasing between the electrons and plasma waves can be expressed in terms of the electrons propagation distance until the dephasing takes place. For the blowout regime, this dephasing length L_{deph} can be described by[22, 162]:

$$L_{deph} = \frac{\lambda_p^3}{\lambda_L^2}, \qquad \text{for } a_0 < 1, \tag{2.74}$$

$$L_{deph} \approx \frac{2}{3\pi}\frac{\lambda_p^3}{\lambda_L^2}\sqrt{a_0}, \qquad \text{for } a_0 > 1. \tag{2.75}$$

It is noteworthy that the dephasing length is longer for lower density plasmas since $\lambda_p \propto 1/\sqrt{n_e}$, which makes low-density targets more attractive to reach higher energies. Furthermore, the dephasing effects usually dominate over depletion ones to limit the energy gain, and the depletion length only overtakes for high laser intensities ($a_0 \gg 1$). For the blowout regime using the resonance condition $c\tau_L \approx \lambda_p/2$, this comparison is easily observed by the ratio $L_{deph,r}/L_{depl,r} \approx 4\sqrt{a_0}/3\pi$, valid for $a_0 > 1$.

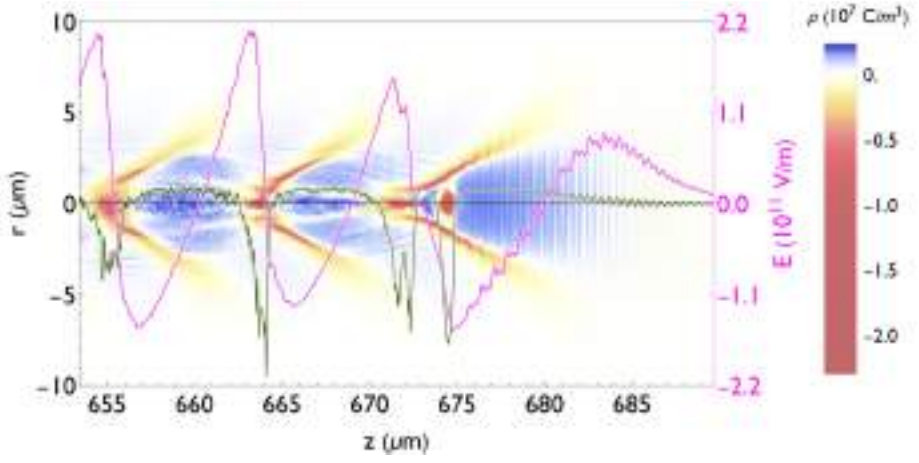

Figure 2.13 – Charge density distribution on the laser polarization plane in a typical LWFA PIC simulation. The dark green line represents the on-axis density, and the pink line is the on-axis longitudinal electric field (wakefield), created by the charge distribution. An accelerated electron bunch can be observed inside the first ionic cavity, around 674 µm, where the wakefield is negative, accelerating the electron bunch forward; for $z > 680$ µm the wakefield is positive, defining a deceleration region for the bunch. The dephasing length for this ionic cavity is $L_{deph} \approx 7$ µm, from ~673 µm to ~680 µm.
Source: By the author.

2.8.4 Maximum energy gain

The electron maximum energy gain in the wakefield, W_{max}, can be determined by the acceleration length and the acceleration field E_{acc}. Assuming that $L_{deph} < L_{depl}$ for typical experimental parameters, the W_{max} can be described by[22]:

$$W_{max}[\mathrm{MeV}] = eE_{acc}L_{deph} \approx 630\,\frac{I_L[\mathrm{W/cm^2}]}{n_e[\mathrm{cm^{-3}}]} \times \begin{cases} 1 & \text{for } a_0^2 \ll 1 \\ 2N_p/\pi & \text{for } a_0^2 \gg 1, \end{cases} \quad (2.76)$$

where N_p is the number of plasma periods behind the laser pulse. The equation (2.76), as well as the other analytical expressions presented in this section, were derived in the 1D approach for plasma wakes. Although these expressions provide a good picture of the LWFA mechanisms, more realistic 3D approaches can significantly change these expressions. Thus, particle-in-cell (PIC) simulations have been largely explored in this field to better understand, predict, and interpret experimental results. Such simulations can predict experimental results with good accuracies, such as electron bunch energy distribution, charge, and divergence. Chapter 3 is dedicated to discussing the PIC simulation, where a brief theory is presented along with some results obtained by our research group to motivate the subsequent experimental results also discussed in this thesis.

3 PARTICLE-IN-CELL SIMULATIONS

In this chapter, particle-in-cell (PIC) simulations are briefly discussed, with an initial theoretical description of the method, followed by the motivation for using PIC codes to predict experimental possibilities from the viable infrastructure in our laboratory at IPEN, and some PIC simulation results that lead off the subsequent experimental activities described in this thesis. It is noteworthy that I personally did not perform PIC simulations during the development of this work, although I have participated in their discussions with other members or collaborators of our research group. However, since the PIC simulations were crucial for establishing the aims of my PhD, the existence of this chapter becomes also crucial to a better understanding of the next ones.

3.1 Introduction to particle-in-cell algorithms

Particle-in-cell (PIC) computational codes are algorithms developed to study the interaction in 3D systems with many particles, such as plasmas. These codes simplify the interactions by clustering a large number of particles in so-called cells (or macroparticles) evaluated according to their weight, and the interactions occur between each defined macroparticle, saving significant computational processing resources[163]. PIC algorithms usually discretize the space into a grid, while keeping the electric and magnetic fields (both electromagnetic and originated by charges) continuous, and then calculate the response of the macro particles in its self-consistent field. This process is repeated in each timestep of the simulation, which establishes several iteration cycles between the fields and the collective behavior of the particles. Figure 3.1 shows a flowchart of an interaction cycle, where: (1) the fields $\boldsymbol{E}$ and $\boldsymbol{B}$ are gathered from the grid for the macro particles position $\boldsymbol{x_i}$ and added to external fields, as those from a laser pulse; (2) the particles respond to the total fields using the motion equations with their positions $\boldsymbol{x_i}$ and momenta $\boldsymbol{p_i}$; (3) the charge density ρ and current $\boldsymbol{j}$ f the macro particles are calculated from $\boldsymbol{x_i}$ and $\boldsymbol{v_i}$, and the particles are placed at their new positions in the grid; finally, (4) the fields $\boldsymbol{E}$ and $\boldsymbol{B}$ are pushed in time.

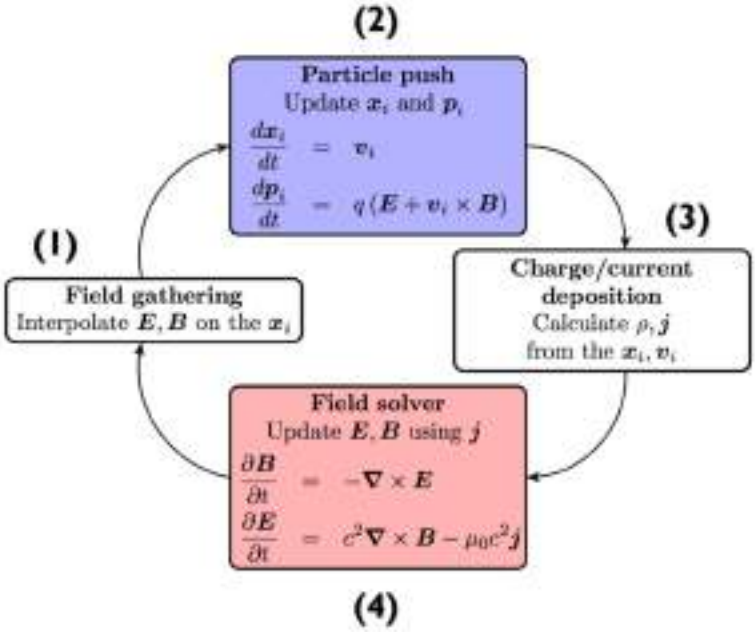

Figure 3.1 – Scheme of the self-consistent interaction of macro particles and electromagnetic fields in a discrete timestep, where the variables related to the macro particles $\boldsymbol{x_i}$ and $\boldsymbol{p_i}$ as well as the fields $\boldsymbol{E}$ and $\boldsymbol{B}$ are updated in each step.
Source: Adapted from FBPIC algorithm & features website[164].

In our research group, the simulations were performed using a derived PIC algorithm, the Fourier-Bessel particle-in-cell (FBPIC) originally developed by Remi Lehe at Lawrence Berkeley National Laboratory and Manuel Kirchen at CFEL, Hamburg University[164, 165]. This code is developed entirely in Python for studying plasma physics in relativistic regimes, being suitable for LWFA simulations. FBPIC uses an azimuthal Fourier decomposition in a cylindrical geometry that splits the fields into azimuthal powers components defined by two coordinates (r, z), while the macro particles move in 3D Cartesian coordinates. The cylindrical decomposition helps in modeling several of the laser-plasma interactions, which presents a natural azimuthal symmetry. Since the grid calculations are done in only 2D coordinates, the FBPIC code uses less computational resources (time, memory, parallel processors) compared to full 3D Cartesian codes. The amount of computational resources spent also depends on the chosen number of azimuthal modes represented in each grid. A higher number of modes demands more resources, although it improves the modeling of the physical problem. Generally, LWFA simulations use three azimuthal modes.

Another advantage of the FBPIC code is its compatibility with GPU (graphics processing unit) from NVIDIA. GPUs are suitable for parallel processing of the algorithm, as they can run a large number of tasks simultaneously. For typical simulations

and modern hardware, the use of GPUs decreases the processing time by a few orders of magnitude.

3.2 Simulation results for near-TW laser in SM-LWFA regime

In face of the potential of the PIC simulations for predicting LWFA results, our research group and collaborators have explored FBPIC codes with different parameters that attend to our joint efforts. However, the input parameters need to be in accordance with the feasibility in our laboratory, more specifically the Ti:Sapphire laser systems available and under development at IPEN that are discussed in detail in Chapter 4, which are expected to generate ~50 fs pulses, with ~50 mJ of energy. Thus, the simulated laser parameters should have peak powers around 1 TW. From these laser parameters, assuming that the laser pulses are focused to a ~5 µm beamwaist which is experimentally difficult, but it still yields non-relativistic intensity with $a_0 < 1$ according to equation (2.11). In practice, the laser intensity, as well as a_0, should be even lower due to laser energy losses during the focalization. Under the possible laser parameters available at our laboratory, our group must work in the SM-LWFA regime with high-density targets ($n_e >$10^{19} cm^{-3}). In the last years, our research group and collaborators have explored PIC simulations in this regime using laser parameters close to those mentioned above, which have been demonstrating the feasibility to accelerate electrons up to the MeV range.

In 2021, our research group and collaborators published a work[58] using PIC simulations to study the generation of MeV electron bunches in the SM-LWFA regime, driven by a few TW and sub-TW laser pulses. This kind of investigation had already been explored by our group since 2017, motivating the work described in this PhD thesis, and resulting in publications in international conference proceedings[111, 112]. In this section, some outcomes from the publication of 2021 are discussed in order to elucidate the further experimental activities of our group as well as of this thesis.

The simulations were performed using FBPIC, where the local plasma is calculated from the neutral gas using the Ammosov–Delone–Krainov (ADK) ionization model[166] and 3 azimuthal modes. The simulation timestep was Δt = 89 as, and the volume evaluated at each timestep has a radius r = 20 µm and length Δz = 100 µm, being the z-axis the laser propagation direction. The fields $\boldsymbol{E}$ an $\boldsymbol{B}$ are evaluated in a grid that has 3750 points in the longitudinal direction, z, corresponding to 30 points/λ_L, and 600 points in the radial coordinate, r, amounting to 30 points/w_{min} (with $w_{min} \approx 1$ µm being

the diffraction limit). Lastly, the number of particles per cell is 2 along z, 2 along r, and 12 along θ, in accordance with the developer recommendation[165]. This study assumed a 200 µm in diameter supersonic H_2 target produced by a nozzle in a vacuum. The radial density profile of this kind of target can be approximated by a trapezoidal profile[78] with symmetrical ascending and descending ramps and a central plateau. For the simulations of interest for this work, the ramps are 80 µm long, and the plateau has 40 µm, defining a total diameter of 200 µm with 120 µm of FWHM, as shown by the blue line in Figure 3.2. The published work[58] studied the acceleration as a function of the plateau electron density after ionization (among other parameters), and in Figure 3.2shows the case for $n_e = 2\times10^{20}$ cm^{-3}, along with the corresponding local plasma wavelength (red dashed line, disregarding local relativistic and density variation effects during the pulse propagation). The laser pulse propagates through the target center from the position $z = 0$ µm (start of target) and the background (outside the target) was assumed to be an absolute vacuum. Furthermore, once there is only an ionization per atom, the plasma density n_e should be the same as the neutral gas molecular density n_g for saturated ionization.

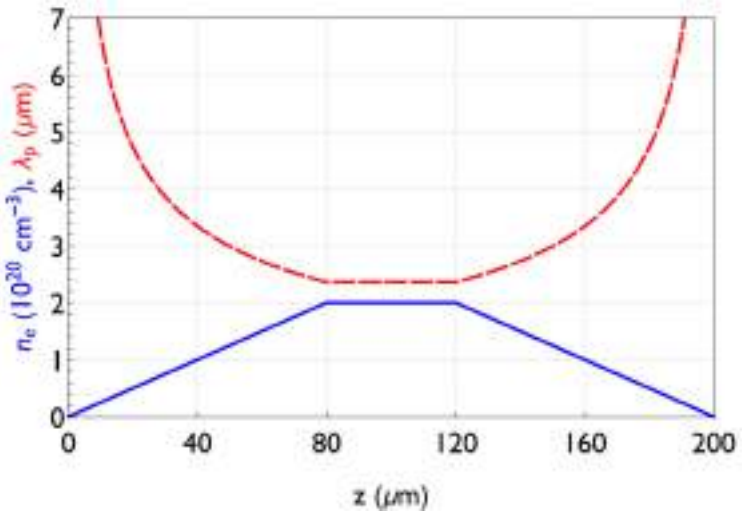

Figure 3.2 – Hydrogen gas target with 2×10^{20} cm^{-3} peak density, where its plasma density distribution after ionization along z-axis (blue solid line) is represented along with the equivalent local plasma wavelength (red dashed line).

Source: Adapted from MALDONADO, E. P., *et al*[58].

The simulated Ti:Sapphire laser pulse has an initial duration of 50 fs (FWHM) and its central wavelength is 800 nm. It is linearly polarized along the x-axis and starts at z = -50 µm. The laser beam is also assumed an ideal Gaussian with $M^2 = 1$, and it was focused on vacuum (without the target influence) at t $z = 40$ µm to a beamwaist

w_0 = 7 µm, which has a value $\sim 9\lambda_L$ and already demonstrated experimentally[56, 57, 62]. Regarding the laser peak power $\mathcal{P}_L$, the simulations were performed using five different values which were ¼, ½, 1, 2, and 4 TW, around the laser power range intended in our laboratory. In addition, the plasma peak densities (plateau density) were also varied in the range from $n_e/n_c \approx 0.006$ to $n_e/n_c \approx 0.8$, similar values to that used in the first SM-LWFA experiments using sub-TW laser pulses[56, 62]. Table 3.1 shows the physical parameters used in the simulations and their variation ranges.

Physical parameter	**Value**
Laser initial pulse duration τ_L (fs)	50
Laser initial peak power $\mathcal{P}_L$ (TW)	¼, ½, 1, 2, 4
Laser wavelength λ_L (µm)	0.8
Laser (MIV) pulse length $c\tau_L$ (µm)	15
Laser (MIV) beamwaist w_0 (µm)	7
Laser (MIV) Rayleigh length z_R (µm)	192
Laser (MIV) normalized vector potential a_0	0.4 – 1.6
Laser (MIV) intensity I_L ($\times 10^{17}$ W/cm²)	3 – 50
Neutral gas molecular density n_g ($\times 10^{19}$ cm^{-3})*	1 – 140
Plasma wavelength λ_p (µm)	1 – 10.5
Plasma dephasing length L_{deph} (µm)	1 – 912

Table 3.1 – Laser and plasma parameters used in the simulations. MIV: measured in vacuum. *Assuming the saturated ionization the plasma density is the same as the gas density ($n_e = n_g$).
Source: Adapted from MALDONADO, E. P., *et al*[58].

The analysis of the simulations results led to a classification of them into three SM-LWFA sub-regimes, which are divided according to their initial laser and plasma parameters. These groups with their characteristics are summarized in Table 3.2. In each group, the self-focusing (SF) and the envelope pulse self-modulation (SM) processes occurred in distinct regions of the target. Although in some configurations the laser peak power is smaller than the critical power for RSF (relativistic self-focusing), self-focusing was observed under these conditions, and can be attributed to ponderomotive self-focusing[167, 168] and classical self-focusing[129]. In addition, only some simulations showed the desired laser self-channeling condition, where the self-focusing and

diffraction effects are counterbalanced to maintain the nonlinear wakefield stability and produce QME bunches. These features yielded different subsequent characteristics of the electron acceleration process as well as electron bunches, which represent the signature of each sub-regimes. It is noteworthy that there is a subtle tradeoff between laser peak powers and plasma plateau densities to reach the proper acceleration conditions capable to obtain desired electron bunches quality.

First group	
Laser and plasma parameters	**Characteristics**
$\mathcal{P}_L$ = ¼ TW, n_e < 5×10^{20} cm^{-3} $\mathcal{P}_L$ = ½ TW, n_e < 2×10^{20} cm^{-3} $\mathcal{P}_L$ = 1 TW, n_e < 1×10^{20} cm^{-3} $\mathcal{P}_L$ = 2 TW, n_e < 0.5×10^{20} cm^{-3} $\mathcal{P}_L$ = 4 TW, n_e < 0.3×10^{20} cm^{-3}	• SF and SM occur in the middle of the exit ramp, exciting a nonlinear wakefield • No significant self-channeling • Bunches duration of few fs or tens fs, and no QME formed • Under same $\mathcal{P}_L$, the maximum electron energy increases with n_e
Second group	
Laser and plasma parameters	**Characteristics**
$\mathcal{P}_L$ = ½ TW, $n_e \in$ [2, 3]×10^{20} cm^{-3} $\mathcal{P}_L$ = 1 TW, $n_e \in$ [1, 3]×10^{20} cm^{-3} $\mathcal{P}_L$ = 2 TW, $n_e \in$ [0.5, 3]×10^{20} cm^{-3} $\mathcal{P}_L$ = 4 TW, $n_e \in$ [0.3, 2]×10^{20} cm^{-3}	• SF and SM occur at the end of the plateau, exciting a nonlinear wakefield • Subsequent self-channeling occurred • Bunches duration of few fs, moderate divergence, and QME • Under same $\mathcal{P}_L$, the maximum electron energy does not change significantly with n_e
Third group	
Laser and plasma parameters	**Characteristics**
$\mathcal{P}_L$ = ¼ TW, $n_e \geq$ 5×10^{20} cm^{-3} $\mathcal{P}_L$ = ½ TW, n_e > 3×10^{20} cm^{-3} $\mathcal{P}_L$ = 1 TW, n_e > 3×10^{20} cm^{-3} $\mathcal{P}_L$ = 2 TW, n_e > 3×10^{20} cm^{-3} $\mathcal{P}_L$ = 4 TW, n_e > 2×10^{20} cm^{-3}	• SF and SM occur at the first half target, leading the laser beam to fade quickly which impairs the nonlinear wakefield formation • Self-channeling did not occur • Bunches duration of several tens of fs, low energy, no QME was observed • Under same $\mathcal{P}_L$ the maximum electron energy decreases with increasing n_e

Table 3.2 – Summary of the SM-LWFA sub-regimes classification from the simulation results.
Source: Adapted from MALDONADO, E. P., *et al*[58].

The best cases belong to the second group, which establishes a regime capable to achieve laser self-channeling, which allowed the formation of a continuous nonlinear wakefield along the entire exit ramp, yielding well-formed QME bunches. This can be better exemplified by analyzing the simulation results of the configuration using $\mathcal{P}_L$ = ½ TW ($a_0 \approx 0.6$) and plasma peak density $n_e = 2\times10^{20}$ cm^{-3} (~$0.1n_c$). This configuration produces a maximum nonlinear wakefield at $z' \approx 140$ µm, where the pulse has a maximum electric field as well as minimum duration (pulse fragment with length $c\tau_L' \approx 1$ µm due to SM), with intensity represented by $a_0' \approx 1.4$ due to SF. Once the electrons are trapped in the wakefield at the beginning of the exit ramp (downramp), they are accelerated along it over an extension that corresponds to most of its length. Although the dephasing length related to the plateau density is only $L_{deph} \approx 10$ µm, a stretching of this distance occurs in the downramp due to the density decrease. Snapshots of the charge density in the x-z plane, $\rho(x, z)$, in the middle of the downramp as well as after the end of the target, where electron bunches can be seen are shown, respectively, in Figure 3.3a and Figure 3.3b. Moreover, Figure 3.3c shows the energy spectrum of all electrons ejected from the target, emphasizing the contribution from the bunch highlighted in Figure 3.3a and b, which has mean energy of $\mathcal{E}_k \approx 8.4$ MeV and width $\Delta\mathcal{E}_k \approx 2.6$ MeV (FWHM), that can be classified as a QME; the remaining electrons present a quasi-exponential distribution with a median of 0.4 MeV. The QME bunch has a charge of $Q \approx 4$ pC, corresponding to 0.4% of the $Q_T \approx 1$ nC total charge ejected. Similar percentages are maintained for other simulations in the second group. Finally, the bunches divergence can be evaluated from the transverse normalized rms emittance in the x and y axes[89] considering all the electrons leaving the target, resulting in $\varepsilon_{x,rms} \approx 11.5$ mm·mrad and $\varepsilon_{y,rms} \approx 9.8$ mm·mrad. When considering only the QME bunch, the emittances drop by almost two orders of magnitude, to $\varepsilon_{x,rms} \approx 0.6$ mm·mrad and $\varepsilon_{y,rms} \approx 0.3$ mm·mrad.

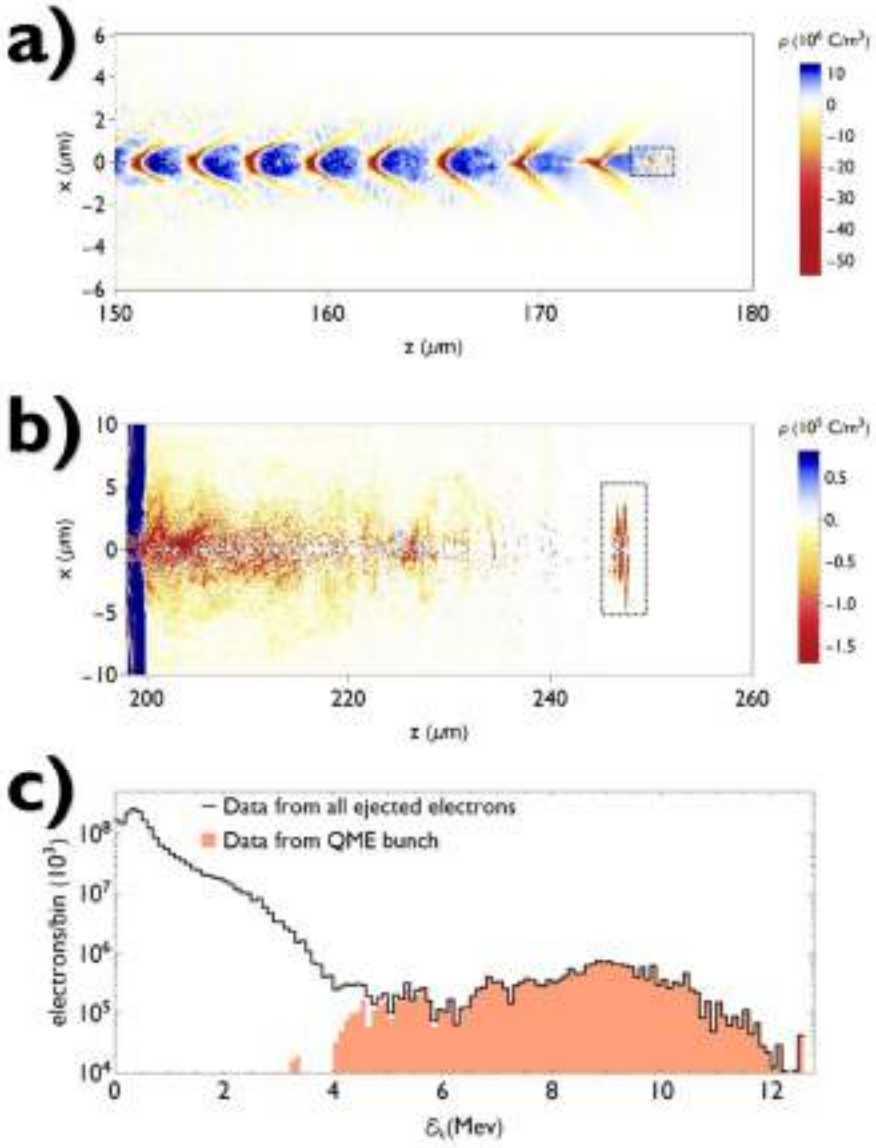

Figure 3.3 – Snapshots of the charge density in the x-z plane from simulation configuration using $\mathcal{P}_L$ = ½ TW and $n_e = 2\times10^{20}$ cm^{-3} where (a) in the middle of the downramp is shown as well as (b) the electron bunches leaving the target with a QME portion highlighted by the dashed rectangle. Part (c) shows the energy distribution of all electrons leaving the target in a histogram with 120 bins over the entire energy range. The highlighted orange region of the spectrum corresponds to the QME electrons.
Source: Adapted from MALDONADO, E. P., *et al*[58].

In addition to the results exemplified in Figure 3.3, other simulations obtained well-formed QME bunches for different laser peak powers and plasma peak densities listed in Table 3.3 shows the best results, where a_0' is the new normalized vector potential amplitude after SF and SM of the laser pulse, Q refers to QME bunch charge, $\mathcal{E}_k$ and $\Delta\mathcal{E}_k$ are, respectively, the QME bunch mean kinetic energy and its width (FWHM), and $\varepsilon_{x,rms}$ and $\varepsilon_{y,rms}$ are the transverse normalized rms emittance in the x-axis and y-axis, respectively. Although these results provide a guide to generate QME bunches in the MeV

scale, it is worth pointing out that the outcomes are dependent on the assumed parameters in this study (density profile, gas species, and focalization of the laser beam), inspired in other experimental realizations of sub-TW SM-LWFA regimes[56, 57, 62].

$\mathcal{P}_L$ (TW)	n_e (10^{20} cm^{-3})	a_0'	Q (pC)	$\mathcal{E}_k$ (MeV)	$\Delta\mathcal{E}_k$ (MeV)	$\varepsilon_{x,rms}$, $\varepsilon_{y,rms}$ (mm·mrad)
0.5	2.0	1.4	4	8.4	2.6	0.6, 0.3
1.0	1.6	2.7	12	11	10	1.8, 5.4
2.0	1.6	4.4	259	4.6	4.6	7.2, 8.3

Table 3.3 – Selected configurations generating well-formed QME bunches obtained at each laser peak power $\mathcal{P}_L$ and a respective plasma peak density n_e.
Source: Adapted from MALDONADO, E. P., *et al*[58].

Figure 3.4 presents the laser peak powers and plasma densities studied in our simulations (hatched region). All simulations with parameters that produced QME electron bunches, even not very well-defined ones, are indicated with dots, allowing the delimitation of a parameters region (inside the dashed line) that should generate QME bunches.

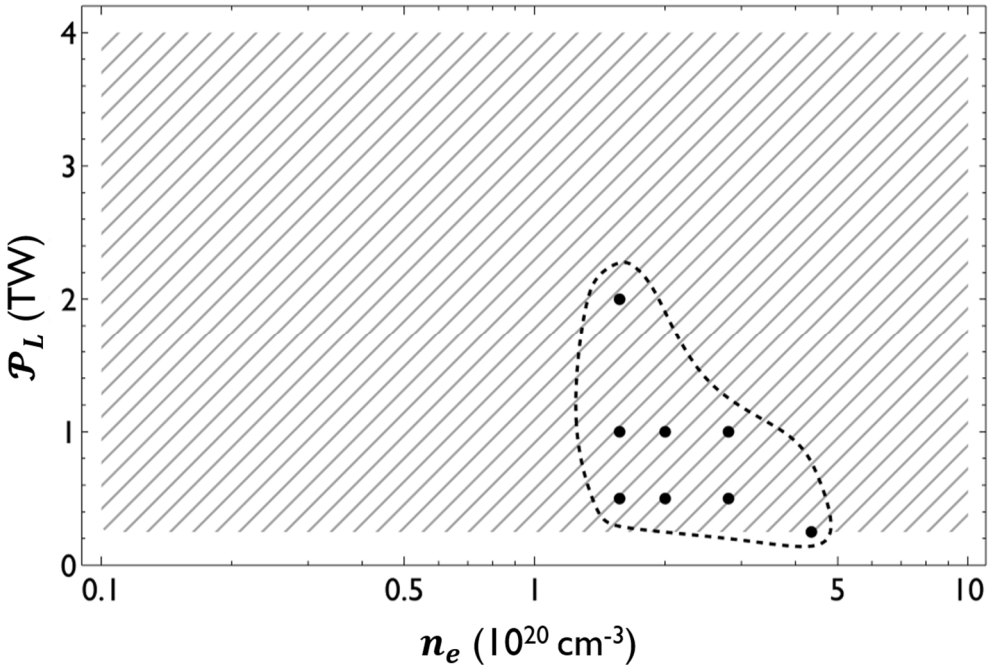

Figure 3.4 – The hatched region represents the simulated laser peak powers ($\mathcal{P}_L$) and plasma densities (n_e). From the QME bunches represented by dots, an interest region could be determined (dashed line) for further theoretical and experimental prospects.
Source: By the author.

From this study, our research group concluded that for laser peak powers in the interval from 0.5 to 2 TW and sub-millimetric targets with optimal peak plasma density around 2×10^{20} cm^{-3}, well-formed QME bunches are produced, with mean energy in the range of 5–11 MeV, widths from 3 to 10 MeV (FWHM), bunch charge being ~0.5% of the total charge, normalized transverse emittances of a few mm·mrad, and low dependence on plasma density variation. These values are following the experimental results using TW and sub-TW SM-LWFA laser pulses[56, 62, 169] that have demonstrated QME bunch charge in the pC range, with fractional charge $Q/Q_T \approx 0.2\%$[56], mean kinetic energy up to 20 MeV with a width from a few to several MeV. Thus, our simulation results motivated and guided our research group for the subsequent experimental activities to attend to the simulation parameter requirements, some of them developed and discussed in this thesis. In addition to the availability of a TW-range laser system that is discussed in Chapter 4, another essential demand is the creation of sub-millimetric, supersonic targets, produced by de Laval nozzles. Chapter 5 is dedicated to discussing the fabrication of micrometric nozzles capable to produce the target conditions as discussed in this section.

4 LASER SYSTEMS

The High Intensity Ultrashort Laser Pulses Laboratory at IPEN has two Chirped Pulse Amplifier[115] (CPA) systems. Those systems are described in detail in this chapter and both can be used for future laser-electron acceleration at IPEN and related experimental activities as further discussed in this thesis. In addition to a better understanding of the laser parameters chosen in our simulations, the laser systems description also is important for understanding the experimental activities of Chapters 5 and 6.

4.1 T-cube

This first laser system, T-cube, will be used by our group to conduct further LWFA studies at IPEN. The laser name refers to a Table-Top Terawatt (T^3) system, once we aim to achieve TW peak power soon. This laser consists of a Ti:Sapphire main oscillator (Mira-Seed, Coherent - item ③ in Figure 4.1) that generates 65 fs (FWHM) pulses centered at 800 nm with 30 nm of bandwidth (FWHM), and 450 mW of average power at 78 MHz. These pulses are injected into a Ti:Sapphire multipass CPA system (Odin, Quantronix – item ④ in Figure 4.1), which stretches the pulses to 30 ps, amplifies them in 8 passes through the gain medium, and compresses them for pulse durations under 50 fs with up to 1 mJ of energy (20 GW of peak power), at repetition rates of 1 kHz and submultiples of it. A programmable acousto-optic dispersive filter[170] (Dazzler, Fastlite) is inserted between the main oscillator and the amplifier, allowing the modulation of the amplitude and phase of the pulse spectrum. This modulation enables the control of the amplified ultrashort pulse temporal profile to optimize its interaction with matter. This 1 mJ energy is barely enough to accelerate electrons, and a second amplification stage is being added to the system. For this, the amplified pulses will be extracted from the CPA before compression and sent into a new Ti:Sapphire amplifier that is under development in our laboratory, or a lamp-pumped Cr:LiSAF amplifier system (item ⑤ in Figure 4.1) already built in our laboratory[171, 172, 173], to generate pulses with a duration of 50 fs with 50 mJ (1 TW power peak) after the compressor (Pulsar - item ⑥ in Figure 4.1), with a

repetition rate under 10 Hz. In the future, both Ti:Sapphire and Cr:LiSAF can be used in tandem to reach higher peak powers.

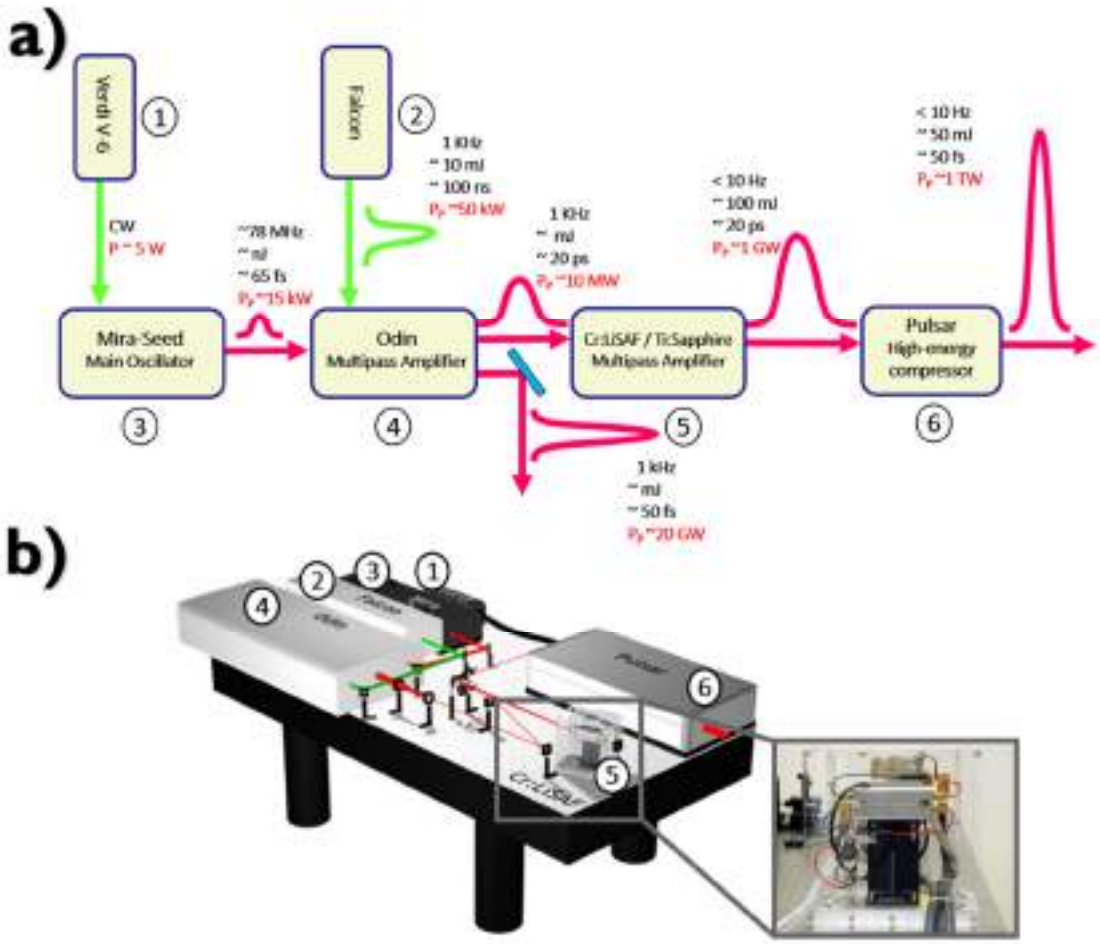

Figure 4.1 – T-cube laser system. After the Odin CPA the pulses have 50 fs, 1 mJ, 1 kHz, and after amplification in Cr:LiSAF and compression in Pulsar the pulses achieved 60 fs, 30 mJ, 10 Hz. Moreover, that system will be upgraded by replacing the Cr:LiSAF with a Ti:Sapphire amplifier that should increase the peak power pulse above 1 TW. (a) The experimental scheme is illustrated and (b) Modeled experimental arrangement where the Cr:LiSAF amplifier is highlighted from a photo.
Source: By the author.

4.2 Femtopower

The second system consists of a Ti:Sapphire main oscillator (Rainbow, Femtolasers -③ in Figure 5.3) that generates laser pulses centered at 785 nm with a duration under 6 fs (FWHM), 370 nm of bandwidth (FWTM), 190 mW of average power at 78 MHz, and carrier-envelope phase (CEP) stabilization system with 250 attoseconds stability. This oscillator is pumped by a Coherent Verdi V6 laser (① in Figure 5.3), which is located inside the main oscillator cover. These pulses are injected into a Ti:Sapphire multipass CPA system (Femtopower Compact PRO CE-Phase HP/HR, Femtolasers -④

in Figure 5.3), which is pumped by an Ascend 60 Q-switched laser (② in Figure 5.3) that generates 300 ns pulses at 532 nm, with 15 mJ (peak power 50 kW), operating at a repetition rate of 4 kHz. During the CPA process, the pulses are amplified in 9 passes through the gain medium and then compressed to less than 25 fs (FWHM) with up to 650 µJ of energy (~26 GW of peak power), centered at 780 nm, with over 40 nm of bandwidth (FWHM), up to 4 kHz repetition rate, and beam with laser quality factor $M^2 \approx 1.2$. This CPA system also can be CEP stabilized. Furthermore, the amplified pulses can be injected into a hollow fiber inside a high-pressure neon chamber (2 bar), where their spectrum is broadened, so the pulses can be compressed to less than 6 fs by an arrangement of chirped mirrors[174], with a pulse energy of 350 µJ (peak power about 60 GW). The CEP stabilization system, of little relevance for the <25 fs pulses, is fundamental in this regime (< 6 fs) and is implemented in the system. Although this laser system has less peak power than the T-cube, laser electron acceleration with 6 fs might be convenient to achieve the blowout regime with pulses of a few cycles, strongly focused to a ~2 µm beamwaist, and at high-density targets. However, this alternative is not a priority for our group since keeping the CEP stabilization in a long and complex beamline is a difficult experimental task. In addition, the peak power of about 60 GW should be low enough to generate MeV electrons since the required densities close to the critical one to reach the relativistic self-focusing, equation (2.60), abruptly decreases the dephasing length L_{deph}.

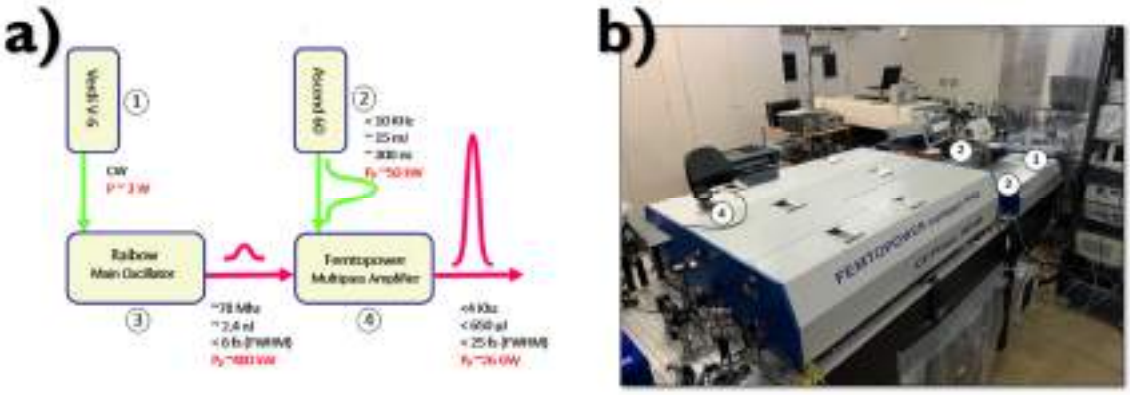

Figure 4.2 – Femtopower laser system, after CPA system the pulses have 25 fs, 650 µJ, 4 kHz, and after hollow fiber held and chirped mirrors the pulse can achieve 6 fs, 350 µJ, 4 kHz. (a) The experimental scheme is illustrated and (b) a photo of the experimental arrangement.

Source: By the author.

Femtopower laser pulses have been largely employed in this thesis, for micromachining the de Laval nozzles (as described in Chapter 5) and in the development of a home-built Mach-Zehnder-like interferometer for pump-probe measurements in gas jets and laser-induced plasma (as described in Chapter 6). Therefore, the characterization of those laser pulses is essential in this work. Figure 4.3 shows the amplified laser pulse spectrum measured by a compact CCD grating spectrometer[175] (Fiber Spectrometer), and the pulse duration measured by an interferometric autocorrelator[176] (Femtometer, Femtolasers). The pulse spectral center of mass is calculated from its spectrum (Figure 4.3a) by:

$$\lambda_{CM} = \frac{\int_{-\infty}^{+\infty} \lambda\, I_L(\lambda)\, d\lambda}{\int_{-\infty}^{+\infty} I_L(\lambda)\, d\lambda}, \tag{4.1}$$

where $I_L(\lambda)$ is the laser intensity spectrum.

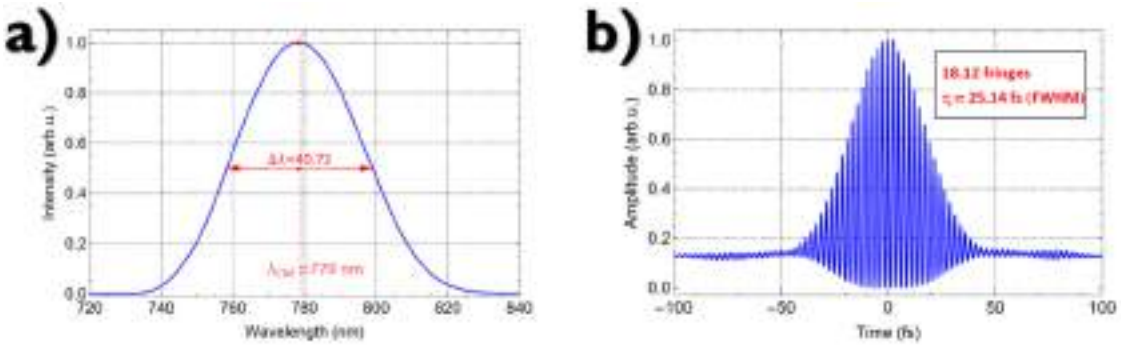

Figure 4.3 – Measurements of the (a) bandwidth $\Delta\lambda_L$ (FWHM), spectral center of mass λ_{CM}, and (b) pulse duration τ_L (FWHM) from Femtopower laser pulses after amplification.

Source: By the author.

5 MICROMETRIC DE LAVAL NOZZLES

According to PIC simulations results[58, 111, 112] and our group proposals[101, 102], there is an urging to generate high-density (~10^{20} cm^{-3}) supersonic gas jets with diameters around 100-300 μm for further SM-LWFA experiments at IPEN. As discussed in Chapter 1, this kind of gaseous target can be generated by de Laval nozzles[50, 70] with exit diameters close to this range. As illustrated in Figure 1.3, these nozzles present a simple converging-diverging geometry capable to accelerate a gas from a high-pressure backing chamber into a supersonic jet at their exits. These supersonic gas jets produce appropriate flat-top targets with well-defined high-density regions, making de Laval nozzles largely explored for laser-plasma interactions experiments such as LWFA. However, a lack of availability of those nozzles with micrometric dimensions makes its fabrication an attractive research topic still little explored in LWFA[77, 78]. In this chapter, the manufacturing method of micrometric de Laval nozzles, developed during this PhD, is discussed along with the characterization of the manufactured nozzle features.

5.1 De Laval nozzle quasi-1D model

Important properties of the supersonic jets generated by de Laval nozzles can be estimated in a first-order approximation by a quasi-1D model[177] that assumes an isotropic flow. Using this model, the ratio between the nozzle exit and throat areas, A_e/A_t, the molecular density drop from the backing chamber to the nozzle exit, $n_g/n_{g,0}$, and the gas jet divergence angle, θ_g (in radians) are obtained as function of the gas Mach number, M, as shown in equations (5.1),(5.2), and (5.3), respectively, while the mass flow rate, $\dot{m}$, only depends on the throat area and the gas properties, as shown in equation (5.4):

$$\frac{A_e}{A_t} = \frac{1}{M}\left[\frac{2+(\kappa-1)M^2}{\kappa+1}\right]^{\frac{\kappa+1}{2(\kappa-1)}} \tag{5.1}$$

$$\frac{n_g}{n_{g,0}} = \frac{1}{M}\left[\frac{\kappa+1}{2+(\kappa-1)M^2}\right]^{\frac{1}{\kappa-1}} \tag{5.2}$$

$$\theta_g = 1/M, \tag{5.3}$$

$$\dot{m} = A_t P_{g,0} \sqrt{\frac{\kappa}{\mathcal{R} T_{g,0}}} \left(\frac{2}{\kappa+1}\right)^{\frac{\kappa+1}{2(\kappa-1)}}, \tag{5.4}$$

where $P_{g,0}$, $T_{g,0}$, and $n_{g,0}$ are the gas pressure, temperature, and molecular density in the backing chamber, $\mathcal{R}$ is the specific gas constant, and $\kappa = c_P/c_V$ is the ratio of the specific heats of the gas at constant pressure, c_P, and constant volume, c_V. The model assumes a cylindrical symmetry, so the areas ratio can be substituted by the squared ratio between the exit and throat diameters. Typically, this model is a good prediction for the gas jet in the immediate vicinity of the nozzle exit, thus the following equations are largely employed as a first approach to design a nozzle[78, 177]. However, although this theoretical model presents satisfactory agreement with experimental results, it does not consider other geometrical features such as the lengths of the converging and diverging sections of the nozzle, their curvatures, and the roughness of the nozzle internal walls; all of these affect the jet profile and are second-order corrections, being better explored by computational fluid dynamic (CFD) simulations[117, 138, 178].

In the quasi-1D model described, it is worth noting that the Mach Number M at the nozzle exit is an important design parameter to manufacture nozzles. It defines the nozzle throat and exit diameters by equation (5.1), capable to generate targets with the desired densities from equation (5.2), and flat-target opening angle from equation (5.3). Figure 5.1 presents two graphs containing the dependence on the Mach Number of the ratio of the nozzle exit and throat areas, A_e/A_t, and of the ratio of the maximum gas density at the nozzle exit and backing chamber, $n_g/n_{g,0}$, for N_2. Both graphs are commonly used as references to determine the nozzle exit and throat diameters based on the Mach number (Figure 5.1a) and gas molecular density (Figure 5.1b).

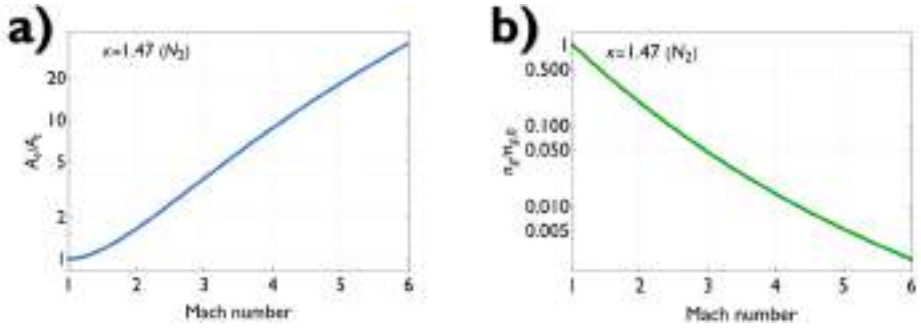

Figure 5.1 – Quasi-1D model dependence on the Mach Number of (a) the ratio between the nozzle exit and throat areas, and of (b) the ratio between the maximum gas molecular density at nozzle exit and backing chamber for N_2.

Source: By the author.

5.2 De Laval nozzle manufacture

To fabricate micrometric de Laval nozzles, different approaches using ultrashort laser pulses micromachining were explored in this work. Ultrafast laser micromachining was chosen because this technique promotes micrometric precision etching while keeping the material properties. This preservation is due to the ultrafast, non-linear interaction of the ultrashort pulses with the matter, which results in an almost non-thermal ablation that does not promote phase transitions in the vicinity of the etched area, producing an almost non-existent heat affected zone (HAZ)[179, 180]. The ablation process in a solid starts when the ultrashort pulse reaches intensities that ionize a significant portion of the material atoms by a nonlinear process. These seed electrons are accelerated into a quivering motion by the pulse electric field, inducing an exponential increase of the free electrons population by impact ionization, a process known as avalanche[179]. This avalanche leads to the material breakdown when the free electrons density reaches ~10^{21} cm^{-3}, corresponding to the critical density for the laser wavelength, at which they become highly absorptive and are heated, then quickly transfer the acquired energy to the surrounding ions within the electron-phonon coupling time, minimizing the ions heating. This relaxation abruptly creates an unstable phase that undergoes a violent adiabatic expansion, called phase explosion[181, 182], which removes material from the surface carrying most of the thermal energy with it, generating a minimal HAZ. The material ablation also can occur due to the ionic Coulomb explosion[183, 184], which results from the charge imbalance caused by the ejection of surface electrons. Both ablation mechanisms can take place simultaneously and their relative contribution depends on the pulse characteristics and on the material, with phase explosion predominating in metals[185]. Furthermore, the seed electrons origin also depends on the material: while in metals they are the conduction band free electrons, in dielectrics and semiconductors those electrons are produced from the valence band by ionization mechanisms such as multiphoton or tunneling ionization[186, 187]. Once the free electrons are present, the exponential avalanche evolves deterministically in almost the same way in all materials[188]. Therefore, ultrafast laser micromachining ensures a non-selective ablation (occurring in any material), where the only essential parameter that has to be known to etch material is its ablation threshold fluence, $\mathcal{F}_{th}$. As a general rule, at the same laser conditions, nonmetallic materials present higher ablation thresholds than metals since a portion of the laser energy is used to ionize the valence band electrons[189].

Ultrashort pulse ablation produces naturally diverging holes due to the focused beam converging geometry and the pulse energy losses as the ablation depth in the material increases[179, 190], producing directly the geometry of a de Laval nozzle. All these features make ultrafast laser micromachining ideal for fabricating nozzles for our experiments. Thus, de Laval nozzles were initially manufactured on metallic substrates using ultrafast laser micromachining by the percussion method[116, 119]. Figure 5.2 presents topographic maps obtained by optical profilometry (Zegage, Zygo Inc.) of a typical nozzle exit and throat on a 0.5 mm thickness copper substrate, manufactured by laser pulses with an energy of $\mathcal{E}_L$ = 150 µJ that were focused by an f = 50 mm achromatic doublet. This method, in conjunction with the low ablation threshold of metals ($\mathcal{F}_{th} \approx 0.05$ J/cm²)[189, 191], produced non-circular and asymmetric holes. This is caused by spatial inhomogeneities in the laser beam arising from deviations from the ideal Gaussian profile and the presence of hot spots, producing a transversal intensity distribution that does not have cylindrical symmetry; this profile is projected on the surface being machined, and ablation occurs inside the isointensity contour defined by the material ablation threshold, resulting in a perforation that follows the beam intensity asymmetric distribution.

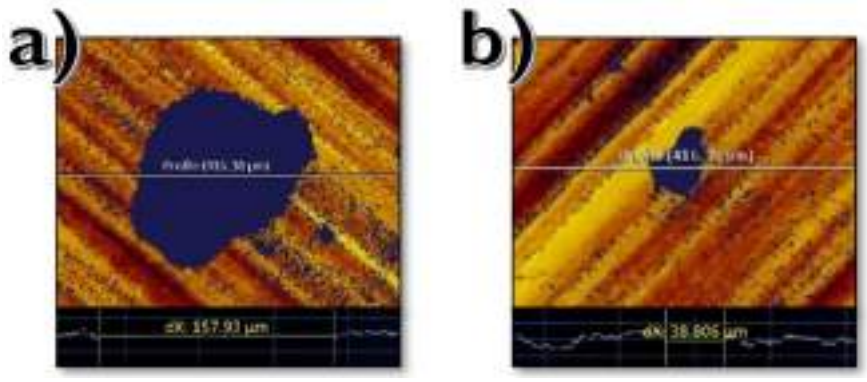

Figure 5.2 – Profilometry maps of a submillimetric de Laval nozzle manufactured on a 0.5 mm thickness copper substrate. (a) $\emptyset_e \approx$ 160 µm exit diameter. (b) $\emptyset_t \approx$ 40 µm throat diameter.
Source: By the author.

The results exhibited in Figure 5.2 lead our group to look for other approaches to manufacture nozzles aiming to get circular holes. This was obtained by modifying the machining process from percussion to trepanning, and replacing the metallic substrates with dielectric materials[116, 180, 192]. The trepanning method rotates the substrate in which the nozzle is being manufactured, while the laser acts as a cutting tool displaced from the rotating axis, smoothing out the laser beam inhomogeneities and preserving the

cylindrical symmetry. Additionally, it allows deeper ablation into the substrate by creating flat surfaces for successive pulses, significantly reducing the loss of energy by reflection at grazing incidence in the etched walls. Meanwhile, replacing the metallic substrates with dielectric ones with two orders of magnitude higher ablation thresholds ($\mathcal{F}_{th} \approx 5$ J/cm²)[189, 193], ensures a more accurate etching since the material is less sensitive to laser intensity fluctuations. The dielectric chosen for fabricating the nozzles was alumina (Al_2O_3) ceramic due to its mechanical properties (high mechanical and flexural strengths, hardness, capable of supporting elevated gas pressures), and availability.

A trepanning setup connected to the Femtopower laser was developed and built. The ultrashort pulses are directed to this setup, shown in Figure 5.3. This arrangement is composed of a rotating DC electric motor coupled to a 3-axis computer-controlled micrometric positioning system (Newport UTS100C) mounted in a XYZ configuration. The motor rotates at ~50 RPM, its axis is parallel to the laser propagation direction, and an achromatic doublet focuses the laser pulses orthogonally to the surface of the substrate holder. Alumina plates with 0.6 mm thickness are placed in the substrate holder, and when the DC motor rotates, the laser etches a circular hole on the alumina surface by trepanning, and after the appropriate time, the laser trespasses the plate, producing a highly circular de Laval nozzle in it. It is noteworthy that before the substrate is etched, some experimental machining parameters must be set for better control of the ablation process. These parameters are discussed in detail in Section 5.3.

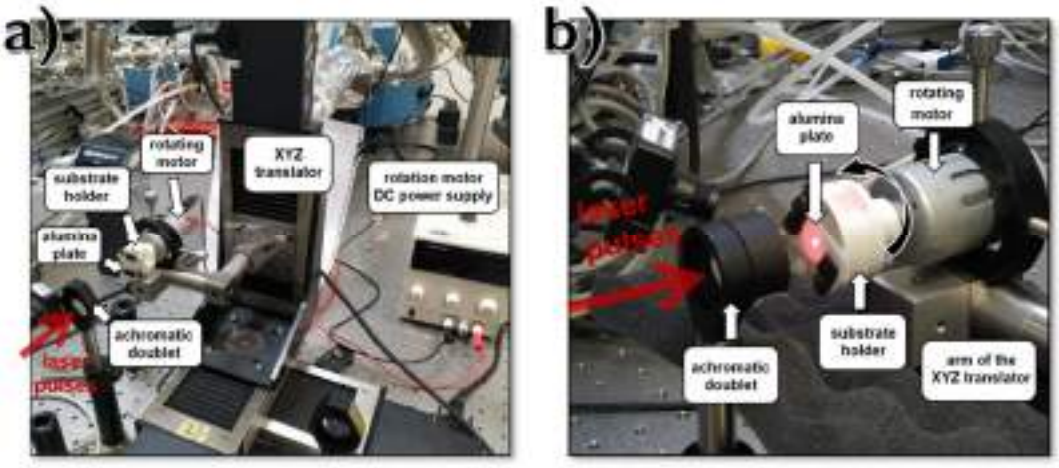

Figure 5.3 – Home-built trepanning setup. (a) rotating motor coupled to the 3-axis micrometric positioning system (XYZ translator). (b) ultrafast laser micromachining on an alumina plate fixed to the substrate holder. In each figure, a different achromatic doublet is shown: (a) f = 75 mm and (b) f = 30 mm.

Source: By the author.

After a de Laval nozzle is etched, the alumina plate is moved laterally by 1 mm, and the laser cuts a 2 mm diameter disk with the nozzle exactly at its center (Figure 5.4a). From the alumina disk, we can characterize the exit and throat diameters and circularity by optical profilometry, and the morphology of the nozzle internal walls by scanning electron microscopy (TM3000, Hitachi Inc). Following these steps, the alumina disk is glued to the tip of a metal part, as shown in Figure 5.4b, using a vacuum compatible epoxy glue (Torr Seal or Hysol) that has a breaking tension above the one exerted in the alumina disk by a pressure of 50 bar. The metal part has a 1 mm hole through it, defining the backing chamber after the tip is connected to the gas line. Figure 5.4c schematizes the nozzles and metallic part projects.

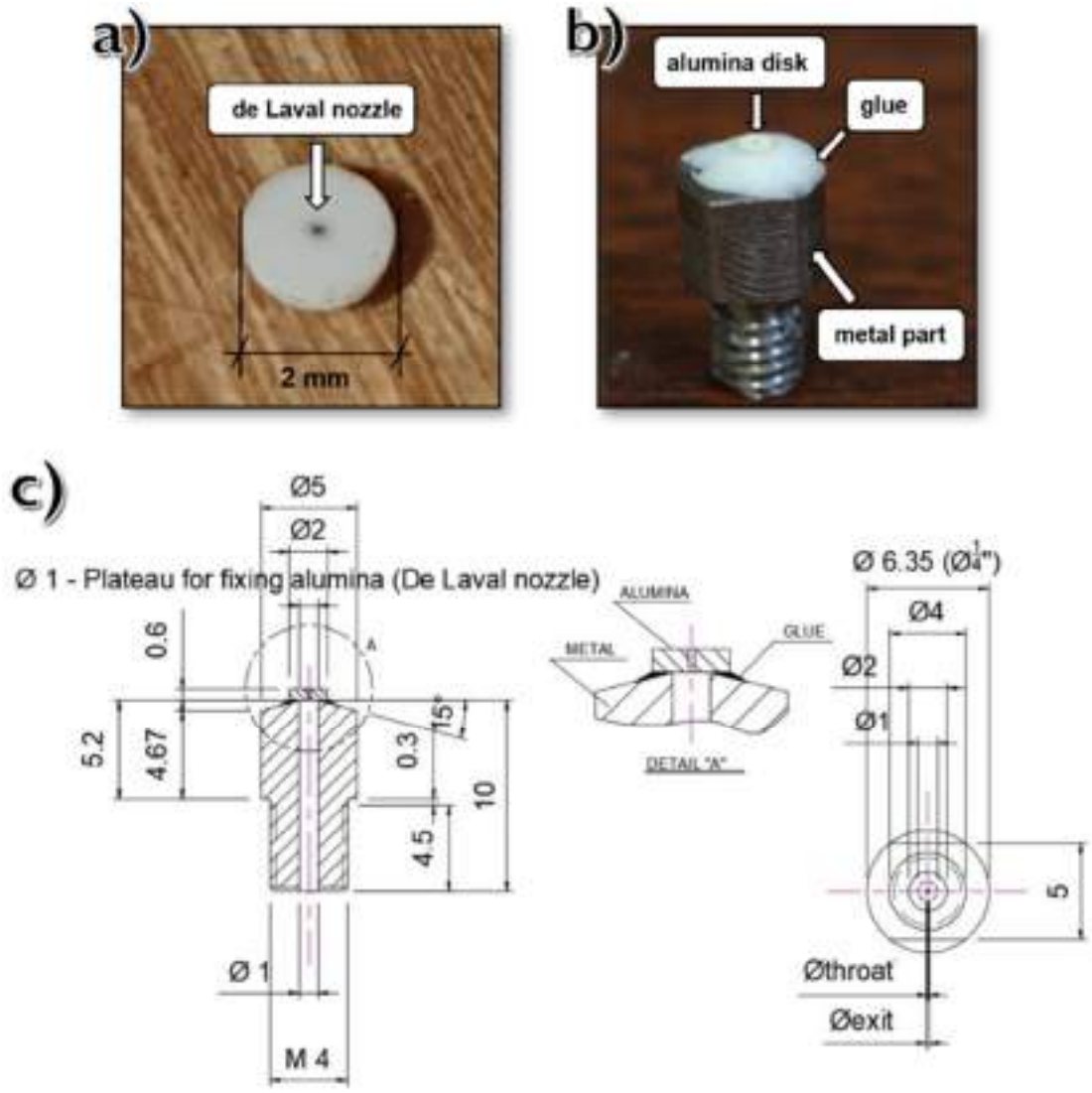

Figure 5.4 – Steps of the gas nozzle preparation: (a) a 2 mm diameter alumina disk with a de Laval nozzle at its center is cut, and then (b) the alumina disk is glued to the tip of the metal part to be connected to the gas line. (c) Project of the de Laval nozzles mount with dimensions in mm.

Source: By the author.

The metal part design, shown in Figure 5.4c, was chosen to be easily connected to a ¼" diameter copper tube (Figure 5.5a) for a continuous gas flow, or to a pulsed valve through a metallic adapter (Figure 5.5b) for controlled gas shots. As discussed in Chapter 6, the gas jets generated by the manufactured nozzles were initially characterized using a continuous flow in atmosphere, and afterwards in pulsed mode, in vacuum, with backing pressures up to 50 bar.

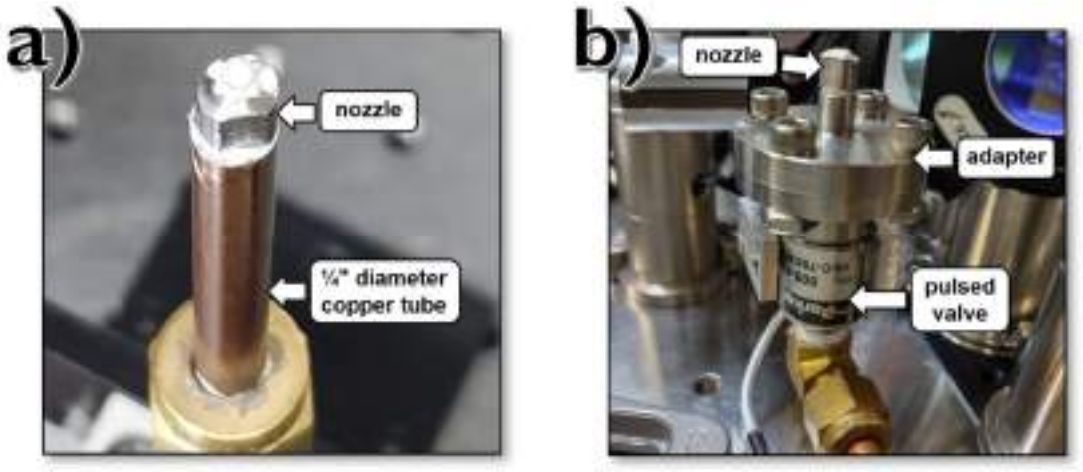

Figure 5.5 – Manufactured nozzle connected to the gas line through (a) a ¼" diameter copper tube and (b) a pulsed valve with a metallic adapter.

Source: By the author.

5.3 Characterization of the manufactured de Laval nozzles

We currently have manufactured more than 40 de Laval nozzles with exit diameters in the range of 120-450 µm, and throat diameters of 15-250 µm, being these values measured from their optical profilometry topographic maps. As exposed in equations (5.1) and (5.2) on a first approximation, the exit and the throat areas of the nozzle define the Mach number, which determines the gas density near the nozzle exit. Our group experimentally observed that the exit and the throat areas depend on the following machining parameters: (1) doublet focal length, (2) laser pulse energy, (3) beamwaist position in the substrate, and (4) exposure time after boring the nozzle. The focal values explored were 30, 50, 75, 150, and 250 mm. Considering the laser beam diameter at the doublet as 8 mm, we could estimate the focused beamwaist for each focal length, evaluating the laser intensity along with the pulse energy value on the substrate during the ablation process. Meanwhile, the laser pulse energies that were explored are in the range of 250-600 µJ. Furthermore, the beamwaist position in the substrate (at its

surfaces, or inside it), determines the laser intensity distribution in the confocal volume, and, consequently, the ablation geometry profile. This parameter is easily controlled by the micrometric positioning system. Finally, the exposure time is also easily controlled by a shutter that blocks the laser pulses. We observed that increasing the exposure time after the laser trespasses the plate enhances the circularity of the exit and the throat, and also improves the internal wall roughness. Thus, before starting the laser micromachining on the alumina substrate, those machining parameters had to be studied to fabricate nozzles with the desired characteristics. The other experimental parameters were kept fixed during this investigation, including the electric motor rotation (~50 RPM) along with the pulse duration (25 fs FWHM) and repetition rate (4 kHz). It is worth emphasizing that during this investigation, a significant accumulated experience about the machining parameters was also due to nozzle fabrication processes that failed, due to reasons such as low intensity that prevented ablation, big exit diameter (> 500 µm), noncircular holes due to laser misalignments with rotation of the machining setup, among others. In this section, nozzle manufacturing results are presented along with a discussion about the four machining parameters explored, aiming to establish protocols to produce micrometric nozzles for further LWFA studies.

The nozzles produced typically have high cylindrical symmetry, demonstrating the high quality and precision of the trepanning machining process, allied to the use of alumina. Figure 5.6 shows the profilometries of the exit ($\emptyset_e$ = 135 µm) and throat ($\emptyset_t$ = 45 µm) for a typical micrometric nozzle. The machining parameters for this nozzle fabrication were 480 µJ pulses focused by the 75 mm focal length doublet, and an exposure time of 15 s after boring the nozzle. During this manufacture, the beamwaist was initially placed in the center of the alumina plate, and during the ablation process, it was progressively moved to the plate back-face to increase the throat diameter. This strategy promotes a significant throat enlargement that yields a higher gas flow, suitable for our proposes. However, the drawback is the decrease in the Mach number.

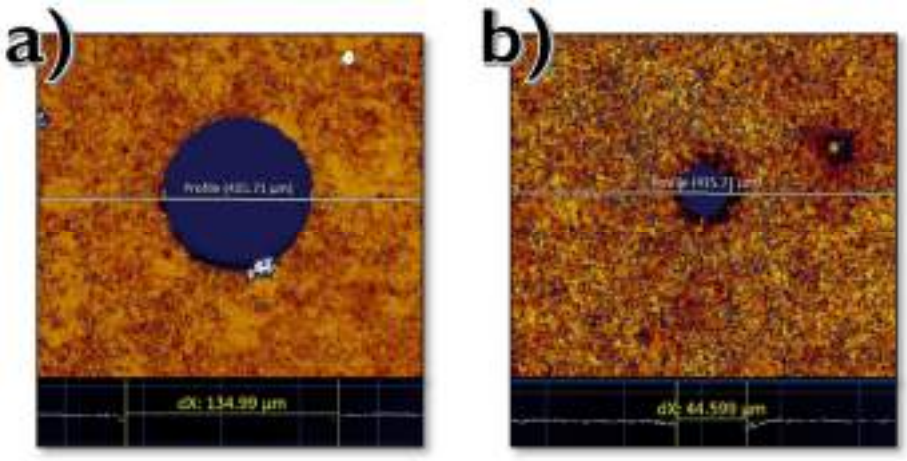

Figure 5.6 – Micrometric de Laval nozzle profilometry. (a) $\emptyset_e$ = 135 µm nozzle exit diameter. (b) $\emptyset_t$ = 45 µm nozzle throat diameter.

Source: By the author.

The nozzle diameters shown in Figure 5.6 result in a Mach number of about 4.0 when using nitrogen (with κ = 1.47), as illustrated in Figure 5.1a, and from equation (5.2) this nozzle produces a gas molecular density of 1.7×10^{19} cm^{-3} at the nozzle exit for a backing pressure of 50 bar, where $n_{g,0} \approx$ (50 bar)×(2.5×10^{19} molecules/cm^{-3}), the latter term being the molecular density of an ideal gas at 300 K and 1 atm and assuming that 1 atm = 1 bar for practical purposes. Although our simulations discussed in Section 3.2 point out to use of simpler gases such as H_2 or He as targets, for the experimental activities discussed in this thesis N_2 has advantages once it presents safer handling than H_2, which is highly flammable, and is less expensive than He. In addition, N_2 presents a higher refractive index than simpler gases[194] that makes its optical diagnostics characterization easier, as discussed in Chapter 6, and recently, successful LWFA experiments were demonstrated using micrometric pure N_2 jets[61, 195]. Regarding the choice of the backing pressure of 50 bar, this value creates targets with adequate plasmas densities for our purposes in conducting SM-LWFA experiments with high-density targets, as well as being the maximum backing pressure tolerated by the pulsed gas valve, also discussed in Chapter 6.

Figure 5.7 exhibits micrographies of another nozzle using scanning electron microscopy (SEM). Both the nozzle exit ($\emptyset_e$ = 170 µm) and throat ($\emptyset_t$ = 30 µm) are visible in Figure 5.7a. This de Laval nozzle was manufactured by 400 µJ pulses, an achromatic doublet with f = 30 mm, the beamwaist position in the center of the alumina plate, and 30 s of exposure time. The structures inside the nozzle are debris that are easily

removed by ultrasound cleaning, and the nozzle internal walls are very smooth, with smaller roughness than that of the alumina surface, which is clearly observed in the exit nozzle edge exhibited with higher magnification in Figure 5.7b. Those characteristics indicate a change in the alumina structure during the ablation process probably due to the melting and ressolidification of the ceramic grains[116, 196, 197], a consequence of residual heat due to elevated pulse energy and high repetition rate. The ressolidification melts the alumina grains[198], and the surface tension of the liquid phase formed flattens its surface, producing low roughness and smooth walls, which should decrease turbulences in the gas jet.

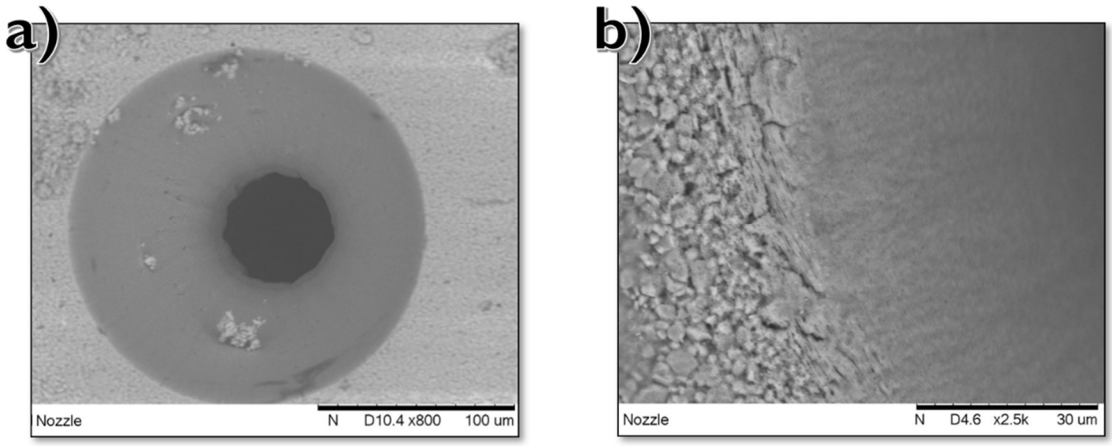

Figure 5.7 – SEM micrographies of de Laval nozzle with $\emptyset_e$ = 170 µm and $\emptyset_t$ = 30 µm. (a) view of the entire nozzle. (b) detail of the nozzle exit edge, highlighting its smooth walls with smaller roughness than the alumina surface.

Source: By the author.

Regarding the machining dependence on the achromatic doublet focal length, the best results were obtained using f = 75 mm, which presents a good relation in achieving the laser intensity needed for ablation, as well as distributing this intensity volumetrically inside the 0.6 mm thick in order to bore it. The investigation points out that intensities above 10^{15} W/cm^2 are needed to bore through the alumina plate due to the energy loss during the machining process (grazing incidence). Thus, the smaller focal length doublets (30, 50, and 75 mm) are more suitable for etching the substrate since they can easily exceed this intensity with the used pulse energies ($\leq$ 600 µJ). Additionally, the focal length has another crucial role in establishing the confocal volume into the substrate, which corresponds to how the intensity of the laser is distributed in the alumina plate. Thus, the shorter lenses define smaller confocal parameters such as ~0.1 mm (f = 30 mm) and ~0.3 mm (f = 50 mm), which are under half of the alumina plate thickness.

Therefore, when using these doublets, the beamwaist should be placed at the center of the plate to reach a condition to bore it, and small pointing fluctuations of the laser can impair the manufacture. The f = 75 mm doublet produces a ~0.6 mm measured confocal parameter, close to the alumina thickness, allowing more reproducibility and different beamwaist positions in the substrate for the manufacture. We even manufactured nozzles with doublets of f = 150 and f = 250 mm, but the reproducibility was not good, and the time to bore the nozzle could surpass 1 hour due to the smaller intensities.

As the machining process is strongly dependent on the achromatic doublet focal length to achieve the proper intensity to bore the alumina plates, it impacts the laser pulse energy. Therefore, for the doublet of f = 75 mm, the best results (smaller nozzle exit and throat diameters, high circularity, and smooth walls) were obtained using $\mathcal{E}_L \approx 400$ µJ, being the same pulse energy value also observed for f = 50 mm. However, for doublets with f = 30 mm, the energy was $\mathcal{E}_L \approx 300$ µJ, and for longer focal lengths (f = 150 mm) more than 500 µJ were needed.

Concerning the beamwaist position in the alumina plate, when it is positioned at the plate front-surface (processing laser entrance, corresponding to the nozzle exit), the laser hardly bored the alumina plate due to the decreasing intensity inside the plate (beam divergence) and the energy losses during the ablation. Moving the beamwaist to the plate back surface (processing laser exit, nozzle throat), an increase in the exit and throat diameters was obtained, producing, usually, an exit diameter above the desired value (> 200 µm). The smallest diameters were produced when the beamwaist was positioned at the center of the alumina plate, resulting in the best energy distribution inside the substrate. We could observe that the gas jets generated by the nozzles manufactured with this strategy exhibit a smaller Mach number than the theoretically predicted by equation (5.1). The reason for this comes from the curvature of the nozzle diverging section that, in second-order approximation, affects the jet Mach number. Figure 5.8 presents a SEM micrography of the cross-section of a de Laval nozzle cleaved along its length. This nozzle was fabricated with the beamwaist positioned in the center of the alumina plate, which contributed to shape the nozzle as a convex trumpet, the curvature that presents the smaller Mach number for a given throat and exit diameters ratio[199]. Recently, we started to manufacture de Laval nozzles initially positioning the beamwaist at the center of the plate, and quickly moving it to the plate back surface (nozzle throat), as done with the nozzle exhibited in Figure 5.6. This new strategy contributes to a change in the nozzle

shape, approaching it to a concave bell, the curvature that generates higher Mach numbers[199].

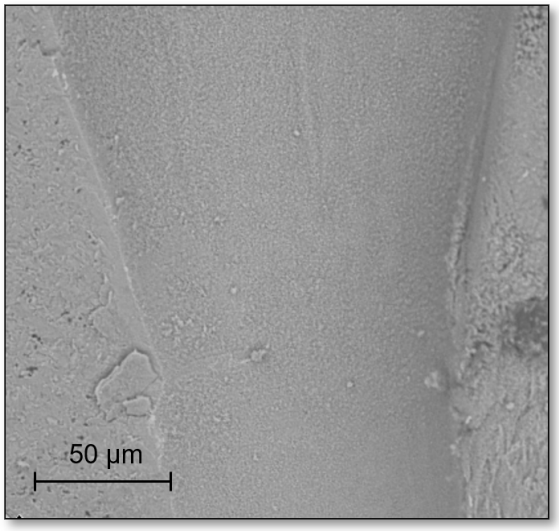

Figure 5.8 – SEM micrography of the transversal profile of a de Laval nozzle manufactured with the beamwaist at the center of the alumina plate.

Source: By the author.

The last machining parameter explored was the exposure time after boring the nozzle. This parameter proved to be crucial for improving the smoothness of the nozzle internal walls by the probable melting and ressolidification process. In order to create a very smooth wall with low roughness, exposure times above 10 s are needed for the typical machining parameter used in this work. Figure 5.9 shows two manufactured nozzles with similar exits and throats diameters ($\emptyset_e \approx 160$ µm and $\emptyset_t \approx 40$ µm) and similar machining parameters (f = 30 mm, ~400 µJ, and beamwaist positioned in the center of the alumina plate), except for the exposure time after boring the nozzle. In Figure 5.9a this exposure time was 30 s and in Figure 5.9b was only 3 s. For the smaller exposure time, the nozzle internal walls present periodical structures created by the trepanning micromachining, which were not smoothed by the melting and ressolidification process due to the lower exposure time. Thus, this investigation concluded that the residual heat necessary for the melt and ressolidification is more present after the nozzle is bored, since the exchange of temperatures between the plasma and atmosphere air becomes more frequent, increasing the ressolidification occurrences.

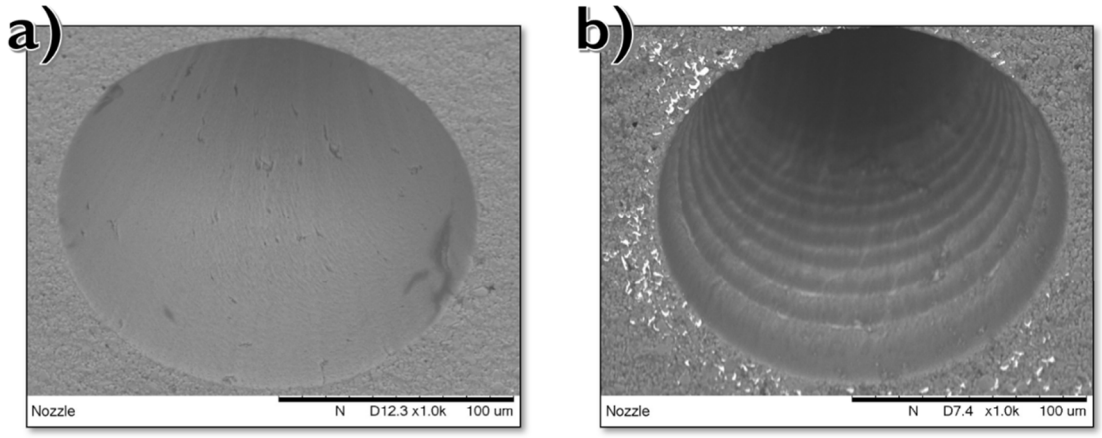

Figure 5.9 – SEM micrographies of nozzles manufactured with a) a long (30 s) and b) a short (3 s) exposure time after boring the nozzle.
Source: By the author.

Based on the outcomes of this investigation, a good set of machining parameters for manufacturing nozzles adequate to our goals is f = 75 mm, $\mathcal{E}_L \approx 400$ µJ, beamwaist initially positioned at the center of the alumina plate and then quickly moved to the plate back surface, and exposure time after boring the nozzle > 10 s. A more complete investigation also would study the contributions of those parameters in the machining process, which could provide a different protocol for micrometric nozzles fabrication. However, for our group goals requirements this investigation proved to be adequate, obtaining de Laval nozzles with desired diameters ranges and very smooth internal walls.

The next step in nozzle characterization is to verify if their supersonic gas jets obey the theoretical predictions as well as the target requirements in our simulations for SM-LWFA experiments. Chapter 6 is dedicated to discussing the implementation of interferometric techniques to diagnose these targets.

6 INTERFEROMETRY DIAGNOSTIC

As mentioned in Chapter 1, after the fabrication of micrometric de Laval nozzles, the next step is to develop non-disturbing optical techniques to characterize the supersonic gas jets and, subsequently, laser-induced plasmas created in these jets. During this PhD, our group decided to explore interferometry as the main diagnostic method for the targets once this technique provides a well-accurate density profile, which is valuable information for characterizing LWFA systems, and providing data for PIC simulations. This chapter is dedicated to discussing the efforts for establishing a time-resolved interferometric setup in our laboratory at IPEN, to characterize the density of gas targets and of laser-induced plasmas during their temporal evolution, covering also an original investigation about the plasma evolution in air.

6.1 Interferogram analysis to retrieve the density information

An interferometer consists, typically, of a laser that is split into two beams: one propagates through the sample under investigation, and the second beam is the reference. Among different interferometer designs, the split can occur before the interaction with the sample, which results in two arms named diagnostic (DIAG) and reference (REF) beams, as in Michelson, Fizeau, and Mach–Zehnder interferometers[93, 200]. In another class of configurations, known as shearing interferometers, there is only one beam, which propagates through the sample and is splitted after it, and an undisturbed part of the beam is used as a reference, like in biprisms and Nomarski interferometers[93, 201]. Independently of the configuration details, the sample imprints a phase shift on the beam that propagates through it, and when this beam is recombined with the reference one, the accumulated phase produces a bending (shift) in the interference fringe pattern[200].

The analysis of an interferogram containing a sample, such as a gas jet or a plasma (typical targets in LWFA), to determine its density distribution requires a mathematical procedure that can be computationally implemented using various algorithms. A common workflow used to retrieve the target density starts obtaining two interferograms, one containing the target information, and another one (reference) of the same region, but without the target, and then selecting the same region of interesting (ROI) in both

interferograms. Assuming the presence of disturbances such as optical irregularities and airflow, which add unwanted phases, the bi-dimensional interferograms fringes intensity distributions containing the target, I_{tar}, and the reference, I_{ref}, information can be described, respectively, by the following equations[202]:

$$I_{tar} = I_{bg} + I_{fr} \cos [\phi_{car} + \phi_{dis} + \phi_{sam}], \tag{6.1}$$

$$I_{ref} = I_{bg} + I_{fr}{}' \cos [\phi_{car} + \phi_{dis}], \tag{6.2}$$

where I_{bg} is the background intensity and I_{fr} is the interference fringes intensity envelope, which differs between equations (6.1) and (6.2) due to the target presence. The terms within the cosines are originated from the phase accumulated in the sample (target), ϕ_{sam}, which will provide the target density distribution, the laser wavelength (carrier) phase, ϕ_{car}, and the unwanted disturbances phase, ϕ_{dis}. Both interferograms are transformed to the frequency domain by 2D fast Fourier transforms (2D-FFT), which yield the intensities $\hat{I}_{tar}$ and $\hat{I}_{ref}$. Then, in each 2D frequency map, Gaussian filters are applied over the region that contains only the target fringes information[202], eliminating the background intensity frequencies. Bidimensional inverse fast Fourier transforms (2D-IFFT) are then applied to each filtered map, which returns new 2D complex maps of the interference fringes in the spatial domain, defined as I'_{tar} and I'_{ref}. The phase information contained in the argument of those new maps can be extracted by the ratio between its imaginary ($\Im$) and real ($\Re$) parts according to:

$$\phi_{tar} = \phi_{car} + \phi_{dis} + \phi_{sam} = tan^{-1}\left[\frac{\Im(I'_{tar})}{\Re(I'_{tar})}\right], \tag{6.3}$$

$$\phi_{ref} = \phi_{car} + \phi_{dis} = tan^{-1}\left[\frac{\Im(I'_{ref})}{\Re(I'_{ref})}\right]. \tag{6.4}$$

Once the phase information in each map is extracted, to obtain the accumulated phase (integrated phase along the probe beam path) related to the gas jet, $\Delta\phi$, is necessary to subtract (6.4) from (6.3) as[202, 203]:

$$\Delta\phi = \phi_{tar} - \phi_{ref} = \phi_{sam}. \tag{6.5}$$

The FFT algorithms produce phase data within the 2π range, due to the use of tangent functions in equations (6.3) and (6.4), generating phase discontinuities, which should be corrected using phase unwrapping algorithms[204]. The 2D maps obtained by the described methods contain the whole accumulated phase (integrated phase) by the

DIAG beam propagation through the target, here defined as the x direction. This definition results in the accumulated phase map in the yz-plane, denoted by $\Delta\phi(y,z)$.

Assuming an axisymmetric (cylindrically symmetric) target, such as a gas jet as illustrated in Figure 6.1, the integrated phase along the x-axis is sufficient to reconstruct the radial phase $\Delta\varphi_r$ using techniques such as the Abel inversion method[203, 205]:

$$\Delta\varphi_r = -\frac{1}{\pi}\int_r^{\infty} \frac{d\Delta\phi}{dx}\frac{dx}{\sqrt{x^2-r^2}}, \tag{6.6}$$

where $r = \sqrt{x^2+z^2}$, according to the coordinates as defined in Figure 6.1. The radial phase $\Delta\varphi_r$ is generally used considering that imperfections in the cylindrical symmetry of real targets are second-order corrections and can be neglected. It is noteworthy that the unit of the radial phase shift $\Delta\varphi_r$ is rad/m. Otherwise, for targets with non-cylindrical symmetry, there are more complex techniques, such as variations of Abel inversion for non-symmetric targets[206] and tomographic methods[207, 208] that combine measurements of the target along different axes to provide more realistic phase maps.

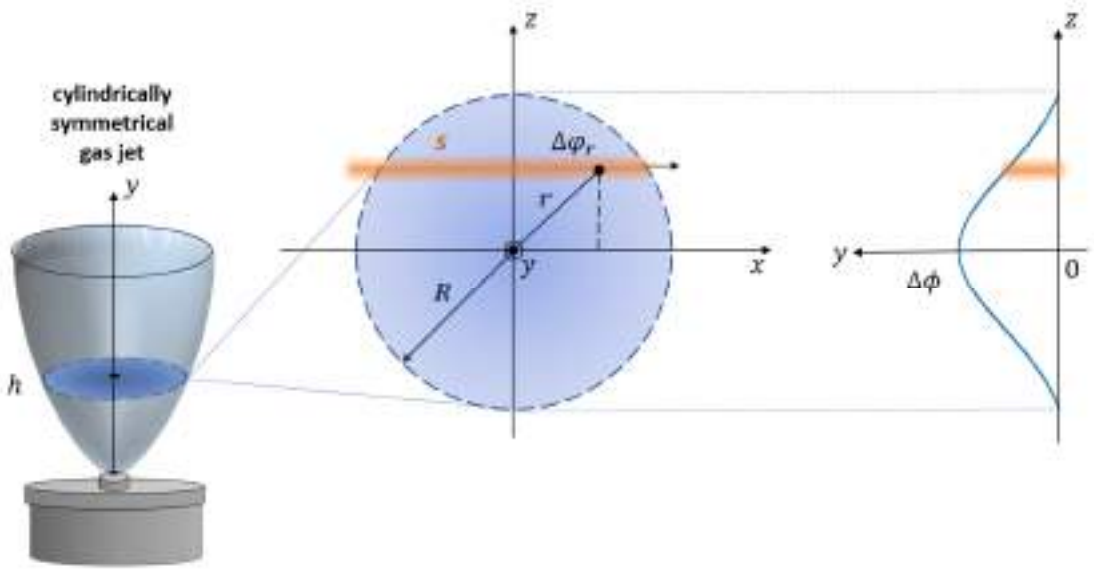

Figure 6.1 – Illustrative scheme of the Abel inversion method with a cylindrically symmetric gas jet: The gas jet integrated phase shift $\Delta\phi$ imprinted in the probe beam is used to recover the radial phase $\Delta\varphi_r$ height h and radius R.

Source: By the author.

From the radial phase map obtained using equation (6.6) and assuming an ideal background vacuum with refractive index equal to 1, the gas jet radial refractive index η can be obtained by:

$$\eta = 1 + \frac{\Delta\varphi_r \, \lambda_{pr}}{2\,\pi}, \tag{6.7}$$

where λ_{pr} is the probe wavelength that refers to the laser inspecting the gas jet or laser-induced plasma. Moreover, the molecular gas density distribution, n_g, can be evaluated from the jet refractive index using the Lorentz-Lorenz relation[209, 210]:

$$n_g = \frac{3}{4\,\pi\,\alpha}\left(\frac{\eta^2-1}{\eta^2+2}\right), \tag{6.8}$$

where α is the gas molecular polarizability. Figure 6.2 presents an illustrative scheme of the data processing steps contained in our homemade algorithms from the interferograms acquisition to gas jet density distribution.

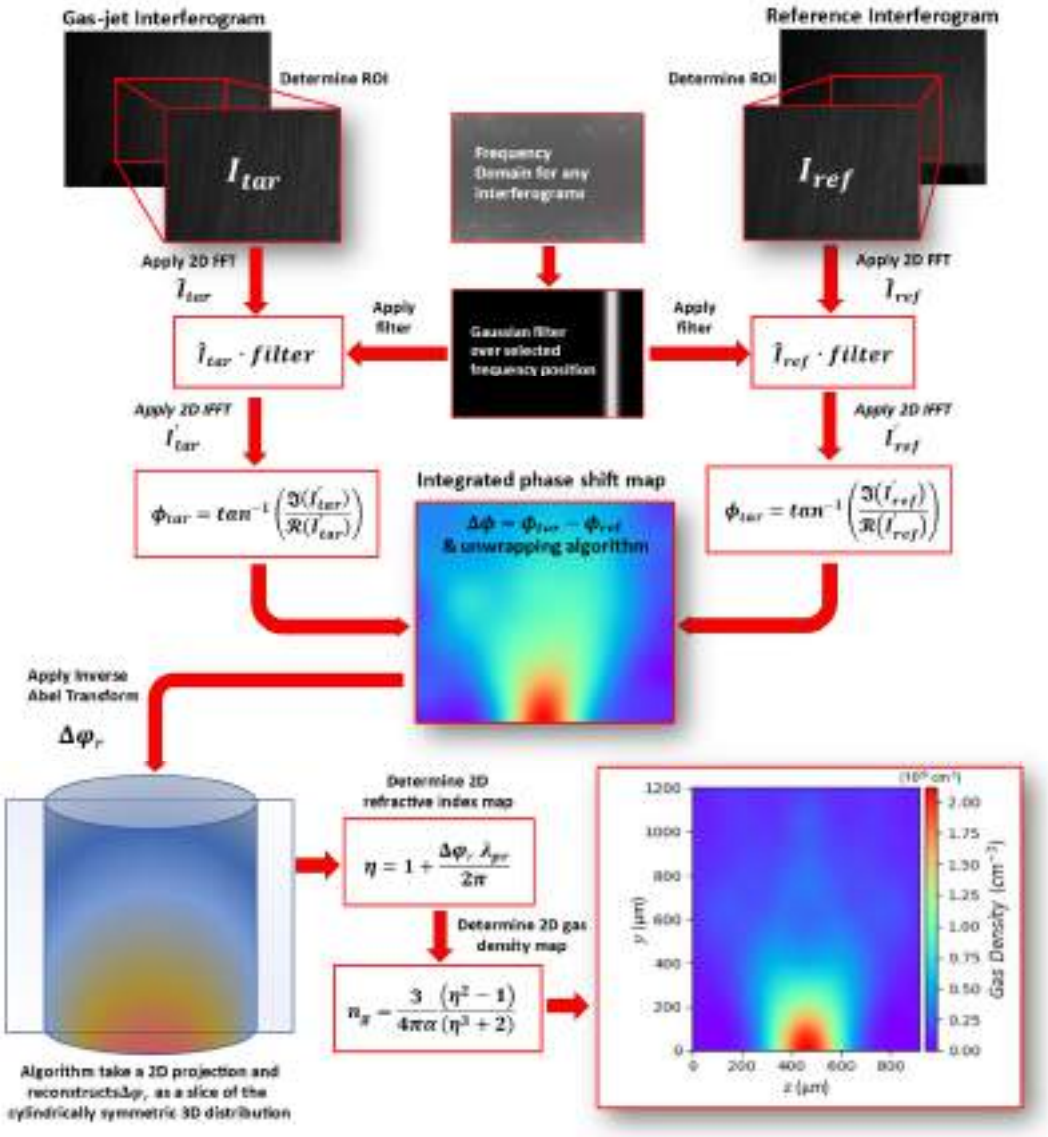

Figure 6.2 – Schematic interferogram analysis steps for determining gas jet radial density profiles.
Source: By the author.

To determine the density distributions of laser-induced plasmas from interferograms, procedures similar to those applied for the gas jets can be used, just changing the expression that relates the plasma density to its refractive index. Thus, the plasma electronic density, n_e, can be evaluated from its refractive index by[211]:

$$n_e = \frac{4\,\pi^2 c^2 \varepsilon_0 m_e}{e^2 \lambda_{pr}^2}\left(1 - \eta_p^2\right), \tag{6.9}$$

which is a derivation of the equation (2.43) where, η_p is the plasma refractive index obtained from equation (6.7). This simple model assumes that there is no variation of n_e across the plasma diameter due to differences in the local number of ionizations.

In our group, the first algorithms for interferogram analysis were implemented using the Wolfram Language in the Mathematica Software (Wolfram Research). Recently, the interferogram analysis was greatly improved by our group by creating a dedicated code in Python, using its scientific libraries, such as the Abel inversion method[212] present in the PyAbel package[213]. As a result, a homemade software to retrieve the density profile of gas jets, with a graphical user interface (GUI), named INTERFEROGRAM ANALYSIS GASJET, was made available in the Zenodo platform[214] as an installable software. Similarly, another homemade GUI software was developed to retrieve the density profile of laser-induced plasmas, named INTERFEROGRAM ANALYSIS LIP, also made available in the Zenodo platform[215]. All the results presented here were obtained with these softwares, except where noted.

Concerning the uncertainties of the retrieved density profiles from either gas jets or laser-induced plasmas, the homemade software has algorithms for their evaluation. The first error source comes from small differences between the target and reference interferograms, which can be described by the probability distributions of the intensities and phase derivatives of two intensity fringes patterns[216]:

$$\sigma_{\Delta\phi} = \frac{\pi\delta}{2\beta}\left[\frac{\langle I_{tar}\rangle\left(I_{tar}+I_{ref}\right)}{2I_{tar}I_{ref}}\right]^{1/2}, \tag{6.10}$$

where δ is related to the displacement between the 2D interferogram (target and reference), β is the fringe wavelength, and $\langle I_{tar}\rangle$ and $\langle I_{ref}\rangle$ are the fringes average intensity distribution in the target and reference interferograms. Both δ and β values are extracted from each line (y coordinate) of the interferogram by appropriate algorithms.

The second error source is related to the accuracy of applying the inverse Abel transform that depends on the symmetry degree of the integrated phase shift map. This

uncertainty can be determined for the i^{th} line of the phase map from the correlation between the radial phase, $[\Delta\varphi_r]_i$, and the normalized integrated phase, $\|\Delta\phi\|_i$, according to[217]:

$$(\sigma_{abel})_i = \Re(\|\Delta\phi\|_i - [\Delta\varphi_r]_i) = \sqrt{(\|\Delta\phi\|_i - [\Delta\varphi_r]_i)^2}, \tag{6.11}$$

where the index i represents the line position on the symmetrical axis of 2D $\Delta\phi$ and $\Delta\varphi_r$ maps, as illustrated in different lines in Figure 6.3.

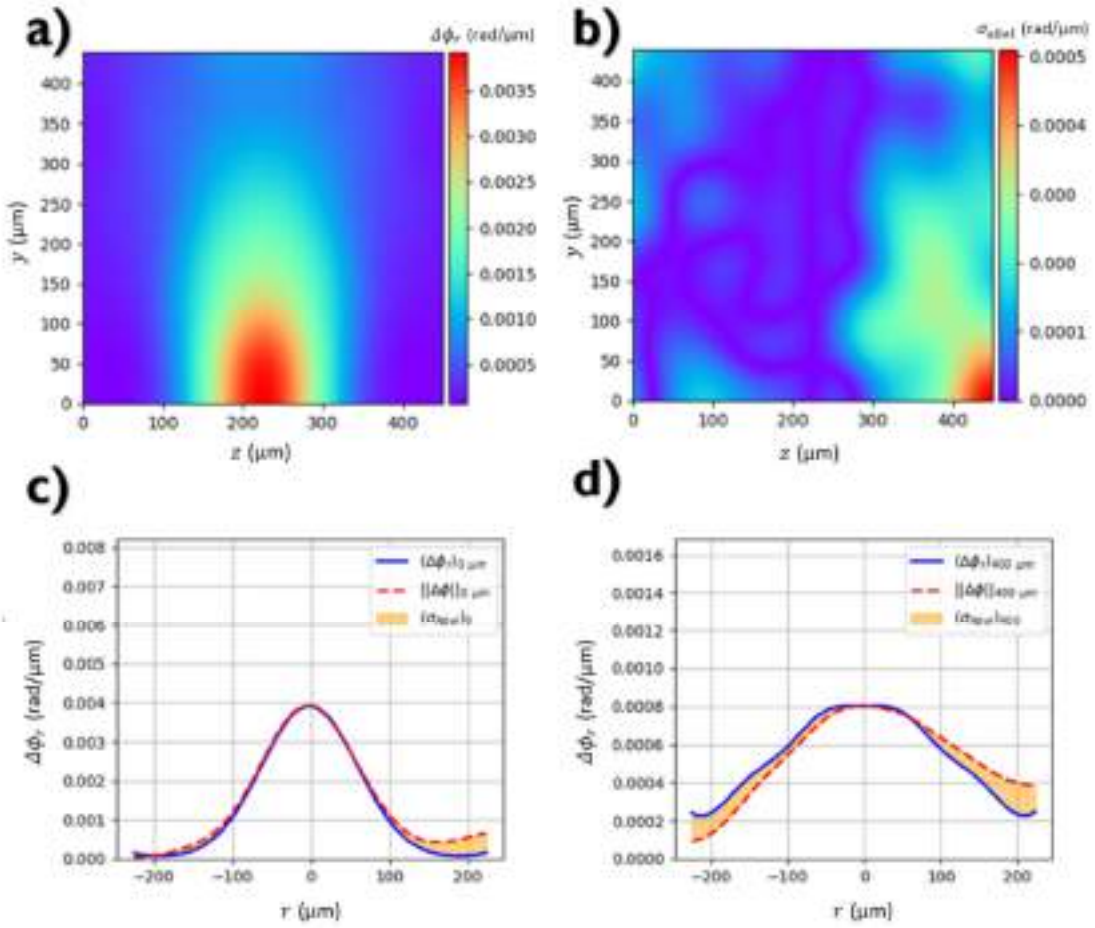

Figure 6.3 – Example of the determination of the σ_{abel}: (a) typical 2D $\Delta\varphi_r$ map of a gas jet, (b) the 2D σ_{abel} map determined from the correlation between $\Delta\varphi_r$ and $\|\Delta\phi\|$ for the lines extracted from (a), as exemplified by the two lines in the positions (c) y = 0, and (d) y = 400 µm. Similar processes are used for laser-induced plasmas analysis.

Source: By the author.

The last error source is related to the probe beam Gaussian bandwidth, being its standard deviation:

$$\sigma_{\lambda_{\text{pr}}} \approx 0.42\,\Delta\lambda_{\text{pr}}, \tag{6.12}$$

where $\Delta\lambda_{pr}$ is the probe bandwidth (FWHM). Using CW laser beams as a probe, the $\sigma_{\lambda_{pr}}$ value can be neglected since those lasers have a typical bandwidth under 0.01 nm. However, when probing with ultrashort laser pulses, the $\sigma_{\lambda_{pr}}$ contribution becomes crucial once they have large bandwidths, as shown in Section 6.3. Each of the three error sources are taken into account in our homemade algorithms, being their contribution to the gas jet density maps provided through the error propagation in each step of the data processing. Determining the relative weights of each source of uncertainty in the final result is not an easy task, and this analysis is being done in a manuscript in preparation for publication[218].

6.2 Implementation of a CW Mach-Zehnder interferometer to measure gas jets

To characterize typical LWFA targets such as gas jets and plasmas the Mach–Zehnder and Nomarski interferometers are largely employed, each with different advantages depending on their application. For our purposes, the MZI offers the following advantages over the Nomarski interferometer[125]: (1) greater control over the spacing and orientation of the interferogram fringes, once the wavefront of each arm can be individually controlled, (2) better control over the interferogram resolution since it depends only on the imaging system (distances of lenses and/or mirrors before the imaging detector), while for Nomarski interferometers the resolution can be also limited by the aperture of the Wollaston prism. Therefore, our group decided to implement a MZI that was assembled with different configurations according to the evolution of the PhD, as discussed in this Chapter.

An initial MZI configuration arose from the need to diagnose gas jets generated by the first micrometric nozzles manufactured, therefore a typical Mach-Zehnder interferometer[93, 119] was built in atmosphere using a CW linearly polarized green helium-neon (HeNe) laser with λ_{pr} = 543 nm and $\Delta\lambda_{pr}$ = 0.002 nm bandwidth. As outlined in Figure 6.4a, the HeNe beam is spatially filtered using a 50 μm pinhole and collimated into a 1 cm radius beam; this beam is split by the beamsplitter BS1 into REF and DIAG beams, being the latter the arm that propagates through the gas jet generated by the nozzle. The interferogram of the phase accumulated by the DIAG beam is obtained by overlapping it with the undisturbed REF beam after recombination in the second

beamsplitter, BS2. A 10 cm convergent lens (L), positioned after the BS2 and 12 cm away from the gas jet, produces a 5× magnified interferogram of the gas jet in the surface of a CCD. The CCD integration time was 10 ms. This configuration allows the characterization of a continuous flow gas jet, with the nozzle connected directly to a ¼" diameter copper tube, as presented in Figure 5.5a. In addition to operating as an interferometer[162], the MZI design can be also employed to produce shadowgrams using the Schlieren imaging technique [91, 219, 220], generating a gas jet image directly on the CCD. This method is implemented by blocking the REF beam and inserting a knife-edge (KE) at the focal point of the lens L, as shown in Figure 6.4b, working as an auxiliary technique to interferometry to diagnose the geometrical profile of the gas jet. A photo of the MZI setup is shown in Figure 6.4c.

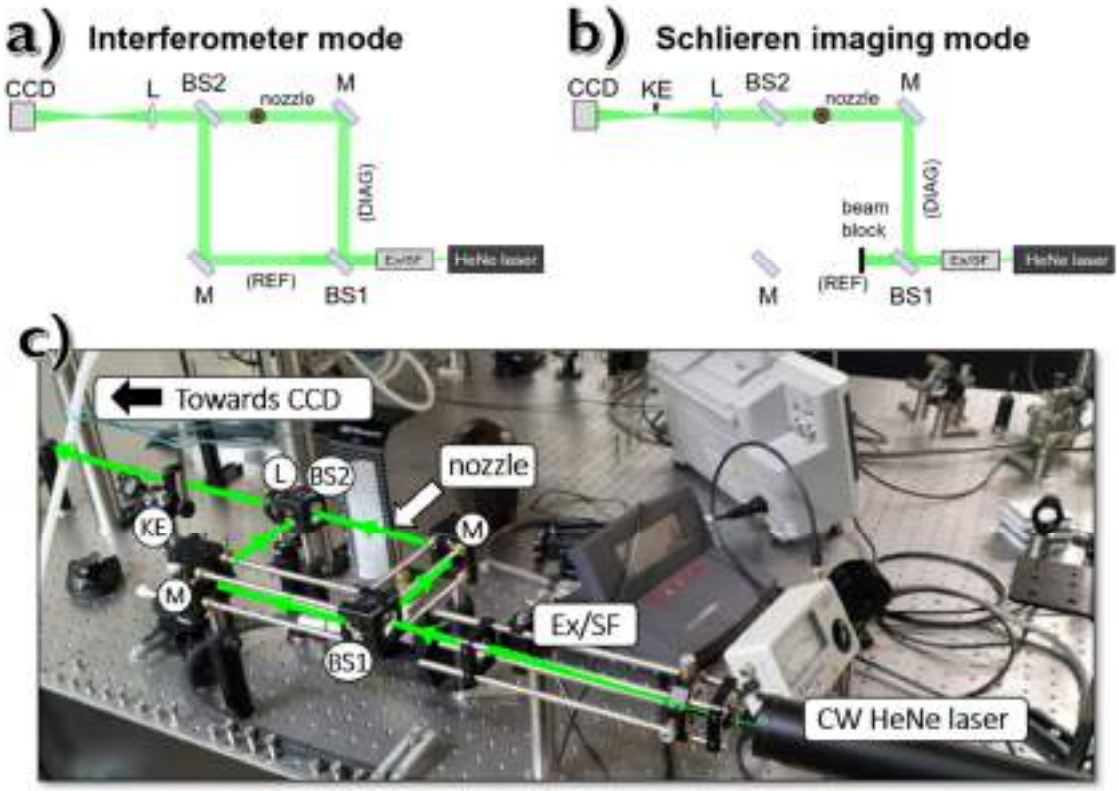

Figure 6.4 – Schematic of the CW MZI setup to diagnose gas jets generated by the manufactured nozzles: (a) interferometer mode (b) Schlieren imaging mode. (c) A photo of the setup in atmosphere. Ex/SF: expander/spatial filter, BS: beam splitter, M: mirror, L: lens, KE: knife-edge, and CCD: charge-coupled device.

Source: By the author.

Since the desired environment to diagnose the gas jet is vacuum, a small vacuum chamber was created to be inserted in the DIAG arm. As illustrated in Figure 6.5, this

chamber is fitted to the ¼" diameter copper tube by a flange with an o´ring, keeping the nozzle inside, and has a connection to a mechanical pump on its top. This chamber was used to study the nozzle performance in a vacuum environment (~50 mbar) when applying a backing pressure of up to 50 bar.

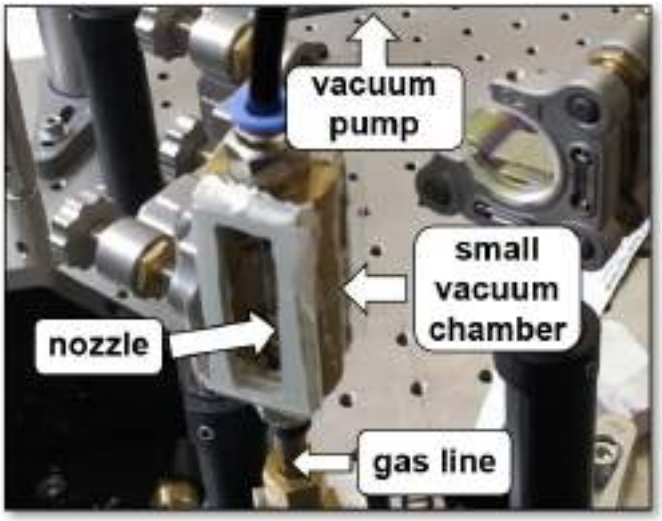

Figure 6.5 – Small vacuum chamber fitting the ¼" diameter copper tube. The gas jet flows continuously with backing pressure up to 50 bar while a mechanical vacuum pump establishes a background pressure of about 50 mbar inside the vacuum chamber.

Source: By the author.

Each of the two techniques (interferometry and Schlieren) produces different 2D images, which are captured by the CCD. As exemplified in Figure 6.6a, wavefront distortions induced by the jet refractive index profile, which deviate from the DIAG beam, are directly visualized in the shadowgram, yielding a clear image of the jet expansion that is suitable for characterizing its geometric profile. When these wavefront distortions are compared (interfered) with the REF beam, the accumulated phase causes a bending of the interferogram fringes (Figure 6.6b), which does not present a clear visualization of the jet profile. The density profile of the jet is retrieved using the methods and software described in Section 6.1.

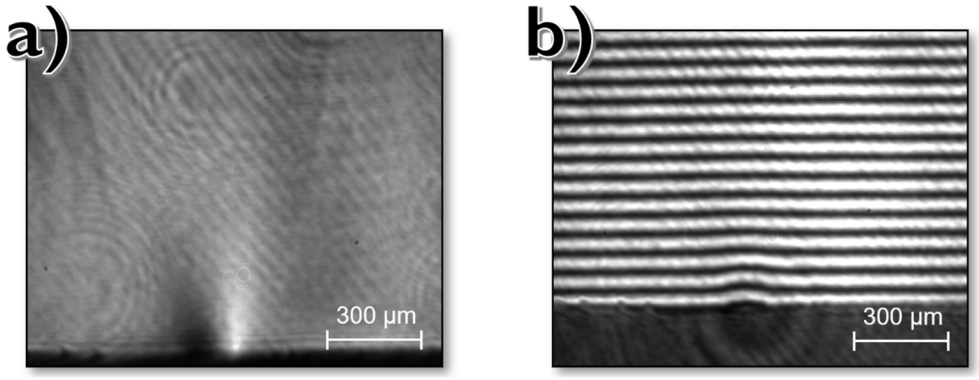

Figure 6.6 – Example of (a) a Schlieren imaging and (b) interferogram under the same experimental conditions: N_2 jet expanding at a backing pressure of 50 bar inside of the small vacuum chamber (~50 mbar). The jet was generated by a manufactured nozzle with $\emptyset_e$ = 190 µm and $\emptyset_t$ = 85 µm.
Source: By the author.

6.2.1 Characterization of gas jets

A typical gas jet characterization using the CW Mach-Zehnder interferometer and our homemade software is presented in Figure 6.7, where a nitrogen gas jet created from a manufactured nozzle with $\emptyset_e$ = 190 µm and $\emptyset_t$ = 85 µm and a backing pressure of 50 bar, was measured in the atmosphere and in a background of ~50 mbar (inside the small vacuum chamber). The shadowgram in vacuum is the same shown in Figure 6.6a, and the density map in vacuum comes from the interferogram presented in Figure 6.6b. Shadowgrams are shown in part (a) of Figure 6.7, and the gas density maps obtained using α = 1.710 Å^3 for N_2[221] are shown in the part (b). From these maps, the density profiles close to the nozzle exit ($y \approx 0$ µm) were extracted shown in Figure 6.7c, with their uncertainties σ_{n_g} obtained directly from the software[214].

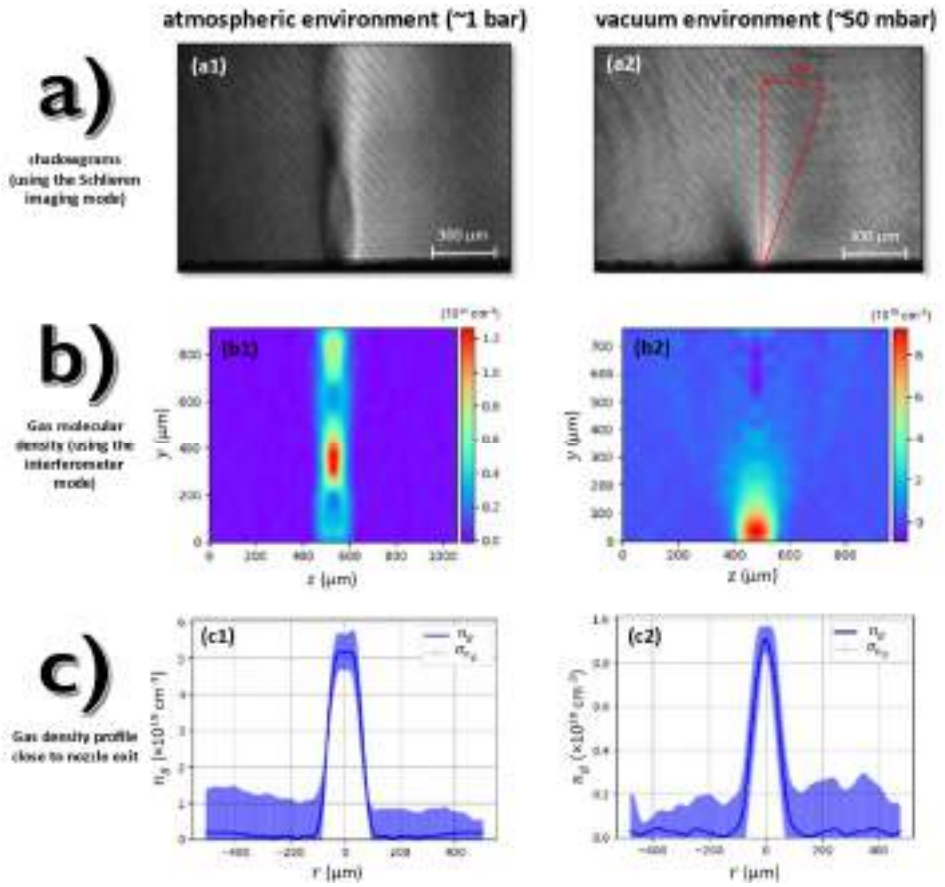

Figure 6.7 – Nitrogen jets expanding in (1) atmosphere and (2) vacuum from a typical micrometric manufactured nozzle. Measurements performed by the CW Mach-Zehnder interferometer in the (a) Schlieren imaging mode, and (b) interferometer mode; part (c) shows the density profiles close to the nozzle exit extracted from the maps in (b).

Source: By the author.

Regarding the results displayed in Figure 6.7, despite the noise in the 2D density maps, the jet shape can be clearly observed from the interferometer mode, in addition to the Schlieren images. Therefore, one of the first conclusions was that Schlieren imaging can be an optional and complementary technique, to quickly visualize the approximate shape of the jets, but it is not essential to diagnose the target geometries since interferometry has already been implemented. As discussed in the next sections, the Schlieren imaging technique was not used for other measurements. In addition, our first results indicated the adequacy of the interferometry technique and the algorithms employed to diagnose the gas jets produced by our manufactured nozzles, measuring their geometry and density distribution with micrometric sensitivity. For the jet in atmosphere, its geometry is characteristic of a supersonic expansion with the formation of shock regions shaped like diamonds (regions with the highest density)[222, 223], being the first indication of the formation of supersonic jets from our nozzles. On the other hand, the

characterization of the jet expansion in vacuum is more relevant since this is the environment for laser-plasma interactions, being described by the equations of the quasi-1D model (discussed in Chapter 5) as a reference to compare with the measured density maps. Regarding the gas jet Mach number, the theoretical value calculated from the nozzle exit and throat areas by equation (5.1) is M ≈ 3.3 for nitrogen (κ = 1.47). However, a divergence angle $\theta_g \approx 19°$ was measured from the Schlieren imaging, yielding M ≈ 3.0 from equation (5.3), a Mach number slight smaller than the theoretical one. This discrepancy could be associated to the nozzle convex trumpet shape as discussed in Figure 5.8, which in second approximation reduces the jet Mach number[199]. Nevertheless, both values are close enough to consider the Mach number given by equation (5.1) as a good reference for designing nozzles. Concerning the measured density profile inside the small vacuum chamber, the highest gas molecular density is $(9.0\pm1.1)\times10^{19}$ cm^{-3} close to the nozzle exit, and it drops abruptly with distance due to the gas expansion in vacuum. This measured value is about twice the estimated value of 4.0×10^{19} cm^{-3} using equation (5.2) and the estimated M=3.3 from equation (5.1). Although this discrepancy exists, probably arising from the aspects not considered in the quasi-1D model, the density values are in the same order of magnitude. In addition, as discussed in Section 5.3, the nozzle convex trumpet shape decreases the Mach number[199], increasing the gas density close to the nozzle exit. This indicates that the discrepancy should come from the idealization implicit in the quasi-1D model that does not take into account the nozzle shape. The quasi-1D model expressed by equations (5.1) and (5.2) also does not apply perfectly to realistic 3D gas jet flows, and CFD simulations can provide more accurate descriptions. Analysis performed by our group[117] for a similar nozzle ($\emptyset_e$ = 190 µm and $\emptyset_t$ = 85 µm) returned a density close to the nozzle exit of about 1.5×10^{20} cm^{-3}, which is 2 times higher than the measured value, and 4 times higher than the theoretical prediction by the quasi-1D model. Lastly, the inappropriate background pressure inside the small vacuum chamber (~50 mbar) should be another source for this discrepancy since an adequate vacuum environment should be smaller than 10^{-3} mbar. Despite the discrepancies, the measured value is between the two theoretical predictions, validating the efficiency of the interferometry technique as well as the algorithms employed in our codes. It is noteworthy that although only one result was shown in this section as an illustrative example, several other gas jets produced from different manufactured nozzles also were characterized by CW Mach-Zehnder interferometer and they obtained conclusions similar to those discussed here.

Within our purposes, the next step is diagnosing the laser-induced plasma, as discussed in the next section.

6.3 Development of time-resolved MZI in atmosphere

Interferometry measurements for laser-induced plasmas require a higher spatial resolution than used with gaseous targets, due to the plasma smaller dimensions, and, more important, pump-probe techniques due to the plasma fast decay time[95], which would fade out in CW measurements due to the extremely small duty cycle. The use of femtosecond pump-probe techniques allows a time scanning during the plasma formation, which allow the investigation of the plasma dynamics, potentially being able to study the wakefield establishment and electron acceleration processes. Therefore, we developed and built a novel kind of time-resolved Mach-Zehnder interferometer[118] as presented below.

The new Mach–Zehnder-like interferometer is coupled to a pump-probe setup, and was developed to characterize transient phenomena in gaseous targets and laser-induced plasmas. Although this interferometer is intended to operate in vacuum, where the laser-electron acceleration will occur, it was initially built in atmosphere for a preliminary characterization of the device, as shown in Figure 6.8. This setup uses Femtopower pulses (τ_L = 25 fs, λ_{CM} = 780 nm, $\Delta\lambda_L$ = 40 nm, $\mathcal{E}_L \leq$ 650 µJ, ≤ 4 kHz, and $M^2 \approx 1.2$), and, initially a beam sampler (BSa) extracts a fraction of the pulse energy, which is sent through a delay line (delay 1) and focused in a BBO crystal to generate second harmonic pulses at 392 nm. The second harmonic pulses duration can be estimated by the duration of a Gaussian pulse broadened due to the group velocity dispersion (GVD), given by[125, 224]:

$$\tau_2 = \tau_1 \sqrt{1 + \left(4\, ln2\, \frac{D_{GVD}\, L}{\tau_1^2}\right)^2}, \tag{6.13}$$

where τ_1 and τ_2 are the pulse duration of the laser pulse before and after the BBO crystal, L is the propagation length in the crystal, and D_{GVD} is the dispersion parameter of the medium. Using L = 0.3 mm, D_{GVD} = 196 fs²/mm for the dispersion parameter of BBO for 392 nm[125], and assuming second harmonic pulses with initial duration equal to the fundamental pulse, $\tau_1 = \tau_L$ = 25 fs, equation (6.13) yields τ_2 = 25.8 fs ≈ τ_L. The second harmonic pulses are used as a probe due to intrinsic advantages when compared to the

fundamental wavelength: they offer double spatial phase resolution, can measure higher density plasmas due to the higher plasma frequency, and can be isolated from laser scatterings by the use of optical filters.

After the BBO crystal, the probe pulses are collimated into a ~5 mm diameter beam that enters the MZI to diagnose the gas jets or side-view of the plasma formed by the high-energy pulses (pump), which are focused by a 90°, 50 mm, off-axis parabolic mirror (OAP).

The temporal delay between pump and probe pulses is controlled by a micrometric positioning system (Newport UTS100C) with a range of 200 mm and a minimum step of 1 µm, which corresponds to a double pass minimum delay of 6.6 fs. However, the temporal resolution of the technique is limited by the duration of the probe pulses.

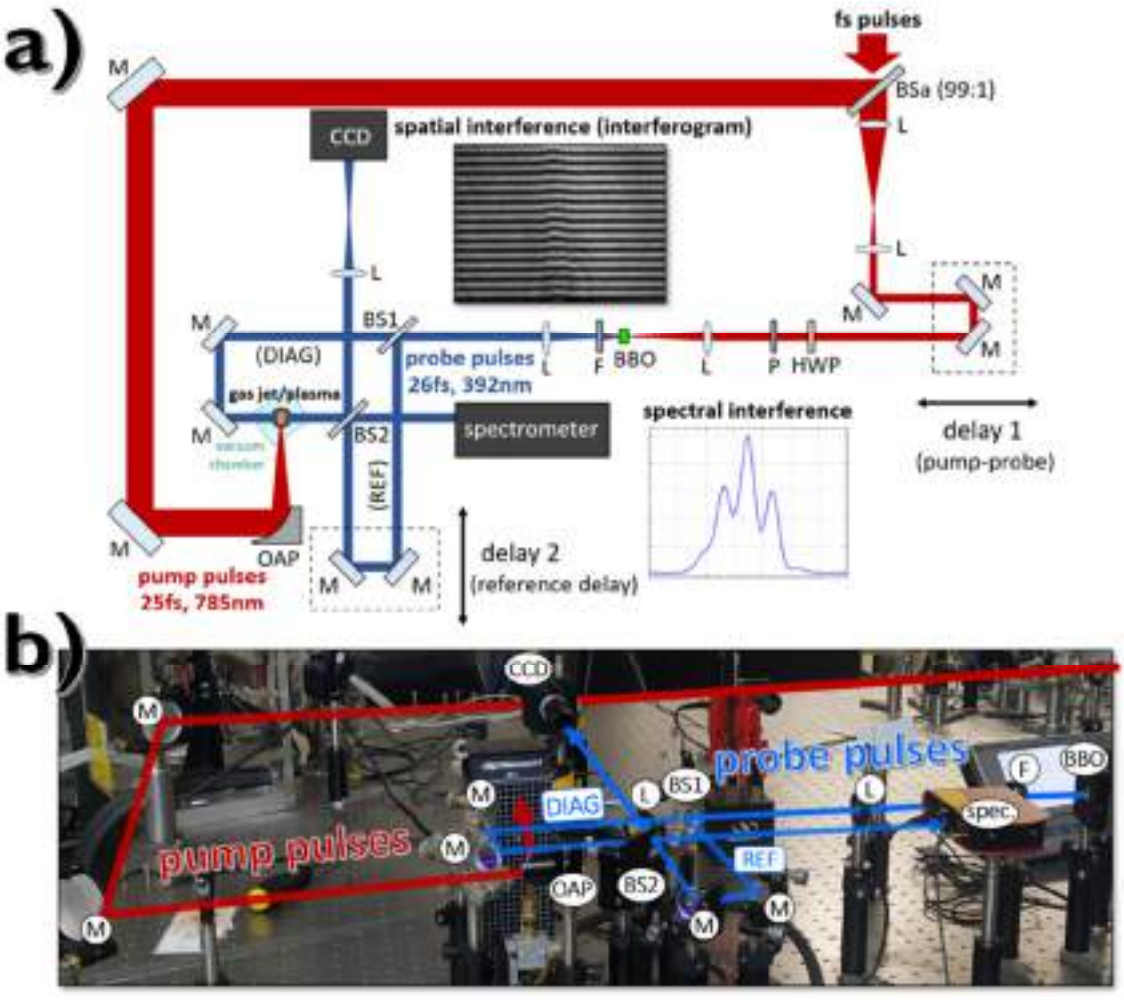

Figure 6.8 – (a) schematic pump-probe setup containing the Mach-Zehnder-like interferometer. M: mirror, L: lens, F: filter, P: polarizer, BS: beamsplitter, BSa: beam sampler, OAP: off-axis parabolic mirror, HWP: half-wave plate, BBO: beta barium borate crystal, CCD: charge-coupled device, and spec.: spectrometer. (b) A photo of the setup assembled in atmosphere.

Source: By the author.

In the interferometer, the probe pulses are divided by a beamsplitter (BS1) into reference (REF) and diagnostic (DIAG) beams; the DIAG beam propagates through the target (gas jet or plasma), accumulating a phase that is retrieved by interference with the REF pulses, after recombination in the BS2 beamsplitter. The temporal overlap between REF and DIAG pulses is obtained by adjusting the REF arm delay (delay 2) by a translation stage supporting 2 mirrors in a roof configuration. After the BS2, the recombined pulses propagate through a 150 mm convergent lens that produces a three-fold magnified interferogram (spatial interference) of the target at the CCD, from which the gas jet or side-view plasma density can be retrieved. BS2 also directs other recombined beams to a spectrometer, creating a spectral fringe pattern (spectral interference). This spectral interference pattern is easier to find than the spatial one when adjusting the delay 2, and it is used to set the two arms with the same optical length; once this “zero-delay” position is found, the interferogram is seen on the CCD. The interferometer also allows small adjustments in the REF arm mirrors to define the fringes spatial frequency and direction. Lastly, as this setup was built in the atmosphere for initial tests, we decided to maintain a continuously gas flow through the ¼" diameter copper tube, which can be fitted by the small vacuum chamber for gas jets studies in vacuum. On the other hand, the plasma measurements could only be made in the atmosphere, since the small vacuum chamber has only one pair of windows which does not allow the insertion of orthogonal beams, as is the case of the pump beam and the DIAG arm, as can be seen in Figure 6.8. It is worth mentioning that in all measurements using the time-resolved MZI in atmosphere, the CCD integration time was 10 ms, as in the CW measurements. Therefore, each recorded interferogram is composed of a superposition of 40 laser shots once the Femtopower was operating at 4 kHz.

The relevance of using a spectral interference pattern (fringes) becomes clear when comparing the pulses spatial and spectral coherence lengths. To estimate the spatial coherence length of the MZI, the contrast of the spatial interferogram fringes was plotted as a function of small displacements around the “zero-delay” position. Figure 6.9a presents a set of those interferograms, with the displacements from the “zero-delay” position indicated, and Figure 6.9b shows the fringes contrast dependence on this displacement, and it can be clearly seen that for displacements above ~15 µm the fringes disappear. The FWHM of the fitted Gaussian function, 14.3 µm, was taken as the MZI spatial coherence length. In practice, finding the “zero-delay” position requires adjusting

delay 2 within a few tens of µm of it, and a few µm are required to optimize the fringes contrast. We observe that it is very difficult to find these interference patterns experimentally.

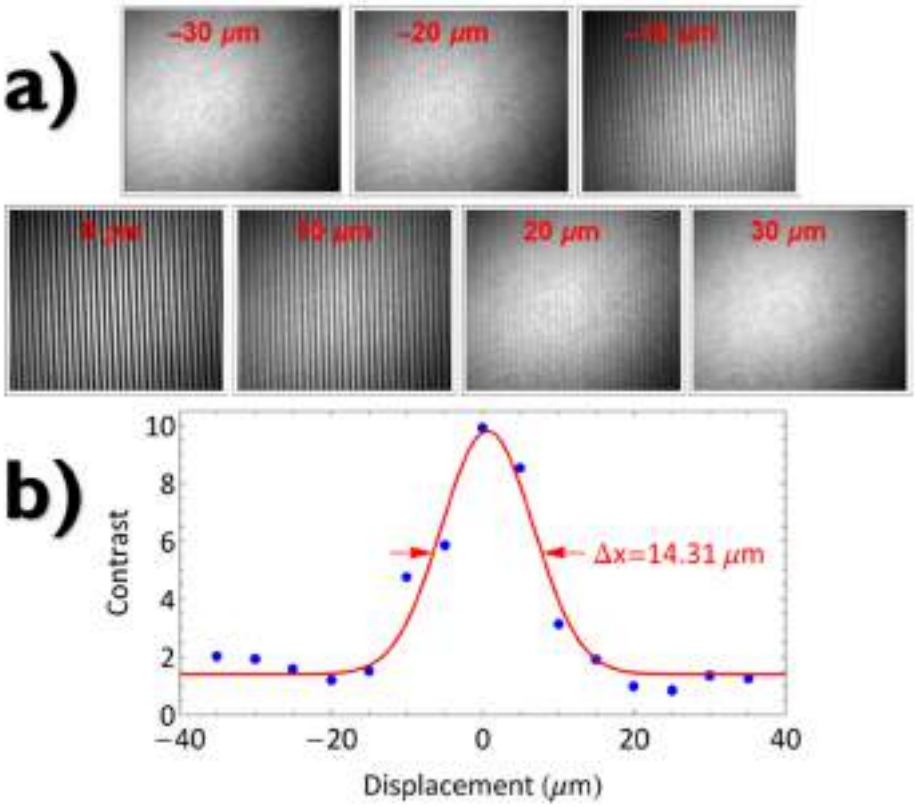

Figure 6.9 – Spatial-domain coherence length determination. (a) interferograms measured for different displacements around the "zero-delay" position. (b) fringes contrast dependence on the displacement measured from a common line of the interferograms and fitted Gaussian.

Source: By the author.

Regarding the spectral coherence length, Figure 6.10 presents the MZI spectral interference as a function of the displacement around the "zero-delay" position (indicated in each spectrum). These spectra plainly show that the spectral coherence length is over 200 µm, more than an order of magnitude longer than the spatial one. This happens because the spectral interference occurs even before the pulses overlap temporally[225, 226] since the pulse replicas, which are apart by a time Δt in the time-domain prints a spectral fringe with the period of $1/\Delta t$ over the pulse spectra in the frequency-domain. Using this concept, we have enhanced the handling of the setup, making it easier to find the "zero-delay" position for the REF arm to measure the interferograms at the CCD[123].

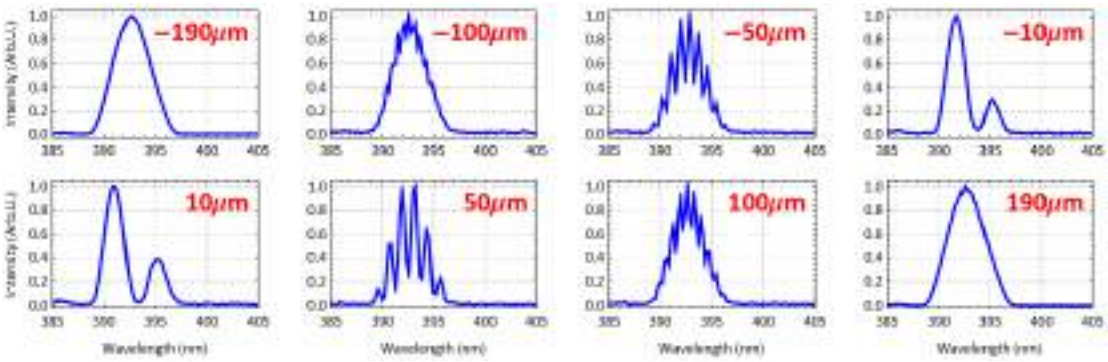

Figure 6.10 – Spectral-domain coherence length performed from the spectra measured with different values of delay 2. The spectral interference pattern appears for delay times by an order of magnitude greater than for spatial interference.

Source: By the author.

Another important feature of our pump-probe setup is the laser intensity achieved by the pump pulses focused to the target by the OAP. In order to estimate this intensity, a pilot focusing experiment was performed using pump pulses with 25 fs, 350 μJ, and $M^2 \approx 1.2$, whose beamwaist was ten-fold magnified by a f = 50 mm achromatic doublet to be measured on a CCD once its pixels have 6.7 × 6.7 μm^2. This experiment setup and the focused laser Gaussian intensity profile obtained are shown in Figure 6.11. Both x and y cross-sections have a beamwaist of about 4 μm, defining a laser intensity of ~2.1×10^{16} W/cm^2[119].

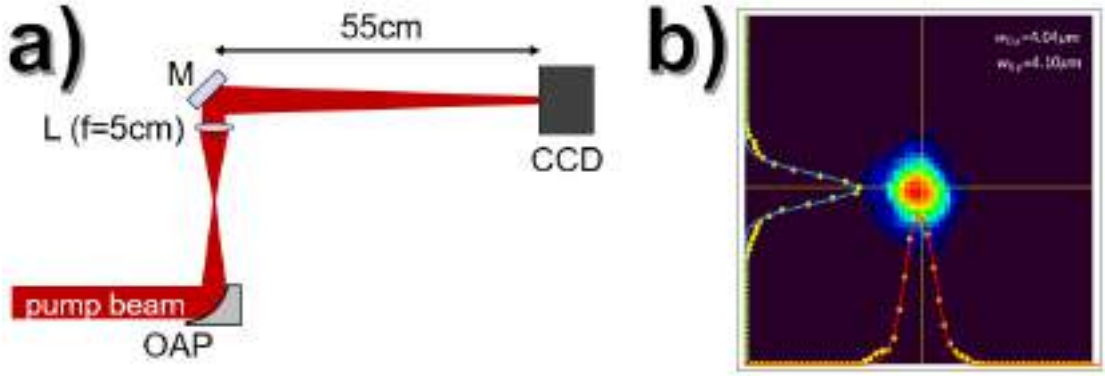

Figure 6.11 – (a) schematic setup for measuring the pump beamwaist 10× magnified: M: mirror, L: lens, CCD: charge-coupled device, and OAP: off-axis parabolic mirror. (b) CCD image of the magnified laser focus with beamwaist on the x-axis and y-axis is about 4 μm.

Source: Adapted from SAMAD, R. E., *et al*[119].

6.3.1 Characterization of gas jets

The interferogram results using the time-resolved Mach-Zehnder-like interferometer in atmosphere involving gas jets are discussed in this section, while laser-induced plasmas are presented in Section 6.3.2.

The interferogram analysis explored in Figure 6.12 shows a nitrogen gas jet expansion inside the small vacuum chamber from a backing pressure of 50 bar. This gas jet was generated from the same nozzle ($\emptyset_e$ = 190 µm and $\emptyset_t$ = 85 µm) measured by the CW MZI (Figure 6.7), and under the same experimental conditions and interferogram analysis algorithms. Thus, Figure 6.12a exhibits the interferogram of the gas jet, which is evidenced by the fringes bending. This interferogram can be compared to the CW MZI measurement in Figure 6.6b, which has a worse spatial resolution since the image is more blurred. The better spatial resolution in Figure 6.12a comes from a higher spatial frequency of the fringes, a consequence of the shorter wavelength provided by the second harmonic pulses at 392 nm, when compared to the green laser at 543 nm. The higher fringe density enhances the interferogram analysis, which can be identified when comparing the retrieved gas density maps in Figure 6.12b with the one in Figure 6.7b2, both resulting from the same nozzle and backing pressure. This last map contains computational artifacts related to the Abel inversion process for greater heights above the nozzle exit, which are absent in Figure 6.12b. Concerning the measured gas densities, Figure 6.12c presents the density profile close to the nozzle exit with a peak density of $(1.1\pm0.3)\times10^{20}$ cm^{-3} that is approximately 20% higher than the similar measurement from Figure 6.7bc, although both measurements are covered by the error bars. This measured peak density is also close to the two theoretical predictions discussed in Section 6.2.1, 4.0×10^{19} cm^{-3} using the quasi-1D model, and 1.5×10^{20} cm^{-3} from CFD simulations. The proximity of the density values proved the good agreement of the time-resolved MZI for gas density measurements with an improvement over the CW MZI, which ensures our confidence in the setup and methodology used. Finally, Figure 6.12d exhibits the density profile for 4 heights above the nozzle exit (y = 0, 150, 300, and 450 µm), showing the abrupt density drop with the height increase, as well as the loss of the flat-top jet shape in vacuum. Thus, to conduct desirable plasma and wakefield conditions is recommended that the laser interaction occurs as close as the nozzle exit possible.

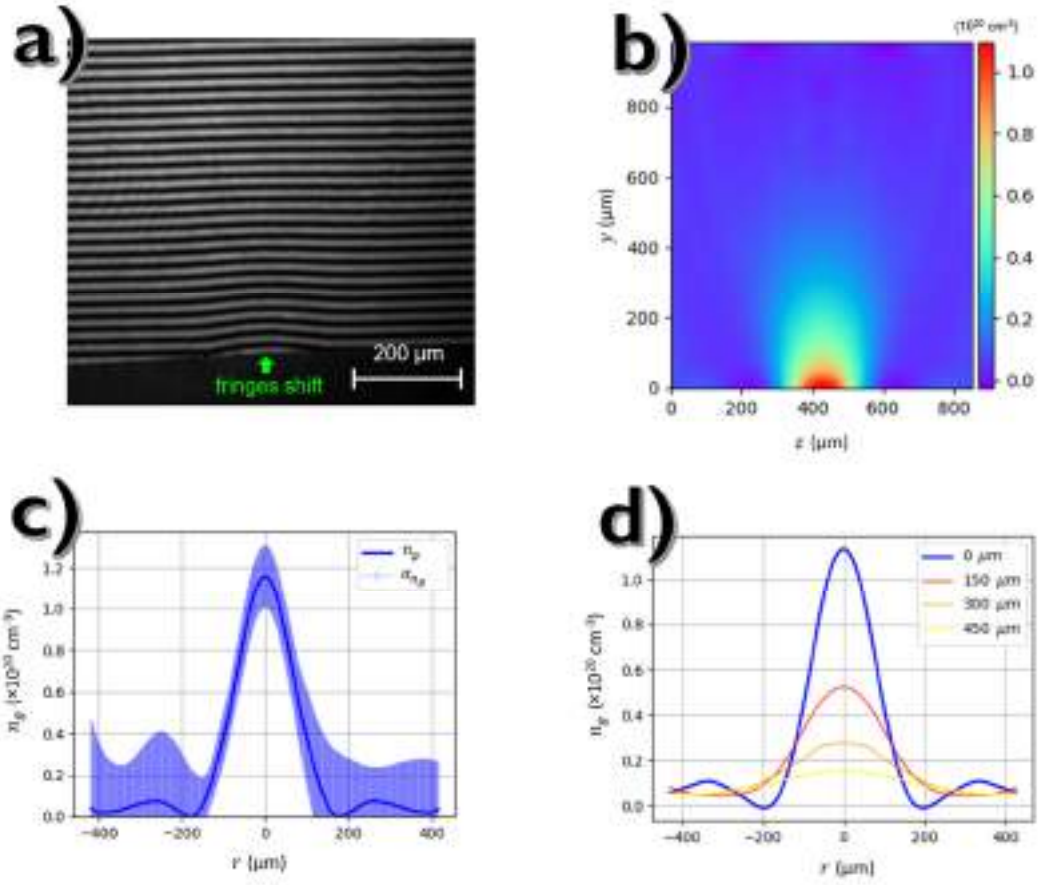

Figure 6.12 – Nitrogen jets expanding at a backing pressure of 50 bar inside the small vacuum chamber (~50 mbar) from the nozzle manufactured with $\emptyset_e$ = 190 µm and $\emptyset_t$ = 85 µm. (a) interferogram. (b) gas density map, (c) density profile close to the nozzle exit (y = 0 µm) with uncertainties evaluated from the homemade software, and (d) density profiles for y = 0, 150, 300, and 450 µm above the nozzle exit, extracted from density map in (b).

Source: By the author.

An identical experiment to the previous one was carried out using a nozzle with smaller diameters, $\emptyset_e$ = 135 µm and $\emptyset_t$ = 45 µm, which are shown in Figure 5.6 profilometries. The results are exhibited in Figure 6.13, where the interferogram containing the N_2 jet expanding inside the small vacuum chamber from a backing pressure of 50 bar is barely visible in the fringes shift in Figure 6.13a. Once this nozzle diameters are smaller than the previous one ($\emptyset_e$ = 190 µm and $\emptyset_t$ = 85 µm), that results in a smaller gas flow and a thinner target, making the fringes bend less prominent than in Figure 6.12a. Concerning the jet density distribution exhibited in Figure 6.13b, the gas density profile close to the nozzle exit (y = 0 µm) presents a peak density of (4.0±0.5)×10^{19} cm^{-3}, as shown in Figure 6.13c. This value is more than 2 times higher than the estimated value of 1.6×10^{19} cm^{-3} using the quasi-1D model[177], repeating the trend observed in the

previous nozzle, which confers reproducibility to our methodology. Also, it is noteworthy that the density uncertainties (error bars) in Figure 6.13c presents a strong asymmetry around the radial axis. This imbalance comes from the Abel inversion algorithm, which assumes that the density distribution has cylindrical symmetry and searches for a revolution axis in the phase map; strong asymmetries in this map will be represented by uneven error bars in the final retrieved density. Figure 6.13d presents the gas density profiles for 4 heights above the nozzle exit (y = 0, 150, 300, and 450 µm), showing again an abrupt density drop with the height increase. Moreover, for the two largest distances, 300 and 450 µm, the profile shapes show unexpected behaviors that are probably due to computational artifacts related to the Abel inversion process. These artifacts are similar to the ones seen in Figure 6.7b2, but are less pronounced, which could be a consequence of the smaller phase shift induced by this nozzle when compared with the expansion from a higher flow nozzle. Nevertheless, the time-resolved MZI improved spatial resolution when compared to the CW MZI, could resolve low gas volume flows produced by smaller nozzles. Improvements in the imaging system, setup isolation to reduce mechanical instabilities and unwanted diffractions in the interferograms, and mainly working at a smaller background pressure environment should contribute to obtaining better gas jet contrast. Those are motivations for moving the setup to a better vacuum chamber, capable to achieve lower background pressures under 1 mbar.

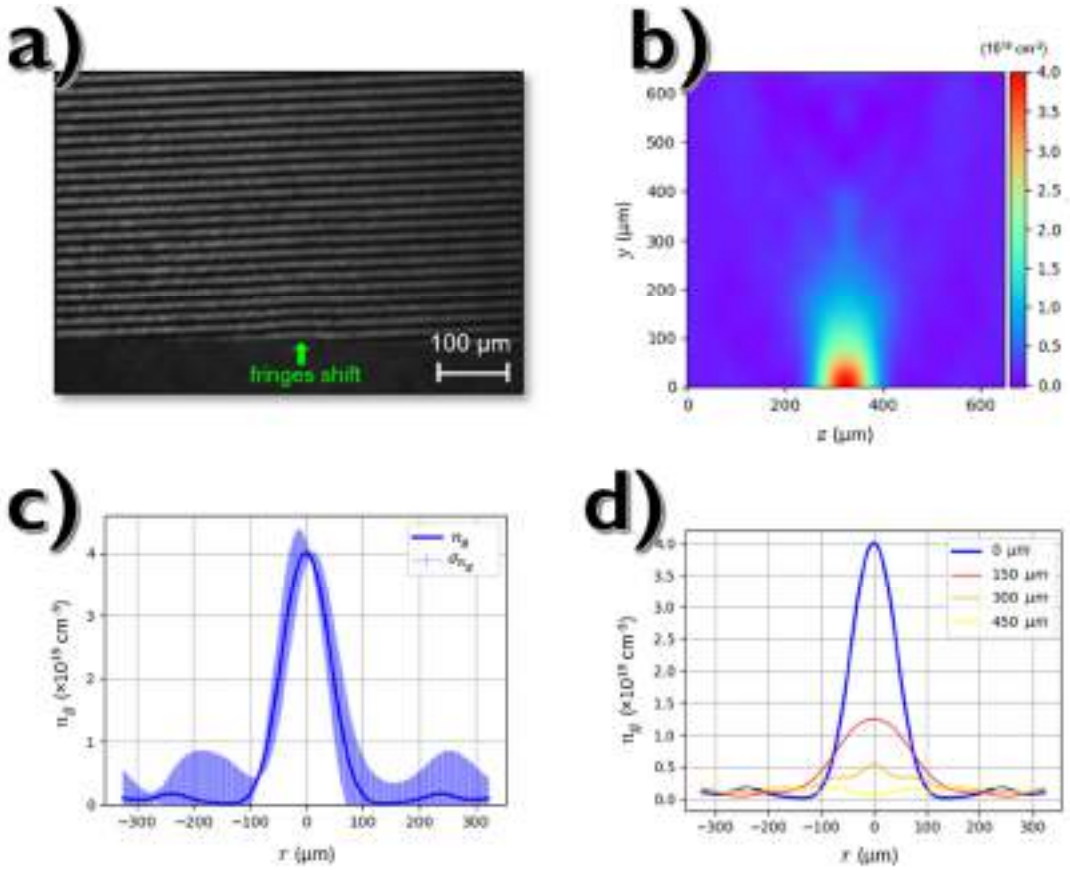

Figure 6.13 – N_2 jets from the $\emptyset_e$ = 135 µm and $\emptyset_t$ = 45 µm nozzle and 50 bar backing pressure inside the small vacuum chamber (~50 mbar). (a) interferogram. (b) gas density map, (c) density profile close to the nozzle exit (y = 0 µm), and (d) density profiles for 0, 150, 300, and 450 µm above the nozzle exit, extracted from density map in (b).

Source: By the author.

6.3.2 Characterization of laser-induced plasmas

The pump-probe interferometer was used for laser-induced plasma measurements in the atmosphere. Figure 6.14 shows the analysis of a typical laser-induced plasma in air. Part (a) shows the plasma side-view interferogram, part (b) presents the density map retrieved from it, and part (c) presents the plasma transversal profile at its maximum peak value. This laser-induced plasma was produced by focusing pump pulses with an energy of 200 µJ, duration of 25 fs, and $M^2 \approx 1.2$, to $w_0 \approx 4$ µm, reaching intensities above 10^{16} W/cm^2. Those laser parameters were used in the experiments discussed in this section, where plasma interferograms were measured at different time delays. In the interferogram, the plasma presence is evidenced by the fringes shift, as well as by a brightness increase due to its emission. In addition, the interferogram fringes were

adjusted to be perpendicular to the laser propagation direction, and with a spatial frequency sufficiently high to make the plasma shifted fringes clearly visible.

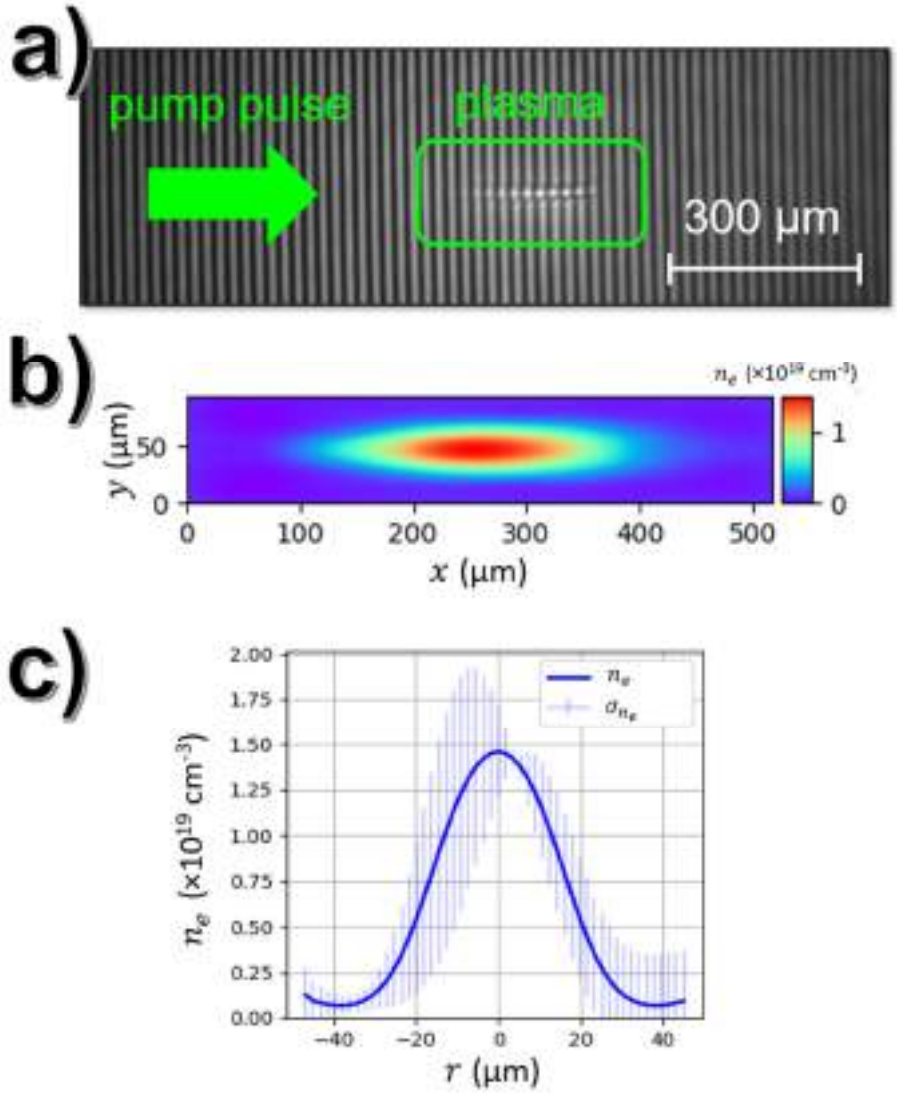

Figure 6.14 – (a) Side-view interferogram of a laser-induced plasma in atmosphere (highlighted in green). (b) Density map retrieved from (a), and (c) density profile extracted from (b) at x = 236 µm.
Source: By the author.

Plasma formation in air (nonthermal dynamics)

In the first investigation, illustrated in Figure 6.15, the plasma density temporal evolution was measured for 8 different delays after the plasma formation (100, 200, 300, 400, 500, 600, 700, and 800 fs). The zero-time was defined, with an uncertainty of tens of fs, when the interferogram displayed small fringe shifts in the expected plasma region. In Figure 6.15a, each plasma density map has an independent color scale that fades to white at $1/e$ of its peak intensity, except for the 100 fs map that fades at a higher value due to its high noise/signal ratio. The density maps also display their time delays (shown

in the labels), which can be correlated to the laser pump pulse propagation (also in the labels). Figure 6.15b presents the plasmas 1/e length and maximum density as a function of time, obtained from the maps shown in Figure 6.15a, where the length uncertainties were considered to be 5% of the measured values due to the CCD pixel size calibration for the plasma diameter. Both quantities show a saturation tendency near 800 fs, where the plasma peak density increases up to a maximum of $(2.2 \pm 0.1)\times10^{19}$ cm^{-3} and its longitudinal length reaches (210 ± 11) μm. Concerning this length, it can be considered as a steady state since this value corresponds to the distance defined by the laser confocal parameter and a possible filamentation in air[227], where the laser reaches an intensity that promotes the air ionization. Regarding the plasma density evolution, at the temporal scales explored in this study (sub-ps), the ionization occurs for atoms that are not resonant with the laser wavelength through the non-linear processes discussed in Section 2.1, thus this density evolution tendency is compatible with previous studies where the tunneling and barrier suppression ionizations promote a rapid ionization at few hundreds of femtoseconds and then establishes a stationary density[228, 229].

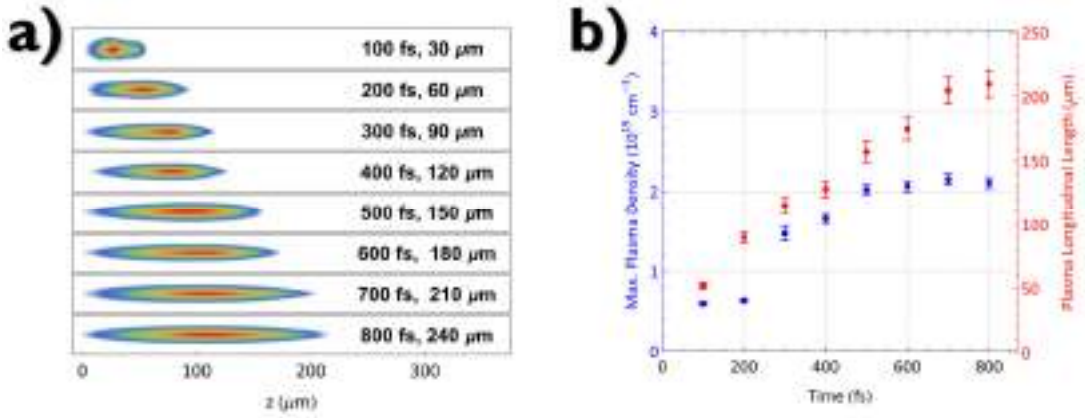

Figure 6.15 – (a) Side-view plasma density maps for 8 different delays after plasma formation. Labels: delay and corresponding pulse propagation position. (b) Temporal evolution of the plasma peak density and length.
Source: By the author.

Assuming that air is composed of 80% N_2 and 20% O_2, and that its number density at room temperature (300 K) and 1 atm is 2.5×10^{19} cm^{-3}, we can estimate its expected ionization for the applied laser intensity. This study considered, in a simplified way, that ionization occurs only when the intensity overcomes the BSI threshold[131, 230]. Therefore, using equation (2.3), the intensity thresholds I_{BSI} for all nitrogen and oxygen ionizations were calculated from the respective ionization energies $\mathcal{E}_{ion}$, as exhibited in Table 6.1.

Ionization state	Nitrogen		Oxygen	
	$\mathcal{E}_{ion}$ (eV)	I_{BSI} (10^{16} W/cm^2)	$\mathcal{E}_{ion}$ (eV)	I_{BSI} (10^{16} W/cm^2)
+1	14.53	0.018	13.62	0.014
+2	29.60	0.077	35.12	0.152
+3	47.45	0.225	54.94	0.405
+4	77.48	0.901	77.41	0.898
+5	97.89	1.469	113.9	2.693
+6	552.1	1032	138.2	4.053
+7	667.1	1617	739.3	2439
+8			871.4	3604

Table 6.1 – Ionization energies and BSI intensity thresholds for nitrogen and oxygen atoms.
Source: By the author.

To verify if the measured plasma densities are in accordance with the theoretical predictions, we assume that the laser pulses are in a TEM_{00} Gaussian beam, thus the intensity at the focus is $(1.2 \pm 0.3)\times10^{16}$ W/cm^2, enough to dissociate the N_2 and O_2 molecules, and to ionize their atoms 4 times, creating a plasma with a density of 2×10^{20} cm^{-3}. The peak intensity of the pulses is $(2.3 \pm 0.5)\times10^{16}$ W/cm^2, sufficient to ionize the nitrogen, but not the oxygen, to the 5+ state; taking the air composition into consideration, the plasma peak density can be as high as 2.4×10^{20} cm^{-3}. These predicted density values are about 9 and 11 times higher than the $(2.2 \pm 0.1)\times10^{19}$ cm^{-3} measured. Similar discrepancies are reported in the literature when using interferometry[125, 231], and the most probable causes for this disagreement are related to the expected plasma density, and the density retrieval algorithm. Regarding the theoretical expected density, our simple estimate may have overestimated its value since we assumed a constant intensity (apart from the peak intensity), and did not consider the laser intensity spatial profile, which would decrease the air ionization state in the beam wings due to lower intensities, resulting in a smaller integrated density[125]. Also, processes that mitigate the laser intensity, such as plasma defocusing near the focus[232, 233] could impair the ionization processes, reducing the free electron density. Finally, we are still devising ways to overcome difficulties associated with loss of contrast in the interferogram due to the modulations caused by the plasma. This effect causes an effective decrease in the

measured phase-shift since the resultant fringes are normalized by the lower ionization states that occupy a larger plasma region[234]. Although these problems must be overcome to allow absolute measurements of plasma density, the interferometer described here has good characteristics and is already in use for the characterization of relative density changes in generated plasmas as a function of time.

Plasma evolution in air (thermal dynamics)

Another investigation using the time-resolved MZI was to explore the laser-induced plasma evolution after its formation. In this investigation, the experimental conditions were the same as previously described. The maximum plasma density was measured after the plasma formation for delays ranging from 50 fs to 0.8 ns (maximum delay in our setup). At this time range, the plasma thermal effects are present, as well as possible recombination dynamics since femtosecond laser-induced plasmas in the air have a lifetime of a few nanoseconds[235, 236]. It is also possible to estimate the plasma temperature evolution. To be able to do this, a local thermal equilibrium (LTE) has to exist attending the McWhirter criterion[237, 238]:

$$n_e[cm^{-3}] \geq 1.6 \times 10^{12} \sqrt{T_e[K]} \left(\Delta\mathcal{E}_{ij}[eV]\right)^3, \tag{6.14}$$

where T_e is the plasma temperature, and $\Delta\mathcal{E}_{ij}$ is the energy difference between the transition levels i and j, with $i > j$. This criterion establishes a minimum local density to attain local thermal equilibrium by collisional processes, and can be used for ultrashort pulses originated plasmas[239]. As already discussed in this section, since is estimated that nitrogen is fully ionized to the state +4, and close to the laser peak it can reach the state +5, these two states were considered, resulting in $\Delta\mathcal{E}_{ij}$ = 20.4 eV. For temperatures under 100,000 K, the equation (6.14) states that the electronic density must be greater than ~4.3×10^{18} cm^{-3}, as is the case.

With these considerations, it is possible to estimate the plasma temperature from the maximum plasma density by applying the Saha equation[240]:

$$\frac{n_e n_i}{n_j} = \frac{2(2\pi m_e k_B T_e)^{3/2}}{h^3} \frac{\mathcal{U}_i(T_e)}{\mathcal{U}_j(T_e)} \exp\left\{-\frac{\Delta E_{ij}}{k_B T_e}\right\}, \tag{6.15}$$

where n_i and n_j are the ionic densities in states i and j, respectively, T_e is the plasma temperature, h is the Planck constant, and $\mathcal{U}_i(T_e)$ and $\mathcal{U}_j(T_e)$ are the ionic partition functions for the states i and j in LTE. These partition functions temperature dependent

values were obtained from the NIST Atomic Spectra Database[241] assuming T_e = 35,000 K, which is consistent with the expected temperature in this kind of investigation. To estimate of the ratio of the nitrogen +5 and +4 populations (n_i/n_j), we consider a Gaussian laser intensity distribution with a beamwaist of 4 µm and 2.3×10^{16} W/cm^2 to ionize the nitrogen atoms. As illustrated in Figure 6.16, the laser intensity profile produces an initial plasma density distribution that has a spatial dependence related to the various ionization intensities calculated from the nitrogen BSI thresholds, where the highest ionization +5 state is achieved only close to the peak.

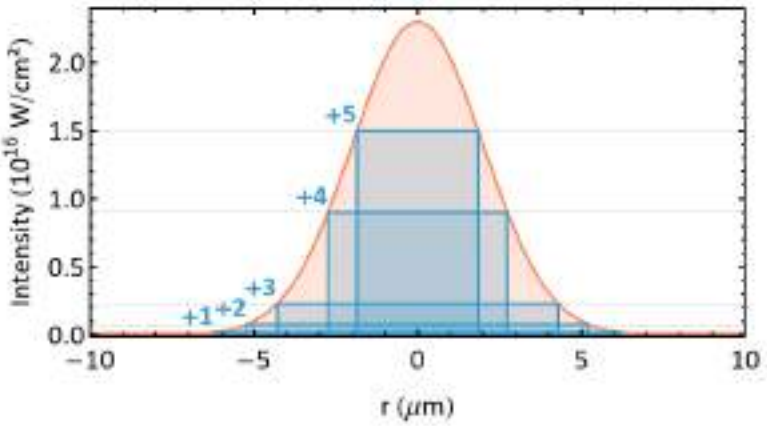

Figure 6.16 – Focus laser intensity with a Gaussian radial distribution (orange line) with the corresponding ionization intensities and positions for the nitrogen atom (blue lines).
Source: By the author.

From Figure 6.16 we could observe that the nitrogen population of the +5 state is restricted to a region with a radius $r_{+5} \leq 1.85$ µm, while the population of the +4 state is between 1.85 µm < $r_{+4} \leq 2.74$ µm. Considering that both the laser beam and the plasma have cylindrical symmetry around the laser axis, we could estimate the ratio n_i/n_j as being given by the number of ionized electrons per atom (4 or 5), multiplied by the areas defined by the ionization radii obtained from Figure 6.16:

$$\frac{n_i}{n_j} = \frac{5\,\pi\, r_{+5}^2}{4\,\pi\,(r_{+4}^2 - r_{+5}^2)} = \frac{5\,\pi\, 1.85^2}{4\,\pi\,(2.74^2 - 1.85^2)} \approx 1.05. \qquad (6.16)$$

Once the ratio n_i/n_j is evaluated, we can estimate the maximum plasma temperature through the equation (6.15) from the maximum plasma densities measured. Thus, Figure 6.17 exhibits the plasma density and estimated temperature evolutions in a delay range between 50 fs and 0.8 ns.

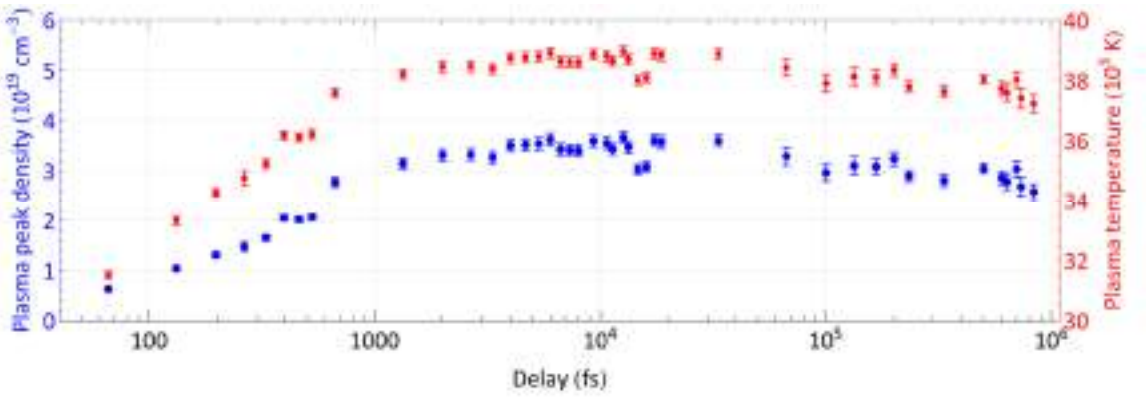

Figure 6.17 – Temporal evolution of laser-induced plasma maximum density (blue) and temperature (red).
Source: By the author.

The results presented in Figure 6.17 show an increasing trend in the maximum plasma density up to $(3.7 \pm 0.1)\times10^{19}$ cm^{-3} at about 13 ps, a much longer time than the pulse propagation period through the confocal region of the laser beam. This ~70% increase over the maximum plasma density reported in Figure 6.15 indicates plasma formation by a process other than photoionization since the laser pulse is not at the plasma region at these times. Therefore, impact ionization (collisional ionization) should be investigated[242, 243]. In addition, beyond 13 ps, the maximum plasma density decreases, which indicates that electron-ion recombination effects begin to be predominant[235, 244].

The estimated plasma temperature evolution follows the same behavior as the plasma density, with a peak of (39,000 ± 200) K at ~13 ps. Regarding the ionic population ratio, its value was assumed to be n_i/n_j = 1.05, but it could vary from 0.5 up to 1.5, changing the estimated temperature by less than 10%. Additionally, the partition functions could have been taken at any temperature between 10,000 K and 50,000 K and the estimated plasma temperature would change by no more than 3%, so after a few interactions we choose to use the partition functions at 35,000 K because this value is closer to the estimated plasma temperature along its evolution. Despite all this, the plasma temperature obtained is only an estimate, and it was calculated considering exclusively the nitrogen atoms because in the simple BSI model adopted all oxygen atoms are ionized to the final +4 state, with no population on the +5 state, so the Saha equation could be applied to this species also. To consider the oxygen, better population estimates, based on more complex ionization models and spatial distributions, would have to be used, but the values obtained give us an assessment of the temperatures reached by the plasma. Finally, although time delays longer than 0.8 ns could not be explored in this experimental setup, the density and temperature decreasing trends should become more evident as

longer times allow for more electron recombinations and cooling to the surrounding environment.

The findings exhibited in this section demonstrate the suitability of the time-resolved MZI to diagnose plasmas dimensions and density distributions, producing side-view interferograms with micrometric and femtosecond resolutions. Additionally, measurements of plasma in air are important to provide a better understanding of the plasma dynamics when generated by ultrashort laser pulses, a topic essential also for laser-plasma acceleration. These plasma results in the atmosphere give us directions to improve our methodology for this next step, which is to diagnose supersonic gas jets and the plasmas inside a vacuum chamber for further laser-electron acceleration studies in our laboratory.

6.4 Development of a time-resolved MZI in a vacuum chamber

After the initial tests using the time-resolved MZI in atmosphere to measure continuously supersonic gas jets (section 6.3.1) and laser-induced plasmas (section 6.3.2), the next step is to move the interferometer inside a vacuum chamber, where SM-LWFA experiments will be conducted. However, this change presents several challenges, such as the need of a pulsed gas flow to constrain the laser interaction with the gaseous target, ensuring an optimal energy transfer from the laser pulses to the wakefield, also to avoiding the electron bunches absorption by the residual atmosphere, and overloading the vacuum turbomolecular pump that is usually used in this kind of setup, breaking the vacuum. Furthermore, an electronic synchronization system is necessary for the pulsed valve because the pump and probe pulses must arrive at the target at a stationary gas flow condition (optimal reproducible interaction length and gas density) within a few ms after the valve aperture. The synchronization with the CCD aperture and its exposure time is also necessary to capture single shots. However, considering the limited probe pulse intensity generated by the BBO crystal, the single-shot capture drawback is the low intensity captured on CCD that generates noisy signals. For interferogram measurements in the atmospheric setup, this process was not necessary because of the stationary condition provided by the continuously gas flow (or atmosphere for plasma measurements), allowing the integration of 40 probe pulses during an exposure time of 10 ms. Thus, optimal synchronization between pump and probe pulses, pulsed gas valve,

and CCD, represents a real challenge for this experimental setup. Finally, the interferometer implementation inside a vacuum chamber implies the accommodation of the optical components in a restricted space, positioned according to the availability of windows for laser access and optical signal extraction, electric feedthroughs to control components remotely (translators, mirrors, lens, among others), and gaseous feedthrough for the high pressure gases.

A pulsed solenoid valve (VAC-750 psi, Parker Inc., displayed in Figure 5.5b) was used in the vacuum interferometer setup. This kind of valve is usually applied for laser electron acceleration studies, and it withstands backing pressure up to 50 bar. To operate the valve, a power driver was home-built. This driver is controlled by a square-wave external TTL signal from a Digital Delay Generator (DG535, Stanford Research Systems Inc.), that determines the valve opening and closing times; the TTL signal controls a high-speed optocoupler that switches a MOSFET, delivering the effective power of 11.2 W (28 VDC, 400 mA) to the solenoid valve, as shown in the scheme in Figure 6.18a. The Digital Delay Generator can be operated in internal trigger mode, or be triggered by the laser pulses.

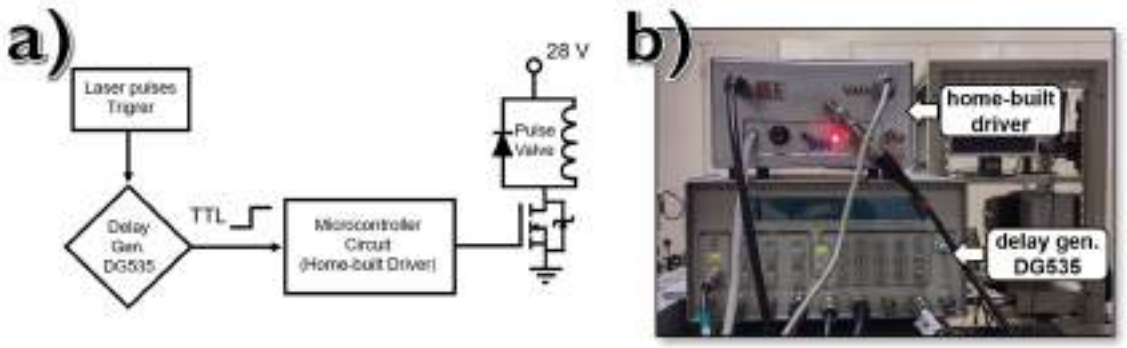

Figure 6.18 – Home-built driver for the pulsed solenoid valve. (a) steps involved in controlling the valve timing cycle operation. (b) photo of the home-built driver triggered by the Digital Delay Generator.

Source: By the author.

Concerning the vacuum chamber available to conduct future SM-LWFA studies, it has 50 cm of diameter, a volume of 5×10^4 cm^3, and reaches final pressures under 10^{-6} mbar using a Pfeiffer TMH 521/TMU 5231 turbomolecular pump with a flow rate of 0.52 m^3/s (for helium). This chamber has several access flanges for beam injection and instrumentation, and its walls are thick enough to block the expected ionizing radiation for the electron energies desired in the first stage (>10 MeV). The MZI setup was moved

inside the vacuum chamber along with the OAP and pulsed valve, and their positions have been optimized to the available space, while the pump-probe delay line (delay 1 in Figure 6.8) was kept in atmosphere. A scheme of the setup placed inside the vacuum chamber is shown in Figure 6.19 with the gas line and electric feedthroughs to control the positioning and angles of optical components. Once the spectrometer used to find the spectral fringes is not vacuum compatible, it is used with the chamber opened, the delay 2 (REF arm, Figure 6.8) is adjusted to the "zero-delay" position, and it is removed from the chamber before making vacuum. Finally, the background pressure inside this vacuum chamber during the gas jet expansion is smaller than 10^{-3} mbar for N_2 at 50 bar of backing pressure, much lower than the one in the small vacuum chamber.

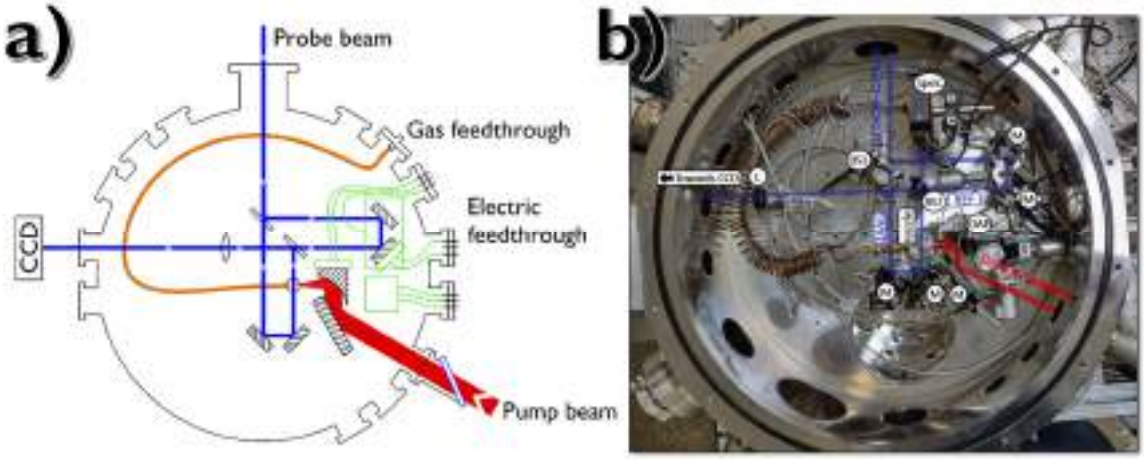

Figure 6.19 – (a) Schematic time-resolved Mach-Zehnder-like interferometer placed inside the vacuum chamber. (b) A photo of the vacuum chamber opened showing the interferometer setup, including the spectrometer.

Source: By the author.

The biggest challenge to obtain interferograms from the vacuum chamber is the low-intensity coming from the single-shot measurement. However, we had been working on different approaches to solving this issue, such as illuminating the CCD directly with a low-intensity flashlamp to favor the appearance of fringes and improve the contrast of the interferogram fringes recorded by the CCD. Using this, we could synchronize the laser pulses with the valve aperture. The best results were obtained by delaying the pulses by 3.9 ms after the valve aperture, considering a valve dead time of 1.3 ms (for a 50 bar backing pressure) after sending the opening signal. Under these conditions, the probe pulse hits the gas jet at an optimal time when its profile presents a high-density region and low diffusion. The externally triggered CCD used in the atmospheric experiments

could not be used in the vacuum studies due to its fixed gain that was not enough to capture single-shot interferograms. It was replaced by a variable gain CCD, that has no external trigger synchronization, but could be software triggered by a spike in the measured signal. Using this internal trigger option and adjusting the CCD gain, we could measure single shots of N_2 gas jets interferograms with a backing pressure of 50 bar, as illustrated in Figure 6.20 for a nozzle with $\emptyset_e$ = 260 µm and $\emptyset_t$ = 160 µm. Once this setup has a non-deterministic capture time start, the gas jet interferograms are not easily reproducible and present a residual gas atmosphere inside the vacuum chamber due to a non-optimal capture time. Thus, only a few manufactured nozzles had their gas jet well diagnosed, mainly the nozzles with larger diameters due to the higher gas flow. A CCD with variable signal gain and external trigger entrance is required for further single-shot, reproducible, measurements, with a low noise-signal ratio, and at optimal measurement time.

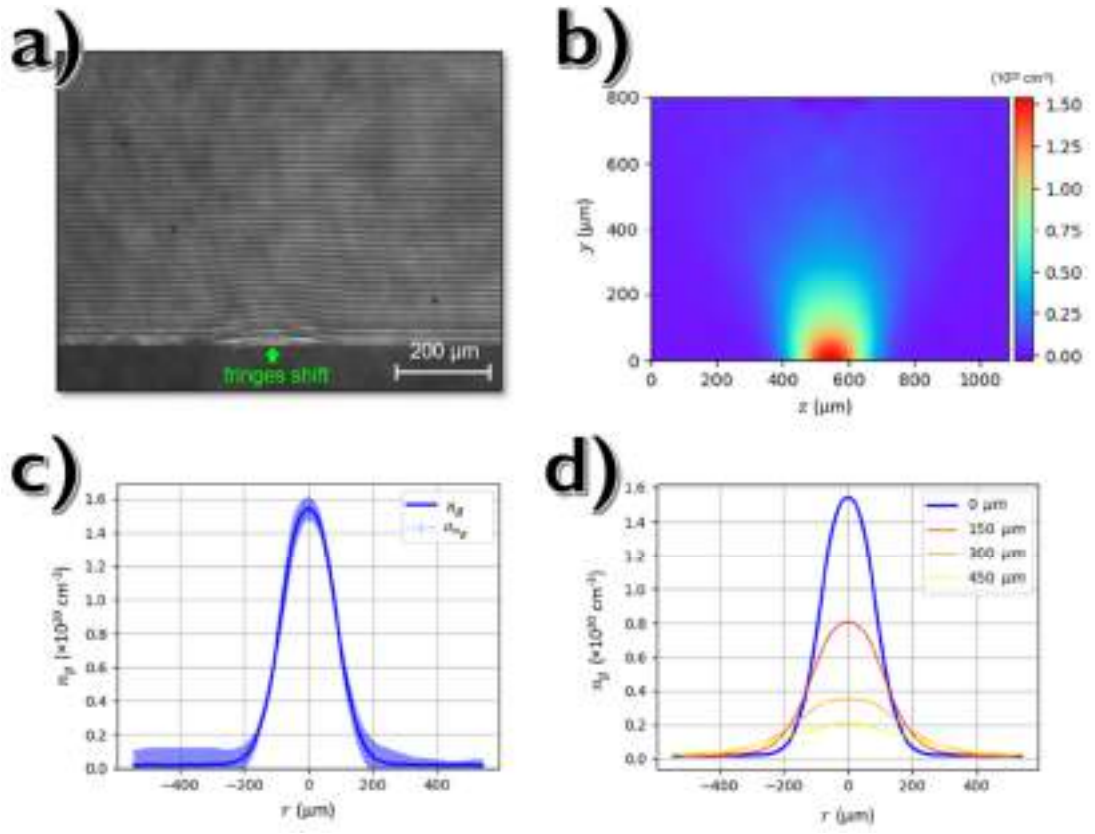

Figure 6.20 – Nitrogen jet expanding in vacuum from $\emptyset_e$ = 260 µm and $\emptyset_t$ = 160 µm nozzle and a backing pressure of 50 bar. (a) interferogram, (b) gas density map, (c) density profile close to the nozzle exit (y = 0 µm), and (d) density profiles for y = 0, 150, 300, and 450 µm above the nozzle exit, extracted from density map in (b).

Source: By the author.

By analyzing the gas jet results from the vacuum chamber, the interferogram exhibited in Figure 6.20a presents a worse contrast as well as a higher noise-signal ratio than others interferograms shown in this thesis. However, from this interferogram the software obtained the gas density map (Figure 6.20b) without noticeable computational artifacts, which should be a consequence of a better vacuum environment also capable to reduce mechanical vibrations from the pumps during the single-shot measurement, and also density profiles with small uncertainties (Figure 6.20c), demonstrating that the density retrieval algorithms can produce good results even from noisy interferograms. As shown in Figure 6.20c, the peak density close to the nozzle exit was $(1.5\pm0.7)\times10^{20}$ cm^{-3}, a value of only 50% above the theoretically predicted 1×10^{20} cm^{-3} by the quasi-1D model[177]. This lower discrepancy when compared to the values measured using the small vacuum chamber also could be an indication of the better vacuum environment. As shown in Figure 6.20d, the density profiles for the 4 heights from the nozzle exit (y = 0, 150, 300, and 450 µm) exhibit, at first glance, the same trend of decreasing density with increasing distance from the nozzle exit, but even for heights above 150 µm there is still a density profile with high values close to 10^{20} cm^{-3}. Considering that the laser pulses must be tightly focused into the gas jets at $y \approx 100$ µm and also assuming a full ionization of the gaseous target, the plasma formed will achieve densities for H_2 close to simulated values in Section 3.2. If He is used, higher densities can be reached since it presents a smaller density drop after the exit of a nozzle due to its bigger κ, as can be seen in Figure 6.21.

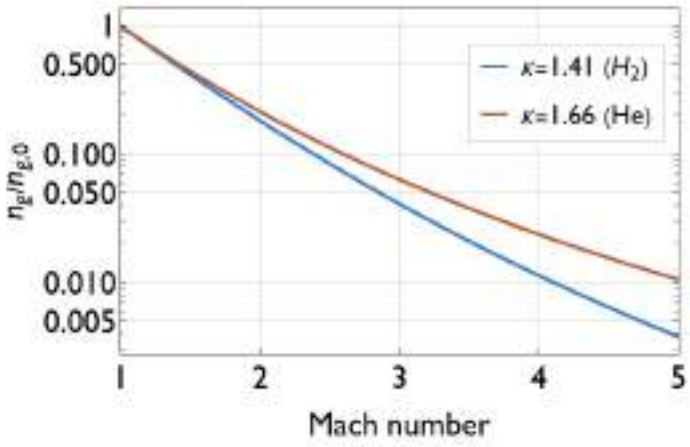

Figure 6.21 – Quasi-1D model dependence on the Mach Number with the ratio between the maximum gas molecular density at nozzle exit and backing chamber for H_2 (blue line) and He (brown line).

Source: By the author.

Due to the reported issues in the single-shot, laser-induced plasma measurements in vacuum were not performed during this PhD. However, some experiments checking the synchronization between the pump pulses and the valve aperture were carried out using N_2 and other noble gases. Figure 6.22 exhibits a photo taken from a vacuum chamber window during a test with He and a nozzle with $\emptyset_e$ = 300 µm and $\emptyset_t$ = 150 µm. A laser pulse hits the target close to the nozzle, creates a plasma, and the excited atoms leave the laser interaction region at supersonic speeds, revealing the jet shape as they decay and emit light.

Figure 6.22 – Helium gas jet produced by a de Laval nozzle in vacuum, exhibiting a plasma excited by an ultrashort pulse. The jet shape can be observed by the light emitted by helium moving at supersonic speeds out of the laser interaction region.

Source: By the author.

7 CONCLUSIONS AND OUTLOOK

In this thesis, a successful method to micromachine de Laval nozzles in alumina by trepanning with ultrashort laser pulses was developed. The manufactured nozzles exhibit high circularity and smooth internal walls, which should decrease turbulence in the jet targets created. Although this work presented only a few examples, the nozzle features, as well as the gas jets generated by them, are general for all alumina manufactured nozzles, proving a good reproducibility of our methodology. By changing the machining parameters we could control the nozzle throat and exit diameters, which are the primary features that define the jet Mach number and geometry of the gas jets. An outlook of this investigation is to improve the control of the nozzle shape, which introduces second-order corrections on the target density profiles, which should be important for subsequent electron acceleration dynamics.

In addition, this work presented the development and assemblage of a novel time-resolved Mach-Zehnder-like interferometer coupled to a pump-probe setup capable to diagnose gas jet targets and laser-induced plasmas with micrometric and femtosecond resolutions. The use of a spectrometer proved to be a fundamental tool to find the pulses temporal overlap, readily providing the correct reference arm length to create spatial interferograms to be recorded by a CCD. As a first step, this setup was built in atmosphere, and gas jet characterization with backing pressures up to 50 bar at continuously flow was performed using a small vacuum chamber that fits the nozzle. Furthermore, an original time-resolved investigation of the laser-induced plasma generated in air was performed using the pump-probe technique, where its characteristics could be explored during plasma formation (nonthermal dynamics) and evolution to longer times (thermal dynamics). The results showed that the interferometer can be used to characterize a gas jet expansion in vacuum, obtaining phase-shift maps that retrieve its geometry and density, as well as the time evolution of the laser-induced plasma, also allowing the estimation of its density. Finally, the initial steps of the implementation the interferometer inside a vacuum chamber were presented and discussed, depicting the challenges involved in this new step, such as pulsed gas valve installation, synchronization between different components, and single-shot measurement on a CCD. Despite these implementation difficulties, measurements of gas jet expansion in vacuum

were accomplished, revealing a clear enhancement compared to those taken using the small vacuum chamber. As an outlook of this investigation, the replacement of the current CCD by one with an external trigger and variable gain should greatly improve the laser-induced plasma measurements inside the vacuum chamber. This experimental setup will soon be operating as desired, being an essential diagnostic tool for future laser-electron acceleration studies at IPEN. This upgrade opens important paths to research in our group besides the aimed LWFA field, since in the short term this setup could be used to investigate fundamental research in laser-induced ionization for different gases in vacuum, pressures, interaction length, etc, demonstrating a potential for the future publications as was recently done in Applied Optics[123].

The interferogram analysis produced during this work motivates our group to develop better algorithms for processing these data which lead us to develop and made available Python codes as installable software for interferogram analysis of gas jets and laser-induced plasmas[214, 215]. Those softwares proved to be suitable for our purposes, being capable to retrieve the targets density distribution with good agreement with theoretical predictions. However, as an outlook, those softwares can be enhanced and updated to improve the data analysis, which may reduce the discrepancies between theoretical predictions and experimental measurements.

Our research group has a cooperation agreement with the Extreme Light Laboratory (ELL) at the University of Nebraska-Lincoln (UNL). This research group is a current leader in electron acceleration by LWFA and their applications[245, 246, 247, 248], owning two ultra-high-intensity ultrashort laser systems with pulse peak power up to 7 TW (Archimedes), and up to 0.7 PW (Diocles). Based on the agreement, I was a visiting PhD student at ELL for 6 months (from September/2021 to February/2022), where I gained skills working with high-peak power lasers (>100 TW) as well as an installation for LWFA experiments. In October 2022, I had the opportunity to return to ELL with my advisor and more two researchers within the LaserNetUS Cycle 3 scientific mission[121] for 1 month. The goals of this project included preliminary SM-LWFA experiments using the de Laval nozzles manufactured at IPEN (discussed in Chapter 5), aiming to validate the efficiency of our nozzle fabrication technique and checking the validity of our PIC simulations predictions for SM-LWFA electron bunches agree with our (discussed in Chapter 3). However, 1 month at ELL proved to be a short period for the experimental activities required for our goals, and then although the participants of this mission along

with the ELL staff had worked hard during this month, no significant electron bunches (> MeV) were observed. Most of the time was spent on activities before the laser-electron acceleration, such as alignment of the driven pulses inside of the target vacuum chamber, achieving the required beamwaist after the focalization, assembly of diagnostic systems for gas jets (Nomarski interferometer) and electrons energies (Thomson spectrometer). Thus, a short time could be directed to acceleration tests, meaning that we did not have time to optimize this experiment to investigate the reasons for not observing the expected electron energies. In spite of this, important achievements were achieved in this scientific mission for both our team and the ELL staff, which motivated both sides to keep and reinforce the collaboration agreement. The next opportunity to return to ELL and continue this investigation was applied to LaserNetUS Cycle 5 project call[249], whose the acceptance result has yet to be announced. In addition, both groups have discussed future collaborations which ensure that these missions should continue soon, being an outlook for a future application of our manufactured nozzles.

All results and their discussions shown in this thesis contribute towards the greater aim of our research group to establish the first laser-electron accelerator infrastructure in Latin America, which will make IPEN a pioneer in this research area. Thus, at the end of this step, I am confident that the PhD outcomes have been successfully completed, becoming one more kick-off to this greater project.

ACADEMIC PRODUCTION

Here I present my academic production during the whole PhD period (May 2018 – May 2023) divided in topics related to my academic formation and research dissemination.

Publications

1. APPLIED OPTICS 2023
   E. P. Maldonado, R. E. Samad, **A. V. F. Zuffi**, N. D. Viera. Simulation of self-modulated laser wakefield acceleration using few TW in the downramp injection and ionization injection regimes. https://doi.org/10.1364/AO.477401

2. JOURNAL OF THE OPTICAL SOCIETY OF AMERICA B 2023
   E. P. Maldonado, R. E. Samad, **A. V. F. Zuffi**, J. R. dos Santos, N. D. Viera. Impact of He+N2 concentration on self-modulated laser wakefield acceleration driven by pulses of a few TW. https://doi.org/10.1364/JOSAB.482305

3. APPLIED OPTICS 2023
   A. V. F. Zuffi, J. R. dos Santos, E. P. Maldonado, N. D. Viera, R. E. Samad. Femtosecond Laser-Plasma Dynamics Study by a Time-Resolved Mach-Zehnder-Like Interferometer. https://doi.org/10.1364/AO.477395

4. PHYSICAL REVIEW A 2022
   A. V. F. Zuffi, N. D. Viera, R. E. Samad. Below-threshold-harmonics-generation limitation due to laser-induced ionization in noble gases. https://doi.org/10.1103/physreva.105.023112

Conference proceedings

1. 2022 SBFOTON CONFERENCE 2022
   A. V. F. Zuffi, F.B.D. Tabacow, N. D. Viera, R. E. Samad. Ultrafast laser micromachining of submillimetric de Laval nozzles in alumina for laser electron acceleration. https://doi.org/10.1109/sbfotoniopc54450.2022.9992490

2. 2022 LATIN AMERICA OPTICS AND PHOTONICS CONFERENCE 2022
   A. V. F. Zuffi, E. P. Maldonado, N. D. Viera, R. E. Samad. Time-Resolved Femtosecond Laser-Plasma Measurements by a Mach-Zehnder-Like Interferometer. https://doi.org/10.1364/LAOP.2022.Tu4A.49

3. 2022 LATIN AMERICA OPTICS AND PHOTONICS CONFERENCE 2022
   E. P. Maldonado, R. E. Samad, **A. V. F. Zuffi**, N. D. Viera. Simulation of a Laser Wakefield Accelerator in Downramp Injection Regime Suitable for High Repetition Rates. https://doi.org/10.1364/LAOP.2022.Tu1C.7

4. 2022 LATIN AMERICA OPTICS AND PHOTONICS CONFERENCE 2022
A. V. F. Zuffi, N. D. Viera, R. E. Samad. Observation of Third-Harmonic Saturation in Helium due to Ionization Depletion. https://doi.org/10.1364/LAOP.2022.Th1B.7

5. 12th INTERNATIONAL PARTICLE ACCELERATOR CONFERENCE 2021
A. Bonatto, E.P. Maldonado, R.P. Nunes, **A.V.F. Zuffi**, F.B.D. Tabacow, R.E. Samad, N.D. Vieira. On the Development of a Low Peak-Power, High Repetition-Rate Laser Plasma Accelerator at IPEN. https://doi.org/10.18429/JACoW-IPAC2021-TUPAB141

6. 2021 SBFOTON CONFERENCE 2021
A. V. F. Zuffi, N. D. Viera, R. E. Samad. Development of a modified Mach-Zehnder interferometer for time and space density measurements for laser wakefield acceleration. https://doi.org/10.1109/sbfotoniopc50774.2021.9461961

7. 2021 SBFOTON CONFERENCE 2021
F.B.D. Tabacow, **A.V.F. Zuffi**, E.P. Maldonado, R.E. Samad, N.D. Vieira. Theoretical and experimental study of supersonic gas jet targets for laser wakefield acceleration. https://doi.org/10.1109/sbfotoniopc50774.2021.9461936

8. 2021 SBFOTON CONFERENCE 2021
B.B. Chiomento, **A.V.F. Zuffi**, N.D. Vieira, F.B.D. Tabacow, E.P. Maldonado, R.E. Samad. Development of dielectric de Laval nozzles for laser electron acceleration by ultrashort pulses micromachining.
https://doi.org/10.1109/sbfotoniopc50774.2021.9461928

9. 2021 SBFOTON CONFERENCE 2021
N.D. Vieira, E.P. Maldonado, A. Bonatto, R.P. Nunes, S. Banerjee, F.A. Genezini, M. Moralles, **A.V.F. Zuffi**, R.E. Samad. Laser wakefield electron accelerator: possible use for radioisotope production.
https://doi.org/10.1109/sbfotoniopc50774.2021.9461976

10. 2019 INTERNATIONAL NUCLEAR ATLANTIC CONFERENCE 2019
N. D. Viera, S. Banerjee, E. P. Maldonado, **A. V. F. Zuffi**, F. B. D. Tabacow, R. E. Samad. Laser Particle Acceleration in Brazil.
http://repositorio.ipen.br/handle/123456789/30550

11. 2019 SBFOTON CONFERENCE 2019
A. V. F. Zuffi, A. A. Almeida, N.D. Vieira, R. E. Samad. Below Threshold Harmonics Dependence with Phase-Matching Parameters in Argon.
https://doi.org/10.1109/sbfoton-iopc.2019.8910189

12. 2019 SBFOTON CONFERENCE 2019
E. P. Maldonado, R. E. Samad, **A. V. F. Zuffi**, F. B. D. Tabacow, N. D. Viera, Self-modulated laser-plasma acceleration in a H2 gas target, simulated in a spectral particle-in-cell algorithm: wakefield and electron bunch properties.
https://doi.org/10.1109/sbfoton-iopc.2019.8910252

13. 2019 FRONTIERS IN OPTICS + LASER SCIENCE 2019
A. V. F. Zuffi, A. A. Almeida, N.D. Vieira, R. E. Samad. Development of glass nozzles for below threshold harmonics and high harmonic generation. https://doi.org/10.1364/FIO.2019.JTu3A.44

14. 2018 LATIN AMERICA OPTICS AND PHOTONICS CONFERENCE 2018
A. V. F. Zuffi, A. A. Almeida, N. D. Viera, R. E. Samad. Below Threshold Harmonics Beams Characterization Using the Knife-Edge Technique https://doi.org/10.1364/LAOP.2018.Tu4A.4

15. 2018 SBFOTON CONFERENCE 2018
A. V. F. Zuffi, A. A. Almeida, N. D. Viera, R. E. Samad. Characterization of Below Threshold Harmonics Generated in Argon by Ultrashort Laser Pulses. https://doi.org/10.1109/sbfoton-iopc.2018.8610890

16. 2018 SBFOTON CONFERENCE 2018
R. E. Samad, **A. V. F. Zuffi**, E. P. Maldonado, N. D. Viera. Development and Optical Characterization of Supersonic Gas Targets for High-Intensity Laser Plasma Studies. https://doi.org/10.1109/sbfoton-iopc.2018.8610903

Software registration

1. ZENODO 2023
J. R. dos Santos, **A. V. F. Zuffi**, N. D. Viera, E. P. Maldonado, R. E. Samad. INTERFEROGRAM ANALYSIS GAS JET: INITIAL RELEASE (VERSION 1.0). Software is available in the repository <https://zenodo.org/record/7778947>. https://doi.org/10.5281/zenodo.7778947

2. ZENODO 2023
J. R. dos Santos, **A. V. F. Zuffi**, N. D. Viera, E. P. Maldonado, R. E. Samad. INTERFEROGRAM ANALYSIS LIP: INITIAL RELEASE (VERSION 1.0). Software is available in the repository<https://zenodo.org/record/7864173#.ZEk7PHbMK3B>. https://doi.org/ 10.5281/zenodo.7864173

Oral presentations

Oct 2022 **Ultrafast Laser Micromachining of Submillimetric de Laval Nozzles in Alumina for Laser Electron Acceleration**, in SBFoton International Optics and Photonics Conference 2022 (Recife, Brazil)

May 2021 **Development of a Modified Mach-Zehnder Interferometer for Time and Space Density Measurements for Laser Wakefield Acceleration**, in SBFoton International Optics and Photonics Conference 2021 (online)

Oct 2019 **Below Threshold Harmonics Dependence with Phase-Matching Parameters in Argon**, in SBFoton International Optics and Photonics Conference 2019 (São Paulo, Brazil)

Oct 2018 **Characterization of Below Threshold Harmonics Generated in Argon by Ultrashort Laser Pulses**, in SBFoton International Optics and Photonics Conference 2018 (Campinas, Brazil)

Poster presentations

Mar 2023 **Laser-induced plasma dynamics in air measured by a femtosecond time-resolved Mach-Zehnder-like interferometer**, in Autumn School on Ultrafast Lasers & Ultrafast Optics Conference XIII (Bariloche, Argentina)

Aug 2022 **Time-Resolved Femtosecond Laser-Plasma Measurements by a Mach-Zehnder-Like Interferometer**, in Latin America Optics & Photonics Conference 2022 (Recife, Brazil)

Aug 2021 **Development of de Laval Nozzles and a Time-resolved Mach–Zehnder-like Interferometer for Laser Wakefield Acceleration Studies at IPEN**, in 2021 LaserNetUS User Meeting (online)

Sep 2019 **Development of glass nozzles for below threshold harmonics and high harmonic generation**, in Frontiers in Optics + Laser Science 2019 (Washington DC, US)

Nov 2018 **Below Threshold Harmonics Beams Characterization Using the Knife-Edge Technique**, in Latin America Optics & Photonics Conference 2018 (Lima, Peru)

Jul 2018 **Optical Characterization of Gas Jets for Electron Laser Acceleration**, in São Paulo School of Advanced Science on Frontiers in Lasers and their Applications (São Paulo, Brazil)

Awards

May 2021 **1st place Student Paper Award in 2021 SBFoton Conference** - "Development of a modified Mach-Zehnder interferometer for time and space density measurements for laser wakefield acceleration"

REFERENCES

[1] COCKCROTT, J. D. and WALTON, E. T. S. Experiments with high velocity positive ions (I) Further developments in the method of obtaining high velocity positive ions. **Proceedings of the Royal Society of London Series a-Containing Papers of a Mathematical and Physical Character,** v. 136, n. 830, p. 620-630, 1932.

[2] COCKCROFT, J. D. and WALTON, E. T. S. Experiments with high velocity positive ions II - The disintegration of elements by high velocity protons. **Proceedings of the Royal Society of London Series a-Containing Papers of a Mathematical and Physical Character,** v. 137, n. 831, p. 229-242, 1932.

[3] LIVINGSTON, M. S. and BLEWETT, J. P. **Particle accelerators**. New York, : McGraw-Hill, 1962.

[4] CHAO, A. W. and CHOU, W. **Reviews of accelerator science and technology**. Hackensack, New Jersey: World Scientific, 2017.

[5] EVANS, L. and BRYANT, P. LHC Machine. **Journal of Instrumentation,** v. 3, 2008.

[6] HARRISON, M., PEGGS, S. and ROSER, T. The RHIC accelerator. **Annual Review of Nuclear and Particle Science,** v. 52, p. 425-469, 2002.

[7] LIU, L. et al. The Sirius project. **Journal of Synchrotron Radiation,** v. 21, p. 904-911, 2014.

[8] PAGANETTI, H. **Proton Beam Therapy**: IOP Publishing 2017.

[9] DOSANJH, M. **From Particle Physics to Medical Applications**: IOP Publishing 2017.

[10] GIULIETTI, A. **Laser-Driven Particle Acceleration Towards Radiobiology and Medicine**. Springer International Publishing, 2016.

[11] KATSOULEAS, T. Accelerator physics - Electrons hang ten on laser wake. **Nature,** v. 431, n. 7008, p. 515-516, 2004.

[12] TAJIMA, T., NAKAJIMA, K. and MOUROU, G. Laser acceleration. **Rivista Del Nuovo Cimento,** v. 40, n. 2, p. 33-102, 2017.

[13] PATHAK, N. C. **Laser Pulse Propagation in Plasmas and its implication on frequency up-shift and electron acceleration**. 2011. 165 (Ph.D. Thesis). University of Pisa, Pisa, Italy.

[14] TAJIMA, T. and DAWSON, J. M. Laser Electron Accelerator. **Physical Review Letters,** v. 43, n. 4, p. 267-270, 1979.

[15] MALKA, V. Plasma Wake Accelerators: Introduction and Historical Overview. **Cern Yellow Rep.,** v. vol. CERN-2016-, p. 1–28, 2016.

[16] JOSHI, C. et al. Ultrahigh Gradient Particle-Acceleration by Intense Laser-Driven Plasma-Density Waves. **Nature,** v. 311, n. 5986, p. 525-529, 1984.

[17] SPRANGLE, P. et al. Laser Wakefield Acceleration and Relativistic Optical Guiding. **Applied Physics Letters,** v. 53, n. 22, p. 2146-2148, 1988.

[18] CHEN, P. et al. Acceleration of Electrons by the Interaction of a Bunched Electron-Beam with a Plasma. **Physical Review Letters,** v. 54, n. 7, p. 693-696, 1985.

[19] FAURE, J. et al. A laser-plasma accelerator producing monoenergetic electron beams. **Nature,** v. 431, n. 7008, p. 541-544, 2004.

[20] GEDDES, C. G. et al. High-quality electron beams from a laser wakefield accelerator using plasma-channel guiding. **Nature,** v. 431, n. 7008, p. 538-41, 2004.

[21] MANGLES, S. P. et al. Monoenergetic beams of relativistic electrons from intense laser-plasma interactions. **Nature,** v. 431, n. 7008, p. 535-8, 2004.

[22] ESAREY, E., SCHROEDER, C. B. and LEEMANS, W. P. Physics of laser-driven plasma-based electron accelerators. **Reviews of Modern Physics,** v. 81, n. 3, p. 1229-1285, 2009.

[23] BIRSS, R. R. Ponderomotive forces. **Physics Education,** v. 4, n. 1, p. 33-39, 1969.

[24] BOOT, H. A. H. and R.-S.-HARVIE, R. B. Charged Particles in a Non-uniform Radio-frequency Field. **Nature,** v. 180, n. 4596, p. 1187-1187, 1957.

[25] KALMYKOV, S. et al. Electron Self-Injection and Trapping into an Evolving Plasma Bubble. **Physical Review Letters,** v. 103, n. 13, 2009.

[26] SUK, H. et al. Plasma electron trapping and acceleration in a plasma wake field using a density transition. **Physical Review Letters,** v. 86, n. 6, p. 1011-1014, 2001.

[27] MCGUFFEY, C. et al. Ionization Induced Trapping in a Laser Wakefield Accelerator. **Physical Review Letters,** v. 104, n. 2, 2010.

[28] GONSALVES, A. J. et al. Petawatt Laser Guiding and Electron Beam Acceleration to 8 GeV in a Laser-Heated Capillary Discharge Waveguide. **Physical Review Letters,** v. 122, n. 8, 2019.

[29] LEEMANS, W. P. et al. GeV electron beams from a centimetre-scale accelerator. **Nature Physics,** v. 2, n. 10, p. 696-699, 2006.

[30] MIAO, B. et al. Multi-GeV Electron Bunches from an All-Optical Laser Wakefield Accelerator. **Physical Review X,** v. 12, n. 3, 2022.

[31] LEEMANS, W. P. et al. GeV electron beams from a centimetre-scale accelerator. **Nature Physics,** v. 2, n. 10, p. 696-699, 2006.

[32] VEISZ, L. et al. **Complete characterization of laser wakefield acceleration**: SPIE. 8079**:** 807906 p. 2011.

[33] HOOKER, S. M. Developments in laser-driven plasma accelerators. **Nature Photonics,** v. 7, n. 10, p. 775-782, 2013.

[34] MALKA, V. Laser Plasma Accelerators. In: MCKENNA, P.;NEELY, D., *et al* (Ed.). **Laser-Plasma Interactions and Applications**. Heidelberg: Springer, 2013. p.281-301.

[35] FERMILAB. International Committee for Future Accelerators. 2018. Available in: < http://icfa.fnal.gov/ >. Acess in: Fev 2018.

[36] U.S. DEPARTMENT OF ENERGY - OFFICE OF SCIENCE. **Advanced Accelerator Development Strategy Report**. p.22. 2016

[37] PHUOC, K. T. et al. Laser based synchrotron radiation. **Physics of Plasmas,** v. 12, n. 2, p. 023101, 2005.

[38] ALBERT, F. **Laser Wakefield Accelerators: Next-Generation Light Sources**. Optics and Photonics News: The Optical Society. 29**:** 42-49 p. 2018.

[39] NEMOTO, K. et al. Laser-triggered ion acceleration and table top isotope production. **Applied Physics Letters,** v. 78, n. 5, p. 595-597, 2001.

[40] SPENCER, I. et al. Laser generation of proton beams for the production of short-lived positron emitting radioisotopes. **Nuclear Instruments & Methods in Physics Research Section B-Beam Interactions with Materials and Atoms,** v. 183, n. 3-4, p. 449-458, 2001.

[41] LEDINGHAM, K. et al. Towards Laser Driven Hadron Cancer Radiotherapy: A Review of Progress. **Applied Sciences,** v. 4, n. 3, p. 402-443, 2014.

[42] DAIDO, H., NISHIUCHI, M. and PIROZHKOV, A. S. Review of laser-driven ion sources and their applications. **Reports on Progress in Physics,** v. 75, n. 5, p. 056401, 2012.

[43] MACCHI, A., BORGHESI, M. and PASSONI, M. Ion acceleration by superintense laser-plasma interaction. **Reviews of Modern Physics,** v. 85, n. 2, p. 751-793, 2013.

[44] LEEMANS, W. P. et al. Multi-GeV Electron Beams from Capillary-Discharge-Guided Subpetawatt Laser Pulses in the Self-Trapping Regime. **Physical Review Letters,** v. 113, n. 24, 2014.

[45] HAFZ, N. A. M. et al. Generation of high-quality electron beams by ionization injection in a single acceleration stage. **High Power Laser Science and Engineering,** v. 4, 2016.

[46] LU, W. et al. Generating multi-GeV electron bunches using single stage laser wakefield acceleration in a 3D nonlinear regime. **Physical Review Special Topics-Accelerators and Beams,** v. 10, n. 6, 2007.

[47] "The International Committee on Ultra-High Intensity Lasers". (ICUIL), 2019. Available in: < https://www.icuil.org/ >. Acess in: Mar 2019.

[48] SALEHI, F. et al. Laser-Accelerated, Low-Divergence 15-MeV Quasimonoenergetic Electron Bunches at 1 kHz. **Physical Review X,** v. 11, n. 2, 2021.

[49] ALBERT, F. and THOMAS, A. G. R. Applications of laser wakefield accelerator-based light sources. **Plasma Physics and Controlled Fusion,** v. 58, n. 10, 2016.

[50] FAURE, J. et al. A review of recent progress on laser-plasma acceleration at kHz repetition rate. **Plasma Physics and Controlled Fusion,** v. 61, n. 1, 2019.

[51] NAGY, T., SIMON, P. and VEISZ, L. High-energy few-cycle pulses: post-compression techniques. **Advances in Physics: X,** v. 6, n. 1, p. 1845795, 2021.

[52] TRÄGER, F. **Springer handbook of lasers and optics**. New York: Springer, 2007.

[53] NISOLI, M. et al. Compression of high-energy laser pulses below 5 fs. **Optics Letters,** v. 22, n. 8, p. 522-524, 1997.

[54] APOLONSKI, A. et al. Controlling the phase evolution of few-cycle light pulses. **Physical Review Letters,** v. 85, n. 4, p. 740-743, 2000.

[55] NAJMUDIN, Z. et al. Self-modulated wakefield and forced laser wakefield acceleration of electrons. **Physics of Plasmas,** v. 10, n. 5, p. 2071-2077, 2003.

[56] GOERS, A. J. et al. Multi-MeV Electron Acceleration by Subterawatt Laser Pulses. **Physical Review Letters,** v. 115, n. 19, 2015.

[57] WOODBURY, D. et al. Laser wakefield acceleration with mid-IR laser pulses. **Optics Letters,** v. 43, n. 5, p. 1131-1134, 2018.

[58] MALDONADO, E. P. et al. Study of quasimonoenergetic electron bunch generation in self-modulated laser wakefield acceleration using TW or sub-TW ultrashort laser pulses. **AIP Advances,** v. 11, p. 065116, 2021.

[59] LEMOS, N. et al. Bremsstrahlung hard x-ray source driven by an electron beam from a self-modulated laser wakefield accelerator. **Plasma Physics and Controlled Fusion,** v. 60, n. 5, p. 054008, 2018.

[60] NICKS, B. S. et al. Laser-wakefield application to oncology. **International Journal of Modern Physics A,** v. 34, n. 34, 2019.

[61] ROVIGE, L. et al. Optimization and stabilization of a kilohertz laser-plasma accelerator. **Physics of Plasmas,** v. 28, n. 3, p. 033105, 2021.

[62] SALEHI, F. et al. MeV electron acceleration at 1 kHz with <10 mJ laser pulses. **Optics Letters,** v. 42, n. 2, p. 215-218, 2017.

[63] DARROW, C. B. et al. Strongly Coupled Stimulated Raman Backscatter from Subpicosecond Laser-Plasma Interactions. **Physical Review Letters,** v. 69, n. 3, p. 442-445, 1992.

[64] JOSHI, C. et al. Forward Raman Instability and Electron Acceleration. **Physical Review Letters,** v. 47, n. 18, p. 1285-1288, 1981.

[65] ANTONSEN, T. M. and MORA, P. Self-Focusing and Raman-Scattering of Laser-Pulses in Tenuous Plasmas. **Physical Review Letters,** v. 69, n. 15, p. 2204-2207, 1992.

[66] ESAREY, E., KRALL, J. and SPRANGLE, P. Envelope Analysis of Intense Laser-Pulse Self-Modulation in Plasmas. **Physical Review Letters,** v. 72, n. 18, p. 2887-2890, 1994.

[67] MALKA, V. Laser plasma accelerators. **Physics of Plasmas,** v. 19, n. 5, 2012.

[68] LIMPERT, J. et al. Ultrafast fiber lasers for strong-field physics experiments. **Laser & Photonics Reviews,** v. 5, n. 5, p. 634-646, 2011.

[69] FATTAHI, H. et al. Third-generation femtosecond technology. **Optica,** v. 1, n. 1, p. 45-63, 2014.

[70] FOELSCH, K. The Analytical Design of an Axially Symmetric Laval Nozzle for a Parallel and Uniform Jet. **Journal of the Aeronautical Sciences,** v. 16, n. 3, p. 161-&, 1949.

[71] DORCHIES, F. et al. Spatial distribution of cluster size and density in supersonic jets as targets for intense laser pulses. **Physical Review A,** v. 68, n. 2, 2003.

[72] ROVIGE, L. et al. Demonstration of stable long-term operation of a kilohertz laser-plasma accelerator. **Physical Review Accelerators and Beams,** v. 23, n. 9, 2020.

[73] DOPP, A. et al. 3D printing of gas jet nozzles for laser-plasma accelerators. **Rev Sci Instrum,** v. 87, n. 7, p. 073505, 2016.

[74] RAE, S. C. Ionization-induced defocusing of intense laser pulses in high-pressure gases. **Optics Communications,** v. 97, n. 1-2, p. 25-28, 1993.

[75] HITT, D. L., ZAKRZWSKI, C. M. and THOMAS, M. A. MEMS-based satellite micropropulsion via catalyzed hydrogen peroxide decomposition. **Smart Materials & Structures,** v. 10, n. 6, p. 1163-1175, 2001.

[76] JANSON, S., HELVAJIAN, H. and BREUER, K. **MEMS, microengineering and aerospace systems**. 30th Fluid Dynamics Conference 1999.

[77] SALEHI, F. et al. Characterization of a 100 micrometer-scale cryogenically cooled gas jet for near-critical density laser-plasma experiments. **Review of Scientific Instruments,** v. 90, n. 10, 2019.

[78] SCHMID, K. and VEISZ, L. Supersonic gas jets for laser-plasma experiments. **Review of Scientific Instruments,** v. 83, n. 5, 2012.

[79] SPRANGLE, P., HAFIZI, B. and PENANO, J. R. Laser pulse modulation instabilities in plasma channels. **Physical Review E,** v. 61, n. 4, p. 4381-4393, 2000.

[80] YU, P. et al. Modeling of Laser Wakefield Acceleration In Lorentz Boosted Frame Using a Quasi-3D OSIRIS Algorithm. In: HOGAN, M. J. (Ed.). **Advanced Accelerator Concepts**, v.1777, 2016.

[81] JHA, P., SINGH, R. G. and UPADHYAY, A. K. Pulse distortion and modulation instability in laser plasma interaction. **Physics of Plasmas,** v. 16, n. 1, 2009.

[82] GOLOVIN, G. et al. Control and optimization of a staged laser-wakefield accelerator. **Nuclear Instruments & Methods in Physics Research Section a-Accelerators Spectrometers Detectors and Associated Equipment,** v. 830, p. 375-380, 2016.

[83] CHAGOVETS, T. et al. Automation of Target Delivery and Diagnostic Systems for High Repetition Rate Laser-Plasma Acceleration. **Applied Sciences,** v. 11, n. 4, p. 1680, 2021.

[84] ZAFFINO, R. et al. Preparation and characterization of micro-nano engineered targets for high-power laser experiments. **Microelectronic Engineering,** v. 194, p. 67-70, 2018.

[85] PRENCIPE, I. et al. Targets for high repetition rate laser facilities: needs, challenges and perspectives. **High Power Laser Science and Engineering,** v. 5, 2017.

[86] LIN, J. et al. Adaptive control of laser-wakefield accelerators driven by mid-IR laser pulses. **Optics Express,** v. 27, n. 8, p. 10912, 2019.

[87] SHALLOO, R. J. et al. Automation and control of laser wakefield accelerators using Bayesian optimization. **Nature Communications,** v. 11, n. 1, 2020.

[88] GONOSKOV, A. et al. Employing machine learning for theory validation and identification of experimental conditions in laser-plasma physics. **Scientific Reports,** v. 9, n. 1, 2019.

[89] DOWNER, M. C. et al. Diagnostics for plasma-based electron accelerators. **Reviews of Modern Physics,** v. 90, n. 3, 2018.

[90] COSTA, G. et al. Characterization of self-injected electron beams from LWFA experiments at SPARC_LAB. **Nuclear Instruments & Methods in Physics Research Section a-Accelerators Spectrometers Detectors and Associated Equipment,** v. 909, p. 118-122, 2018.

[91] SETTLES, G. S. **Schlieren and shadowgraph techniques : visualizing phenomena in transparent media**. Berlin ; New York: Springer, 2001.

[92] SHIRAISHI, S. et al. Laser red shifting based characterization of wakefield excitation in a laser-plasma accelerator. **Physics of Plasmas,** v. 20, n. 6, 2013.

[93] BRANDI, F. and GIZZI, L. A. Optical diagnostics for density measurement in high-quality laser-plasma electron accelerators. **High Power Laser Science and Engineering,** v. 7, 2019.

[94] SWEENEY, D. W., ATTWOOD, D. T. and COLEMAN, L. W. Interferometric Probing of Laser-Produced Plasmas. **Applied Optics,** v. 15, n. 5, p. 1126-1128, 1976.

[95] JAROSZYNSKI, D. A., BINGHAM, R. and CAIRNS, R. A. **Laser-plasma interactions**. Boca Raton: CRC Press/Taylor & Francis, 2009.

[96] BRANDI, F. et al. Measurement of the particle number density in a pulsed flow gas cell with a second-harmonic interferometer. **6th Target Fabrication Workshop (Tfw6) and the Targetry for High Repetition Rate Laser-Driven Sources (Targ3) Conference,** v. 1079, 2018.

[97] ARUNACHALAM, A. K. et al. Observation of non-symmetric side-scattering during high-intensity laser-plasma interactions. **New Journal of Physics,** v. 20, n. 3, p. 033027, 2018.

[98] ALBERT, F. et al. 2020 roadmap on plasma accelerators. **New Journal of Physics,** v. 23, n. 3, 2021.

[99] MARQUÈS, J. R. et al. Temporal and Spatial Measurements of the Electron Density Perturbation Produced in the Wake of an Ultrashort Laser Pulse. **Physical Review Letters,** v. 76, n. 19, p. 3566-3569, 1996.

[100] GILLEY, K. N. et al. Risk Factors for COVID-19 in College Students Identified by Physical, Mental, and Social Health Reported During the Fall 2020 Semester: Observational Study Using the Roadmap App and Fitbit Wearable Sensors. **Jmir Mental Health,** v. 9, n. 2, 2022.

[101] VIEIRA, N. D. et al. **Laser particle acceleration in Brazil**. 2019 International Nuclear Atlantic Conference - INAC 2019. Santos, Brazil: ABEN, 2019. 13 p.

[102] VIEIRA, N. D. et al. **Compact Laser Accelerators for medical applications**. XLIV Congress of the Brazilian Biophysical Society. Santos, Brazil, 2019. p.

[103] BONATTO, A. et al. **On the Development of a Low Peak-Power, High Repetition-Rate Laser Plasma Accelerator at IPEN**. 12th INTERNATIONAL PARTICLE ACCELERATOR CONFERENCE. Campinas, Brazil, 2021. p.

[104] CIPICCIA, S. et al. A tuneable ultra-compact high-power, ultra-short pulsed, bright gamma-ray source based on bremsstrahlung radiation from laser-plasma accelerated electrons. **Journal of Applied Physics,** v. 111, n. 6, 2012.

[105] ROUSSE, A. et al. Production of a keV X-Ray Beam from Synchrotron Radiation in Relativistic Laser-Plasma Interaction. **Physical Review Letters,** v. 93, n. 13, 2004.

[106] VIEIRA, N. D. et al. **Laser wakefield electron accelerator: possible use for radioisotope production**. 2021 SBFoton International Optics and Photonics Conference (SBFoton IOPC), 2021. 1-5 p.

[107] MALHEIROS, T. Dois ministros, promessas antigas e um projeto de reator para salvar vidas parado. **20 jun., 2022**, https://www.ipen.br/portal_por/portal/interna.php?secao_id=39&campo=16498, 29 set., 2021.

[108] KROLL, F. et al. Tumour irradiation in mice with a laser-accelerated proton beam. **Nature Physics,** v. 18, n. 3, p. 316-+, 2022.

[109] SVENDSEN, K. et al. A focused very high energy electron beam for fractionated stereotactic radiotherapy. **Scientific Reports,** v. 11, n. 1, 2021.

[110] FUCHS, T. et al. Treatment planning for laser-accelerated very-high energy electrons. **Physics in Medicine and Biology,** v. 54, n. 11, p. 3315-3328, 2009.

[111] MALDONADO, E. P. et al. **Self-modulated laser-plasma acceleration in a H2 gas target, simulated in a spectral particle-in-cell algorithm: wakefield and electron bunch properties**. 2019 SBFoton International Optics and Photonics Conference (SBFoton IOPC). São Paulo, Brazil: IEEE, 2019. 5 p.

[112] MALDONADO, E. P. et al. **Electron beam properties in self-modulated laser wakefield acceleration using TW and sub-TW pulses**. 2021 SBFoton International Optics and Photonics Conference (SBFoton IOPC), 2021. 1-5 p.

[113] MALDONADO, E. P. et al. **Simulation of a Laser Wakefield Accelerator in Downramp Injection Regime Suitable for High Repetition Rates**. Latin America Optics and Photonics (LAOP) Conference 2022. Recife: Optica Publishing Group, 2022. Tu1C.7 p.

[114] HIDDING, B. et al. Quasimonoenergetic electron acceleration in the self-modulated laser wakefield regime. **Physics of Plasmas,** v. 16, n. 4, 2009.

[115] SAMAD, R. E. et al. **High Intensity ultrashort laser pulses and their applications at IPEN**. 2021 SBFoton International Optics and Photonics Conference (SBFoton IOPC), 2021. 1-5 p.

[116] CHIOMENTO, B. B. et al. **Development of dielectric de Laval nozzles for laser electron acceleration by ultrashort pulses micromachining**. 2021 SBFoton International Optics and Photonics Conference (SBFoton IOPC), 2021. 1-5 p.

[117] TABACOW, F. B. D. et al. **Theoretical and experimental study of supersonic gas jet targets for laser wakefield acceleration**. 2021 SBFoton International Optics and Photonics Conference (SBFoton IOPC), 2021. 1-5 p.

[118] ZUFFI, A. V. F. et al. **Development of a modified Mach-Zehnder interferometer for time and space density measurements for laser wakefield acceleration**. 2021 SBFoton International Optics and Photonics Conference (SBFoton IOPC), 2021. 1-5 p.

[119] SAMAD, R. E. et al. **Development and Optical Characterization of Supersonic Gas Targets for High-Intensity Laser Plasma Studies**. 2018 SBFoton International Optics and Photonics Conference (SBFoton IOPC). Campinas, Brazil IEEE**:** 5 p. 2018.

[120] ZUFFI, A. V. F. et al. **Ultrafast laser micromachining of submillimetric de Laval nozzles in alumina for laser electron acceleration**. 2022 SBFoton International Optics and Photonics Conference (SBFoton IOPC). Recife, Brazil, 2022. 1-5 p.

[121] LASERNETUS. "LaserNetUS Cycle 3 Experiments Announced". LaserNetUS web site, 2021. Available in: < https://lasernetus.org/resources/awarded-experiments/lasernetus-cycle-3-experiments-announced >. Acess in: Jun 28 , 2022.

[122] ZUFFI, A. V. F. et al. **Time-Resolved Femtosecond Laser-Plasma Measurements by a Mach-Zehnder-Like Interferometer**. Latin America Optics and Photonics Conference. Recife, Brazil: 7-11 aug 2022, 2022. p.

[123] ZUFFI, A. V. F. et al. Femtosecond laser-plasma dynamics study by a time-resolved Mach–Zehnder-like interferometer. **Applied Optics,** v. 62, n. 8, p. C128-C134, 2023.

[124] GIBBON, P. **Short pulse laser interactions with matter : an introduction**. London: Imperial College Press, 2005.

[125] ARUNACHALAM, A. K. **Investigation of laser-plasma interactions at near-critical densities**. 2017. 119 (Ph.D.). University of Jena, University of Jena, Jena.

[126] SÄVERT, A. **Few-cycle microscopy of a laser wakefield accelerator**. 2016. 130 (Ph.D.). Faculty of Physics and Astronomy, Friedrich-Schiller-Universität Jena

[127] LIN, J. **Electron Acceleration and Radiation Generation from Relativistic Laser-Plasma Interactions at High Repetition-Rate**. 2021. 220 (Ph.D. Thesis). Nuclear Engineering and Radiological Sciences, University of Michigan, Ann Arbor, Michigan, US.

[128] JUNG, R. **Laser-plasma interaction with ultra-short laser pulses**. 2007. 198 (Ph.D. Thesis). Heinrich-Heine-Universität Düsseldorf, Heinrich-Heine-Universität Düsseldorf, Düsseldorf.

[129] SHEN, Y. R. **The principles of nonlinear optics**. New York: J. Wiley, 1984.

[130] KELDYSH, L. V. Ionization in Field of a Strong Electromagnetic Wave. **Soviet Physics Jetp-Ussr,** v. 20, n. 5, p. 1307-1314, 1965.

[131] AUGST, S. et al. Tunneling Ionization of Noble-Gases in a High-Intensity Laser Field. **Physical Review Letters,** v. 63, n. 20, p. 2212-2215, 1989.

[132] AUGST, S. et al. Laser Ionization of Noble-Gases by Coulomb-Barrier Suppression. **Journal of the Optical Society of America B-Optical Physics,** v. 8, n. 4, p. 858-867, 1991.

[133] ZUFFI, A. V. F., VIEIRA, N. D. and SAMAD, R. E. Below-threshold-harmonics-generation limitation due to laser-induced ionization in noble gases. **Physical Review A,** v. 105, n. 2, 2022.

[134] FILIN, A. et al. Impact-Ionization Cooling in Laser-Induced Plasma Filaments. **Physical Review Letters,** v. 102, n. 15, 2009.

[135] LAWSON, J. D. Lasers and Accelerators. **Ieee Transactions on Nuclear Science,** v. 26, n. 3, p. 4217-4219, 1979.

[136] WOODWARD, P. M. A Method of Calculating the Field over a Plane Aperture Required to Produce a Given Polar Diagram. **Journal of the Institution of Electrical Engineers,** v. 93, n. 10, p. 1554-1558, 1947.

[137] ESAREY, E., SPRANGLE, P. and KRALL, J. Laser Acceleration of Electrons in Vacuum. **Physical Review E,** v. 52, n. 5, p. 5443-5453, 1995.

[138] SCHMID, K. **Laser Wakefield Electron Acceleration: A Novel Approach Employing Supersonic Microjets and Few-Cycle Laser Pulses**. 2011. 179 (Ph.D. Thesis). Max Planck Institute, Garching, Germany.

[139] BAUER, D., MULSER, P. and STEEB, W. H. Relativistic Ponderomotive Force, Uphill Acceleration, and Transition to Chaos. **Physical Review Letters,** v. 75, n. 25, p. 4622-4625, 1995.

[140] PLATEAU, G. **Electron bunch diagnostic for laser-plasma accelerators, from THz to X-rays**. 2011. 197 (PhD Thesis). École Polytechnique X, École Polytechnique, Paris, France.

[141] BOHM, D. and GROSS, E. P. Theory of Plasma Oscillations .A. Origin of Medium-Like Behavior. **Physical Review,** v. 75, n. 12, p. 1851-1864, 1949.

[142] GRIFFITHS, D. J. **Introduction to electrodynamics**. 3rd. Upper Saddler River, NJ: Prentice Hall, 1999.

[143] BOYD, R. W. **Nonlinear optics**. 2nd. San Diego, CA: Academic Press, 2003.

[144] RANKIN, R. et al. Refraction Effects Associated with Multiphoton Ionization and Ultrashort-Pulse Laser Propagation in Plasma Wave-Guides. **Optics Letters,** v. 16, n. 11, p. 835-837, 1991.

[145] GIBBON, P. et al. Experimental study of relativistic self-focusing and self-channeling of an intense laser pulse in an underdense plasma. **IEEE Transactions on Plasma Science,** v. 24, n. 2, p. 343-350, 1996.

[146] FEIT, M. D., KOMASHKO, A. M. and RUBENCHIK, A. M. Relativistic self-focusing in underdense plasma. **Physica D: Nonlinear Phenomena,** v. 152-153, p. 705-713, 2001.

[147] DAWSON, J. M. Nonlinear Electron Oscillations in a Cold Plasma. **Physical Review,** v. 113, n. 2, p. 383-387, 1959.

[148] AKHIEZER, A. I. and POLOVIN, R. V. Theory of Wave Motion of an Electron Plasma. **Soviet Physics Jetp-Ussr,** v. 3, n. 5, p. 696-705, 1956.

[149] ROSENZWEIG, J. B. Trapping, thermal effects, and wave breaking in the nonlinear plasma wake-field accelerator. **Physical Review A,** v. 38, n. 7, p. 3634-3642, 1988.

[150] SHENG, Z. M. and MEYERTERVEHN, J. Relativistic wave breaking in warm plasmas. **Physics of Plasmas,** v. 4, n. 2, p. 493-495, 1997.

[151] BULANOV, S. V. et al. Transverse-Wake Wave Breaking. **Physical Review Letters,** v. 78, n. 22, p. 4205-4208, 1997.

[152] FAURE, J. et al. Controlled injection and acceleration of electrons in plasma wakefields by colliding laser pulses. **Nature,** v. 444, n. 7120, p. 737-739, 2006.

[153] UMSTADTER, D., ESAREY, E. and KIM, J. Nonlinear Plasma Waves Resonantly Driven by Optimized Laser Pulse Trains. **Physical Review Letters,** v. 72, n. 8, p. 1224-1227, 1994.

[154] CLAYTON, C. E. et al. Self-Guided Laser Wakefield Acceleration beyond 1 GeV Using Ionization-Induced Injection. **Physical Review Letters,** v. 105, n. 10, 2010.

[155] THAURY, C. et al. Shock assisted ionization injection in laser-plasma accelerators. **Scientific Reports,** v. 5, n. 1, p. 16310, 2015.

[156] BUCK, A. et al. Shock-Front Injector for High-Quality Laser-Plasma Acceleration. **Physical Review Letters,** v. 110, n. 18, 2013.

[157] GONSALVES, A. J. et al. Tunable laser plasma accelerator based on longitudinal density tailoring. **Nature Physics,** v. 7, n. 11, p. 862-866, 2011.

[158] DE LA OSSA, A. M. et al. Optimizing density down-ramp injection for beam-driven plasma wakefield accelerators. **Physical Review Accelerators and Beams,** v. 20, n. 9, 2017.

[159] BEREZHIANI, V. I. and MURUSIDZE, I. G. Relativistic Wake-Field Generation by an Intense Laser-Pulse in a Plasma. **Physics Letters A,** v. 148, n. 6-7, p. 338-340, 1990.

[160] BUTLER, A., SPENCE, D. J. and HOOKER, S. M. Guiding of High-Intensity Laser Pulses with a Hydrogen-Filled Capillary Discharge Waveguide. **Physical Review Letters,** v. 89, n. 18, 2002.

[161] LEEMANS, W. P. et al. Multi-GeV Electron Beams from Capillary-Discharge-Guided Subpetawatt Laser Pulses in the Self-Trapping Regime. **Physical Review Letters,** v. 113, n. 24, 2014.

[162] MATLIS, N. H. et al. Snapshots of laser wakefields. **Nature Physics,** v. 2, n. 11, p. 749-753, 2006.

[163] BIRDSALL, C. K. and LANGDON, A. B. **Plasma physics via computer simulation**. New York: McGraw-Hill, 1985.

[164] LEHE, R. and KIRCHEN, M. FBPIC algorithm & features. github, 2016. Available in: < https://fbpic.github.io/overview/pic_algorithm.html >. Acess in: Jan 30, 2023.

[165] LEHE, R. et al. A spectral, quasi-cylindrical and dispersion-free Particle-In-Cell algorithm. **Computer Physics Communications,** v. 203, p. 66-82, 2016.

[166] AMMOSOV, M. V., DELONE, N. B. and KRAINOV, V. P. Tunnel Ionization of Complex Atoms and Atomic Ions in a Varying Electromagnetic-Field. **Zhurnal Eksperimentalnoi I Teoreticheskoi Fiziki,** v. 91, n. 6, p. 2008-2013, 1986.

[167] KARANPREETVIRK. A review on self focusing in laser plasma interaction. **Materials Today: Proceedings,** v. 37, p. 2786-2791, 2021.

[168] SIEGRIST, M. R. Self-focusing in a plasma due to ponderomotive forces and relativistic effects. **Optics Communications,** v. 16, n. 3, p. 402-407, 1976.

[169] LIN, M. W. et al. Laser wakefield acceleration driven by a few-terawatt laser pulse in a sub-mm nitrogen gas jet. **Physics of Plasmas,** v. 27, n. 11, 2020.

[170] TOURNOIS, P. Acousto-optic programmable dispersive filter for adaptive compensation of group delay time dispersion in laser systems. **Optics Communications,** v. 140, n. 4-6, p. 245-249, 1997.

[171] SAMAD, R. E. **Desenvolvimento de um amplificador de pulsos ultracurtos de Cr:LiSAF para um sistema laser híbrido de alta potência**. 2006. xiii, 124 Tese de Doutorado (Ph. D.). Instituto de Física da USP, Universidade de São Paulo, São Paulo.

[172] SAMAD, R. E. et al. 5 Hz flashlamp pumped Cr:LiSAF multipass amplifier for ultrashort pulses. **Journal of Optics A: Pure and Applied Optics,** v. 10, n. 10, p. 104010, 2008.

[173] SAMAD, R. E. et al. Development of a TW level Cr : LiSAF multipass amplifier. **Riao/Optilas 2007,** v. 992, p. 398-402, 2008.

[174] UIBERACKER, M. et al. Attosecond real-time observation of electron tunnelling in atoms. **Nature,** v. 446, n. 7136, p. 627-632, 2007.

[175] LIN, K. F. and SCHAEFER, G. **A Low-Cost Compact Ccd Grating Spectrometer**. Ias 93. Toronto, Ont.: Canada, 1993. 2334-2337 p.

[176] ARMSTRONG, J. A. Measurement of Picosecond Laser Pulse Widths. **Applied Physics Letters,** v. 10, n. 1, p. 16-18, 1967.

[177] SYLLA, F. et al. Development and characterization of very dense submillimetric gas jets for laser-plasma interaction. **Review of Scientific Instruments,** v. 83, n. 3, p. 033507, 2012.

[178] HENARES, J. L. et al. Development of gas jet targets for laser-plasma experiments at near-critical density. **Review of Scientific Instruments,** v. 90, n. 6, 2019.

[179] CHENG, J. et al. A review of ultrafast laser materials micromachining. **Optics and Laser Technology,** v. 46, p. 88-102, 2013.

[180] MISHRA, S. and YADAVA, V. Laser Beam MicroMachining (LBMM) - A review. **Optics and Lasers in Engineering,** v. 73, p. 89-122, 2015.

[181] LORAZO, P., LEWIS, L. J. and MEUNIER, M. Short-pulse laser ablation of solids: From phase explosion to fragmentation. **Physical Review Letters,** v. 91, n. 22, 2003.

[182] PEREZ, D. and LEWIS, L. J. Molecular-dynamics study of ablation of solids under femtosecond laser pulses. **Physical Review B,** v. 67, n. 18, 2003.

[183] BULGAKOVA, N. M. et al. A general continuum approach to describe fast electronic transport in pulsed laser irradiated materials: The problem of Coulomb explosion. **Applied Physics A,** v. 81, n. 2, p. 345-356, 2005.

[184] STOIAN, R. et al. Surface Charging and Impulsive Ion Ejection during Ultrashort Pulsed Laser Ablation. **Physical Review Letters,** v. 88, n. 9, 2002.

[185] GAMALY, E. G. The physics of ultra-short laser interaction with solids at non-relativistic intensities. **Physics Reports-Review Section of Physics Letters,** v. 508, n. 4-5, p. 91-243, 2011.

[186] KAUTEK, W. et al. Laser ablation of dielectrics with pulse durations between 20 fs and 3 ps. **Applied Physics Letters,** v. 69, n. 21, p. 3146-3148, 1996.

[187] JOGLEKAR, A. P. et al. A study of the deterministic character of optical damage by femtosecond laser pulses and applications to nanomachining. **Applied Physics B-Lasers and Optics,** v. 77, n. 1, p. 25-30, 2003.

[188] GAMALY, E. G. et al. Ablation of solids by femtosecond lasers: Ablation mechanism and ablation thresholds for metals and dielectrics. **Physics of Plasmas,** v. 9, n. 3, p. 949-957, 2002.

[189] SAMAD, R. E. et al. **Ultrashort Laser Pulses Machining**. InTech, 2012.

[190] LUGOVSKOY, A. V. and BRAY, I. Ultrafast electron dynamics in metals under laser irradiation. **Physical Review B,** v. 60, n. 5, p. 3279-3288, 1999.

[191] NOLTE, S. et al. Ablation of metals by ultrashort laser pulses. **Journal of the Optical Society of America B-Optical Physics,** v. 14, n. 10, p. 2716-2722, 1997.

[192] TUENNERMANN, A., NOLTE, S. and LIMPERT, J. Femtosecond vs. Picosecond Laser Material Processing. **Laser Technik Journal,** v. 7, n. 1, p. 34-38, 2010.

[193] PERRY, M. D. et al. Ultrashort-pulse laser machining of dielectric materials. **Journal of Applied Physics,** v. 85, n. 9, p. 6803-6810, 1999.

[194] SANG, B. H. and JEON, T. I. Pressure-dependent refractive indices of gases by THz time-domain spectroscopy. **Optics Express,** v. 24, n. 25, p. 29041-29048, 2016.

[195] GUSTAS, D. et al. High-charge relativistic electron bunches from a kHz laser-plasma accelerator. **Physical Review Accelerators and Beams,** v. 21, n. 1, 2018.

[196] GARCIA-LECHUGA, M., SOLIS, J. and SIEGEL, J. Melt front propagation in dielectrics upon femtosecond laser irradiation: Formation dynamics of a heat-affected layer. **Applied Physics Letters,** v. 108, n. 17, 2016.

[197] LE, Q. T., BERTRAND, C. and VILAR, R. Femtosecond laser ablation of enamel. **Journal of Biomedical Optics,** v. 21, n. 6, 2016.

[198] NIE, B. et al. Femtosecond laser melting and resolidifying of high-temperature powder materials. **Applied Physics a-Materials Science & Processing,** v. 118, n. 1, p. 37-41, 2015.

[199] ZHOU, O. C. et al. Effect of nozzle curvature on supersonic gas jets used in laser-plasma acceleration. **Physics of Plasmas,** v. 28, n. 9, 2021.

[200] PEDROTTI, F. L., PEDROTTI, L. M. and PEDROTTI, L. S. **Introduction to optics**. 3rd. Upper Saddle River, N.J.: Pearson/Prentice Hall, 2007.

[201] BENATTAR, R., POPOVICS, C. and SIGEL, R. Polarized-Light Interferometer for Laser Fusion Studies. **Review of Scientific Instruments,** v. 50, n. 12, p. 1583-1585, 1979.

[202] COUPERUS, J. P. et al. Tomographic characterisation of gas-jet targets for laser wakefield acceleration. **Nuclear Instruments & Methods in Physics Research Section a-Accelerators Spectrometers Detectors and Associated Equipment,** v. 830, p. 504-509, 2016.

[203] MALKA, V. et al. Characterization of neutral density profile in a wide range of pressure of cylindrical pulsed gas jets. **Review of Scientific Instruments,** v. 71, n. 6, p. 2329-2333, 2000.

[204] HERRAEZ, M. A. et al. Fast two-dimensional phase-unwrapping algorithm based on sorting by reliability following a noncontinuous path. **Applied Optics,** v. 41, n. 35, p. 7437-7444, 2002.

[205] ÁLVAREZ, R., RODERO, A. and QUINTERO, M. C. An Abel inversion method for radially resolved measurements in the axial injection torch. **Spectrochimica Acta Part B: Atomic Spectroscopy,** v. 57, n. 11, p. 1665-1680, 2002.

[206] ALVAREZ, R., RODERO, A. and QUINTERO, M. C. An Abel inversion method for radially resolved measurements in the axial injection torch. **Spectrochimica Acta Part B-Atomic Spectroscopy,** v. 57, n. 11, p. 1665-1680, 2002.

[207] GOLOVIN, G. et al. Tomographic imaging of nonsymmetric multicomponent tailored supersonic flows from structured gas nozzles. **Applied Optics,** v. 54, n. 11, p. 3491-3497, 2015.

[208] LANDGRAF, B. et al. High resolution 3D gas-jet characterization. **Review of Scientific Instruments,** v. 82, n. 8, 2011.

[209] LORENTZ, H. A. Über die Beziehungzwischen der Fortpflanzungsgeschwindigkeit des Lichtes derKörperdichte. **Ann. Phys. 9**, p. 641-665, 1880.

[210] LORENZ, L. Über die Refractionsconstante. **Ann. Phys. 11**, p. 70-103, 1880.

[211] VERDEYEN, J. T. and GERARDO, J. B. Application of Laser to Plasma Refractive Index Determination. **Annals of the New York Academy of Sciences,** v. 122, n. A2, p. 676-684, 1965.

[212] TOMASSINI, P. and GIULIETTI, A. A generalization of Abel inversion to non-axisymmetric density distribution. **Optics Communications,** v. 199, n. 1-4, p. 143-148, 2001.

[213] HICKSTEIN, D. D. et al. A direct comparison of high-speed methods for the numerical Abel transform. **Review of Scientific Instruments,** v. 90, n. 6, 2019.

[214] SANTOS, J. R. et al. InterferometryAnalysis_GasJet: Initial Release (version 1.0). 2023 Available in: < https://zenodo.org/record/7778947#.ZCMz4HbMK3C >. Acess in: Mar. 28, 2023.

[215] SANTOS, J. R. et al. InterferometryAnalysis_LIP: Initial Release (version 1.0). 2023. Available in: < https://zenodo.org/record/7864173#.ZEgNT3bMIb0 >. Acess in: April 28, 2023.

[216] LEHMANN, M. Decorrelation-induced phase errors in phase-shifting speckle interferometry. **Applied Optics,** v. 36, n. 16, p. 3657-3667, 1997.

[217] PAUL, R. K. et al. Reconstruction errors in Abel inversion. **Plasma Devices and Operations,** v. 13, n. 4, p. 281-289, 2005.

[218] SANTOS, J. R. et al. Softwares to recover density profiles of the gas jets and plasmas from interferometry technique. **[Manuscript in preparation]**, 2023.

[219] SETTLES, G. S. and HARGATHER, M. J. A review of recent developments in schlieren and shadowgraph techniques. **Measurement Science and Technology,** v. 28, n. 4, p. 042001, 2017.

[220] LIM, H. D. et al. Optical Flow Technique for Supersonic Jet Measurements. **World Academy of Science, Engineering and Technology,** v. 10, p. 1228, 2016.

[221] OLNEY, T. N. et al. Absolute scale determination for photoabsorption spectra and the calculation of molecular properties using dipole sum rules. **Chemical Physics,** v. 223, n. 1, p. 59-98, 1997.

[222] NORMAN, M. L. and WINKLER, K.-H. A. **Supersonic Jets** Los Alamos Science Spring/Summer: Los Alamos National Laboratory. 12**:** 1-34 p. 1985.

[223] NORMAN, M. L. et al. Structure and Dynamics of Supersonic Jets. **Astronomy & Astrophysics,** v. 113, n. 2, p. 285-302, 1982.

[224] DIELS, J.-C. and RUDOLPH, W. **Ultrashort laser pulse phenomena : fundamentals, techniques, and applications on a femtosecond time scale**. 2nd. Amsterdam ; Boston: Elsevier / Academic Press, 2006.

[225] DORRER, C. Influence of the calibration of the detector on spectral interferometry. **Journal of the Optical Society of America B-Optical Physics,** v. 16, n. 7, p. 1160-1168, 1999.

[226] LEPETIT, L., CHERIAUX, G. and JOFFRE, M. Linear techniques of phase measurement by femtosecond spectral interferometry for applications in spectroscopy. **Journal of the Optical Society of America B-Optical Physics,** v. 12, n. 12, p. 2467-2474, 1995.

[227] COUAIRON, A. and MYSYROWICZ, A. Femtosecond filamentation in transparent media. **Physics Reports-Review Section of Physics Letters,** v. 441, n. 2-4, p. 47-189, 2007.

[228] TIWARI, P. K. et al. Laser induced tunnel ionization and electron density evolution in air. **Journal of the Physical Society of Japan,** v. 74, n. 8, p. 2255-2259, 2005.

[229] LIU, J. S. et al. Sub-picosecond resolved investigation of dynamics of laser driven plasma by broad band chirped-pulse spectral interferometry. **X-Ray Lasers 2002,** v. 641, p. 328-331, 2002.

[230] ZUFFI, A. V. F., VIEIRA, N. D. and SAMAD, R. E. Below-threshold-harmonics-generation limitation due to laser-induced ionization in noble gases. **Physical Review A,** v. 105, n. 2, p. 023112, 2022.

[231] BATANI, D. et al. Optical Time-Resolved Diagnostics of Laser-Produced Plasmas. **Journal of Fusion Energy,** v. 38, n. 3-4, p. 299-314, 2019.

[232] SEMAK, V. V. and SHNEIDER, M. N. Effect of power losses on self-focusing of high-intensity laser beam in gases. **Journal of Physics D-Applied Physics,** v. 46, n. 18, p. 185502, 2013.

[233] MLEJNEK, M., WRIGHT, E. M. and MOLONEY, J. V. Power dependence of dynamic spatial replenishment of femtosecond pulses propagating in air. **Optics Express,** v. 4, n. 7, p. 223-228, 1999.

[234] BRANDI, F. and GIZZI, L. A. Optical diagnostics for density measurement in high-quality laser-plasma electron accelerators. **High Power Laser Science and Engineering,** v. 7, p. e26, 2019.

[235] PENANO, J. et al. Remote lasing in air by recombination and electron impact excitation of molecular nitrogen. **Journal of Applied Physics,** v. 111, n. 3, p. 033105, 2012.

[236] GOFFIN, A. et al. Optical Guiding in 50-Meter-Scale Air Waveguides. **Physical Review X,** v. 13, n. 1, 2023.

[237] MCWHIRTER, R. W. P. Ultraviolet and X-ray Spectroscopy of the Solar Atmosphere. In: HUDDLESTONE, R. H. andLEONARD, S. L. (Ed.). **Plasma**

Diagnostic Techniques. New York:: Academic Press, Inc, 1965. cap. 5, p.201–264.

[238] DOS SANTOS, J. R. et al. Measurement of Dysprosium Stark Width and the Electron Impact Width Parameter. **Applied Spectroscopy,** v. 73, n. 2, p. 203-213, 2019.

[239] BERNHARDT, J. et al. Spectroscopic analysis of femtosecond laser plasma filament in air. **Optics Communications,** v. 281, n. 5, p. 1268-1274, 2008.

[240] BEKEFI, G. **Principles of laser plasmas**. New York: Wiley, 1976.

[241] KRAMIDA, A. et al. NIST Atomic Spectra Database (version 5.9). 2022. Available in: < https://physics.nist.gov/asd >.

[242] WELCH, E. et al. Observation of breakdown wave mechanism in avalanche ionization produced atmospheric plasma generated by a picosecond CO_2 laser. **Physics of Plasmas,** v. 29, n. 5, p. 053504, 2022.

[243] FILIN, A. et al. Impact-ionization cooling in laser-induced plasma filaments. **Physical Review Letters,** v. 102, n. 15, p. 155004, 2009.

[244] COUAIRON, A. and MYSYROWICZ, A. Femtosecond filamentation in transparent media. **Physics Reports,** v. 441, n. 2-4, p. 47-189, 2007.

[245] BANERJEE, S. et al. Optical deflection and temporal characterization of an ultrafast laser-produced electron beam. **Physical Review Letters,** v. 95, n. 3, 2005.

[246] CHEN, S. et al. MeV-Energy X Rays from Inverse Compton Scattering with Laser-Wakefield Accelerated Electrons. **Physical Review Letters,** v. 110, n. 15, 2013.

[247] GOLOVIN, G. et al. Electron Trapping from Interactions between Laser-Driven Relativistic Plasma Waves. **Physical Review Letters,** v. 121, n. 10, 2018.

[248] POWERS, N. D. et al. Quasi-monoenergetic and tunable X-rays from a laser-driven Compton light source. **Nature Photonics,** v. 8, n. 1, p. 29-32, 2014.

[249] LASERNETUS. "LaserNetUS Cycle 3 Proposal Submissions". LaserNetUS web site, 2022. Available in: < https://lasernetus.org/proposal >. Acess in: Mar 15, 2023.

INSTITUTO DE PESQUISAS ENERGÉTICAS E NUCLEARES
Diretoria de Pesquisa, Desenvolvimento e Ensino
Av. Prof. Lineu Prestes, 2242 – Cidade Universitária CEP: 05508-000
Fone/Fax(0XX11) 3133-8908
SÃO PAULO – São Paulo – Brasil
http://www.ipen.br

O IPEN é uma Autarquia vinculada à Secretaria de Desenvolvimento, associada à Universidade de São Paulo e gerida técnica e administrativamente pela Comissão Nacional de Energia Nuclear, órgão do Ministério da Ciência, Tecnologia, Inovações e Comunicações.